TABLE OF CONTENTS

LIST OF TABLES

LIST OF FIGURES

INTRODUCTION

The size of critical metal components used in Aerospace, Transport and Energy production has evolved significantly over the last decade. Industrial needs have become slave to progress and increasingly strict client specifications. Internal defects must be eradicated before the delivery of the final workpiece in order to satisfy expectations and to stamp out all concerns of an unfaltering mechanical health during working life.

The forming process plays an essential role in the elimination of a high percentage of defects. Thus, it is at an elemental level that the future mechanical properties of the workpiece are to be decided. In the forming of ultra large ingots this entails casting and hot forging, two processes that have yet to be explicitly modelled particularly because each company possesses its own recipe. Finite model simulations are commonly used as a descriptive tool for the quantification of the physical phenomena arisen during the fabrication process. The results of which determine the framework of forthcoming process development.

The defects studied in the current work are internal voids with a particular focus on the simulation of void closure within large ingots. Void elimination typically occurs during the initial phases of the ingots elaboration notably during hot forging. It is a two part process detailing mechanical closure and a material healing mechanism. Both are necessary for successful void closure. The void volume must be reduced to zero before a final bonding of the internal surfaces may ensue.

The existing mathematical models are currently incapable of correctly predicting void closure on an industrial level. At present, the lack behind the comprehension of this phenomena makes the application of existing formula extremely case sensitive.

In association with Sorel Forge, the objective of this work is to successfully constitute a simulation prediction model for void closure. Thereby establishing criteria for the optimisation of their industrial process.

In accordance with the industrial partner, the case study focuses on large ingots with initial voids during hot forging. Void geometries and orientations vary in relation to real void morphologies. The casting process is not studied. Various grades of steel are considered. Exact proportions of the chemical composition are not divulged in order to adhere to the confidentiality clause.

This M.Sc thesis encompasses 5 chapters.

CHAPTER 1 is an extensive review of relevant literature concerning the proposed subject. This state of the art discusses the two main approaches used in void closure models. A macroscopic resolution, traditionally used for industrial purposes, and a micromechanical insight are examined before the modern mesoscopic description is addressed. The effect of hot forging on void closure and material behaviour is discussed. Different classical void closure models are compared. Microtomography, a modern characterisation technique is presented.

CHAPTER 2 is a preliminary analysis of the open die forging process. The fabrication procedure is broken down into forging sequences and potential indicators for successful forgings are selected. The feasibility of an in-depth study to characterize successful forgings based on experimental forging results is evaluated.

CHAPTER 3 features an in-depth discussion on applicable void closure models for industrial use. Existing mathematical void closure models are studied and represented using 3D mapping techniques. Significance is given to stress triaxiality states, applied remote strain and material parameters. Rational functions of the third degree are developed in order to easily adapt existing models to specific materials. Void closure is predicted for 42CrMo4, 34CrMo4 and 14NiCrMo13. A suitable model is chosen for Sorel steels.

CHAPTER 4 constitutes a FEM simulation of an open die forging sequence. Previous data and models are implemented in order to evaluate void closure. Virtual voids are introduced

for forging direction effects along a vertical, horizontal and 45 degree axis. The simulated sequence is representative of major void deformation during the hot forging process. The applied simulation method explains the efficiency of the consecutive forging sequence.

CHAPTER 5 headlines the development of a successful forging prediction simulation tool named Forge Calculus. Over 250 files of forging data are computed and analysed. The overall running of the program's internal logic is explained and the mathematical models used for simulation prediction are detailed. Future development is discussed and highly recommended.

CHAPTER 1

STATE OF THE ART

1.1   Introduction

This chapter includes an extensive review of literature concerning void closure in hot forging, setting a solid foundation for theory development in following chapters. It contains three main concepts.

Traditional macroscopic and micro-analytical approaches to the problem of void closure are discussed before giving the advantages of the new mesoscopic approach. Details concerning the physics of void generation, growth, and closure are interpreted with importance given to the influence of hot forming in the latter stages of development. Material behaviour is analysed and local thermodynamic conditions investigated for optimal void closure. X-ray Microtomography, used to characterise void morphologies, is presented as a favourable and promising technology. Different existing mathematical models for void closure are compared. The final stage of void closure known as healing is briefly discussed, but remains annex to the current papers focus point.

1.2   A modern day scale

Many classical models of void closure use one of two perspectives to approach the problem. The chosen philosophy depends on the application and the type of results required. The scale upon which the problem is addressed affects the utility and relevance of the results obtained. A third and more modern approach to the void closure problem has been developed in recent years and serves as a proposal in this thesis's solution.

1.2.1 Macroscopics

The macroscopic approach to the problem of void closure has become very popular and holds a great industrial interest because it focuses mainly on process parameters. Void closure mechanisms are function to process conditions, culminating in qualitative or quantitative results that are easily transposable to the working environment. Process development and optimisation are targeted in order to achieve forgings without defects. This approach generally implies experimental testing or numerical simulation.

Conclusions from Tvergaard (1982) and Ragab (2004) can be drawn that generalise the results obtained from a macroscopic process study, considering the hot forging of large ingots. The initial phases of material deformation have a strong influence on void closure. This is measured by far field equivalent strain which is seen to be a significant parameter.

Tkadlečková et al. (2013) showed the temperature gradient to affect void closure especially regarding centerline voids. A colder surface temperature improves efficiency in these areas on smaller billets (200x200mm) but seems to have no consequential effect on larger ingots given their increased thermal inertia. Heating of the workpiece to around 1250°C prior to forging was shown to increase initial void closure rates.

Other studies by Dudra and Im (1990), indicate that the interaction between the die and billet is noteworthy. The friction coefficient was studied by Chen (2006) and the shape and angle of the contact by Kakimoto et al. (2010). The optimisation of these parameters both proved to have a positive effect on void closure in large ingots. Shaped concave anvils were shown to produce a uniform strain distribution in the early stages of hot forging significantly improving initial void closure. Asymmetric external loading and a concave geometry was proved to accentuate compressive stresses within the workpiece. Contrastively, a flat die was deemed to be advantageous in the final stages of forging as they were demonstrated to possess a greater influence on the closure of central voids by Banaszek and Stefanik (2006).

1.2.2 Microanalytics

The models used in the micro-analytical approach consist of a single void in an infinite incompressible matrix. Their formulation is based on local thermodynamic readings with less emphasis on exterior loading. Micromechanic material behaviour follows a power law derived from a stress potential in a compressible nonlinear material as showcased by Huang. and Wang. (2006).

$$\bar{\bar{s}} = \frac{2}{3} \frac{\sigma_0}{\dot{\varepsilon}_0} \left(\frac{\dot{\varepsilon}_e}{\dot{\varepsilon}_0} \right)^{m-1} \bar{\bar{\dot{\varepsilon}}} \tag{1.1}$$

The chosen stress component, $\bar{\bar{s}}$, symbolizes the deviatoric stress tensor, a fundamental element of the Cauchy stress tensor alongside the hydrostatic representation of change in volume. The distortion of volume is function to $\bar{\bar{\dot{\varepsilon}}}$, the strain rate tensor. The other factors are: m, $(0 \leq m \leq 1)$ strain rate sensitivity exponent, σ_0 reference stress, $\dot{\varepsilon}_0$ and $\dot{\varepsilon}_e$ respectively reference and equivalent strain rate with

$$\dot{\varepsilon}_e = (\frac{3}{2} \bar{\bar{\dot{\varepsilon}}} : \bar{\bar{\dot{\varepsilon}}})^{\frac{1}{2}} \tag{1.2}$$

Strain rate sensitivity limits represent different material make-ups from $m = 0$, perfectly plastic to $m = 1$, denoting a viscous nature.

Micromechanics describe local phenomenon. Their application in void closure has only been effective on simplified void morphologies. The evolution of spherical, cylindrical, Budiansky et al. (1982), and more recently ellipsoidal, Chen et al. (2014) and Saby et al. (2014), geometries have led to analytical or semi-analytical formulas. The introductory models exclude temporal shape development, therefore making them far from pertinent for modelling large deformations and consequently, industrial processes. However, the more recent models account for a change in morphology and can therefore be used in industrial process simulation.

1.2.3 Mesoscopics

The philosophy of mesomechanics centralizes the premises of the two former approaches to void closure, achieving precise results whilst avoiding long macroscopic simulation calculation times. This perception considers the physical phenomenon at a microscopic level, governed by local thermodynamic conditions resulting from a combination of macroscopic external loadings, leading to deformations and heat transfer. Zhang et al. (2009) and Saby et al. (2013) studied void volume prediction with the mesoscale approach, both successfully creating verifiable theoretical models for the multi-scale problem using a Representative Volume Element (RVE) whilst considering the forging of large ingots. Model precision was tested against FE simulations and experimental data (Lee and Mear. 1994) with encouraging results.

Mesoscale models include substantial hypothesis in order to authentically represent the multi scale phenomenon. The vast amounts of miniature voids were assumed to have no effect on macroscopic deformation. Consequently, the initial void to billet volume ratio was deemed close to zero. Thermomechanical fields such as hydrostatic pressure or mean stress and equivalent Von Mises stress gathered from macro scale process parameters were presumed to be locally homogenous. These assumptions lead to further discussion and the implementation of certain model corrections into processing subroutines.

Mesoscopic or Mean field simulations are tools able to calculate the evolution of given parameters at any known location or integration point within the workpiece. The significant mechanical field variables concerning void closure are stress, strain and initial void morphology parameters. The Rayleigh Ritz method, a numeric solver algorithm for equations without exact answers, is used to obtain the morphology parameters for the volumetric strain rate of the proposed cell models. The criterion for material dependant void closure models depends heavily on the materials Norton and strain rate sensitivity exponent as reported by Budiansky et al. (1982), Zhang et al. (2009).
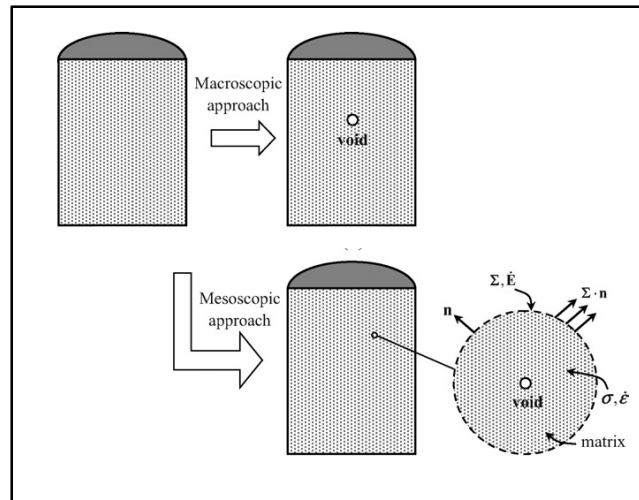
Figure 1 : Mesoscopic approach to modelling
voids in large ingots taken from (X. Zhang, 2008)

1.3   Void physics

This section of the literature review aims to present a global state of the art regarding the physics surrounding voids in metal. Void growth is studied and geometries prior to deformation are analysed. It is shown that initial void morphology parameters and void shape evolution have a significant effect on the accuracy of void closure calculation.

1.3.1   Void origins

Voids initiate as a result of several process parameters, taking place during casting, leaving rudimentary defects to be trapped during solidification. Nucleation, growth and void coalescence are three microscopic phenomena that have been subject to many recent studies as in Samei et al. (2016). Traditional metallographic techniques, notably electron microscopy, as used by Song et al. (2014), have helped with the qualification of these events. Initiation is defined by the breaking down of hard particles at the interface between matrices followed by the disintegration of hard particles of the second phase, particularly inclusions.

Growth ensues, with relative kinetics, function to material parameters, stress and strain. Rice and Tracey (1969) and Budiansky et al. (1982) considered the growth of an isolated spherical

void. The former in a perfectly plastic solid submitted to a remote uniform stress and strain rate. The latter in an infinite linear and non-linear matrix material under remote axisymmetric stress due to loading conditions. Both concluded that hydrostatic tensile stress and plastic deformation stimulate void expansion.

Duva and Hutchinson (1984) worked on an incompressible power-law material lattice with spherical voids, deriving constitutive relations to predict void coalescence. Niordson (2008), expanded upon this by studying the influence of different material length parameters, defining a length scale upon which gradient hardening became important, in void growth to coalescence and identified their influence on the material's overall mechanical characteristics. Results suggest that void growth is significantly suppressed when void dimensions are comparable to or smaller than the material's internal length parameter. Findings that were coherent with former research by Fleck and Hutchinson (2001).

Other interpretations are that void type defects can be caused by shrinkage and gas progression during solidification. Tkadlečková et al. (2013) and Saby (2013) collected data as to the location of porosities in extra-large cast ingots. Results showed higher void densities along ingot centerlines and in the upper regions (Fig 2.). The formation of voids at statistically backed locations could also be due to the surrounding microstructure. Carroll et al. (2012) studied the effect of grain size on local deformation near void-like structures, concluding that the size of strain concentration features are comparable to the materials local grain size as will be further developed in 1.5.2.
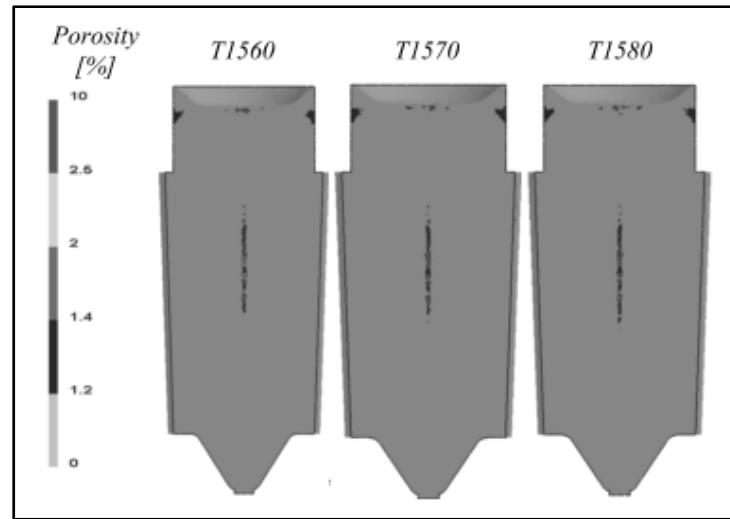
Figure 2 : Void distribution in different cast Steel ingots
taken from Tkadlečková et al. (2013)

1.3.2 Void geometries

It is industrially inconceivable that all void morphologies be modelled with complex real geometries. Despite the apparition of numerous analytical, semi-analytical and numeric models, none allow for real geometry perception. Modern modelling considers spherical, cylindrical and equivalent ellipsoidal voids. Works on void closure by Rice and Tracey (1969) and Budiansky et al. (1982), propose the conservation of a spherical void during hot forging. Later papers including Zhang et al. (2009) and Saby (2013) envisage an evolution of the voids morphology over time. These considerations lead to more accurate results concerning current closure states. Real mean-field simulations show 3D void shape metamorphosis on a 2D plane from sphere to ellipsoid to crack (Figure 3). It must be noted that this evolution path shows an excellent analogy with real void closure results by Lee and Mear (1999).

12
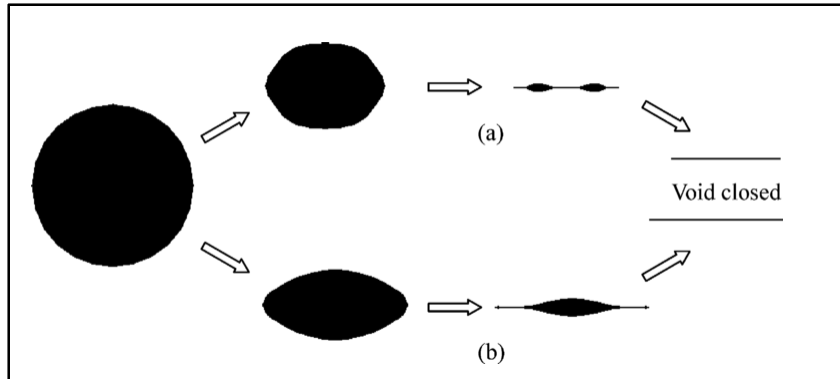
Figure 3 : Void geometry evolution during hot forging
taken from Zhang et al. (2009)

1.3.2.1   Simplified geometry (sphere, cylinder)

Traditional void closure models, Budiansky et al. (1982), Rice and Tracey (1969) or newer works from Chen et al. (2014) use simplified geometry in order obtain workable, analytical functions. Geometries include isolated spherical voids, circular-cylindrical and elliptic cylindrical voids. The latter will be discussed in a following paragraph.

Spherical models show good correlation to real void closure during initial stages of deformation. Significant error can occur for higher values of effective strain. This is explained by the fact that the current models do not consider void shape transformation. The initial spherical void remains spherical until completely closed.

Initial void morphology parameters are also considered significant. Accurate simulations depend on the adaptability of the model to compensate for the evolution of void geometry during the forging process.

1.3.2.2   Equivalent ellipsoids

More recent works from Saby (2013) and Zhang et al. (2012) introducing respectively the Zhang and Cisco models, use initial void geometry parameters; $\{q_i \in [0,4]\}$. The error of

these two models compared to real geometries is shown to be of 5% for the majority of voids encountered. The method details equivalent ellipsoids, calculated via inertia matrices to represent actual voids.

Inertia matrices can be calculated and implemented into source code as a subroutine at each integration step. The internal surfaces of a void were considered. Three node triangular elements were used and a homogenous unitary density supposed. The position of each of the three vertices $\{A, B, C\}$ of each finite element were used to obtain access to the diagonal components MI_i of the voids inertia matrix.

$$\text{For } i \in [1,3], \qquad MI_i = \sum_{\substack{j=1 \\ j \neq i}}^{3} P_{ij} \tag{1.3}$$

$$\text{With } P_{ij} = f(vol(T_r), O, A, B, C) \tag{1.4}$$

T_r being the triangular element of integration. The three strictly positive principal inertia moments $\{I_1, I_2, I_3\}$ are considered in order to calculate equivalent void dimensions $\{r_1, r_2, r_3\}$. The eigenvectors, defined in an orthonormal basis $\{\vec{u_1}, \vec{u_2}, \vec{u_3}\}$, represent the three principal axis for the ellipsoid. The ellipsoid's radii in these directions are computed as:

$$\text{For } i \in [1,3], \qquad r_i = \left(\frac{5}{2V} / \sum_{\substack{j=1 \\ j \neq i}}^{3} I_j - I_i\right)^{\frac{1}{2}} \tag{1.5}$$
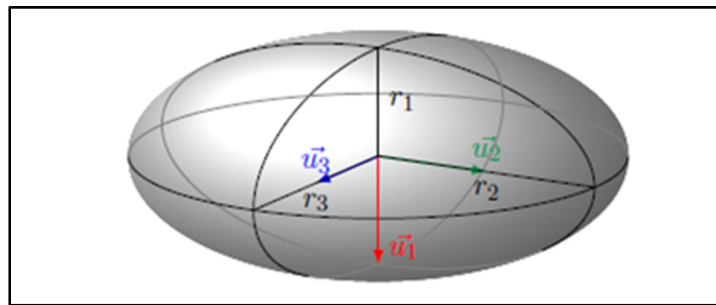
Figure 4: Definition of the dimensions and orientation
of an ellipsoid taken from (M. Saby, 2013)

FE simulations were prepared using the equivalent ellipsoid approximation after real void morphologies were identified using x-ray tube microtomography. Numerical inconsistences were exposed in the latter stages of void closure corresponding to the contact between internal surfaces. Nevertheless, even for tortuous voids, this transpired after 80% of void closure had already occurred.
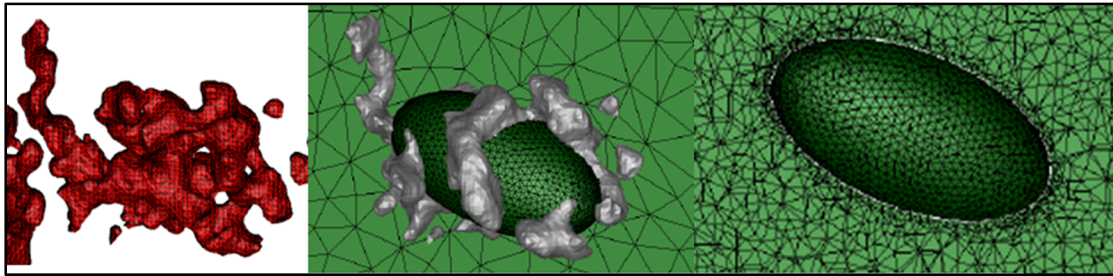
Figure 5 : (From left to right) Transformation from real morphology to equivalent ellipsoid taken from Saby (2013)

1.4 Influence of hot forging on void closure

Forging processes are an essential step in the fabrication of a sound material. Void closure requires energy, in the case of hot forging, an increase in temperature coupled with energy transferred from exterior loadings in the form of plastic deformation, strain energy and void surface energy is produced. A major secondary effect is the activation of particle diffusion, necessary in the healing stages of void closure.

1.4.1 Principal hot forging techniques

A handful of hot forging techniques are used in today's industrial climate. Open die forging or smith forging is paramount for workpiece sizes debuting as large ingots. Closed die forging is used for smaller parts and will therefore be omitted. The process of Upsetting and Cogging make up the prominent duo that lay the foundation a forging fabrication process. A brief description of these two hot forging operations follows.

1.4.1.1 Upsetting

Upsetting is a shape transformation technique for cast ingots in hot forging that consists in applying pressure to one side of a workpiece along its principal axis with flat a die. The aim of this process is a reduction in height which comes accompanied by an increase in width of the workpiece. Main process parameters include initial and final die heights. Heat transfer conditions and existing friction between die face and ingot can cause barreling if left unmonitored. Azushima et al. (2012) showed that the correct choice of lubricant can significantly reduce this phenomenon. High viscosity lubricants allowing for uniform displacements. Low viscosity fluids were shown to create a non-uniform distribution, increasing from the counterpoint to the periphery.

The compressive forces fathered from the upsetting process can be beneficial to the closure of internal voids or other defects engendered during casting. Lee et al. (2011) determined a non-unique response in void closure to upsetting. Various void behaviours were observed, depending on size and position in the large ingot. Hydrostatic stresses around the void were shown to switch from tensile to compressive to tensile conditions. Effective strain of over 0.6 was indicated to validate void closure conditions.
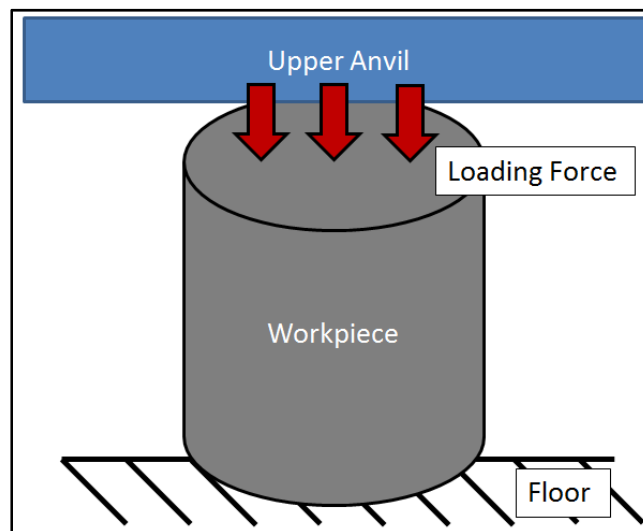
Figure 6 : Upsetting diagram

1.4.1.2 Cogging

Cogging or drawing out often follows the upsetting process in the forging of long, square, octagonal or circular sectioned, steel slabs. The operation takes place in steps, generally starting at one end of the workpiece and finishing at the other. The repetition of these steps is alternated with the rotation of the workpiece in order to reduce thickness and increase length.

Cho et al. (1998) investigated the cogging process design using Conventional flat (CV) and Free Mannesmann (FM) dies (Figure 7). FM dies proved more efficient, increasing hydrostatic stresses in the ingots center. Bite width was also evaluated, concluding that optimal parameters were obtained using 40 to 75% of the width of the die. Quicker forging can be accomplished using a smaller bite, increasing thickness reduction. Kakimoto et al. (2010) demonstrated that a reduction ratio of 75% was necessary in order to achieve soundness in the material matrix.

(a) CV die forging   (b) FM die forging
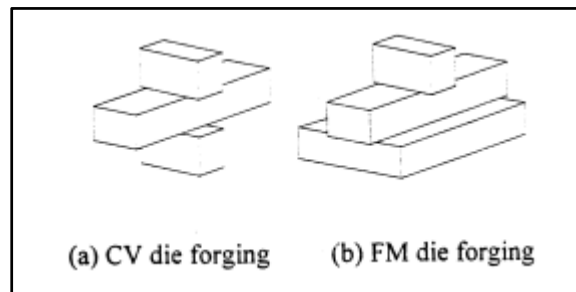
Figure 7 : CV and FM models for the
cogging process

1.4.2 Influential material and process parameters

The deformation occurred by applied external loading during industrial processes have been found to be the main source of void closure. Hydrostatic pressure was shown to be of high importance by Keife and Ståhlberg (1980) and the parameter, Q, based on this characteristic

was established by (Tanaka et al. 1986). The variable is calculated as the integral of stress triaxiality with regards to equivalent deformation.

$$Q = \int_0^{\bar{\varepsilon}} -T_x d\bar{\varepsilon}$$

(1.6)

A void closure parameter (VCP) was later proposed using numeric integration. Further work by Kakimoto et al. (2010) emitted a threshold value $Q \geq 0.21$ for complete closure of an axisymmetric cylindrical drilled hole. The method for process optimization gave encouraging results. However, the modelling of an internal void with only drilled through hole could be seen as unrealistic and too simplistic, giving way for debate. More recent work by Chen and Lin (2013), extended the void closure criterion to a tridimensional space, using a phenomenological expression to correlate the established functions to ellipsoidal voids. FE simulations were used to identify model constants relative to void locations within the workpiece.

Works by Gurson (1977), Budiansky et al. (1982), Duva and Hutchinson (1984),Ragab (2004), Zhang and Cui (2009) and Saby (2013) all emphasise the importance of a trio of process and material parameters. The first, relating to the Q parameter is the stress triaxiality ratio. The second, hand in hand with the hot forging process is the level of deformation, directly related to the industrial process. The final parameters are the materials Norton and strain sensitivity exponents. The analysed void closure models that appear later in this work hypothesise a direct relationship between these two entities.

$$n = \frac{1}{m}$$

(1.7)

1.4.3   Material behaviour during void closure

1.4.3.1   Local thermodynamic conditions in the workpiece

Process loading paths are directly responsible for internal void closure during hot forging. The application of a significant pressure and temperature induces a modification to

mechanical parameters such as strain, strain rate and internal stress on an elemental level. The modelling of this process typically includes a Representative Volume Element (RVE), or a cube of material, presented in Figure 8. Classic local thermodynamic boundary conditions are defined such as mesoscopic loading conditions given by Saby et al. (2013). The considered RVE possesses conditions of symmetry on three adjoining faces. Normal pressures σ_{xx}, σ_{yy} and a given velocity V_z are applied to the remaining faces. RVE dimensions are subject notably to the dimensionless volumetric ratio, η , respectively void over cube. This ensures parameter homogeneity in the cube, a necessary initial hypothesis.

Works including Saby (2013) and Tkadlečková et al. (2013) show the majority of voids and cavities to be located along the centerline and upper half of extra-large ingots. Boundary conditions for the represented RVEs are to be found using full field simulations. Adopting the mesoscale approach means defining selected positions within the ingot used as a basis for future analysis to provide the necessary thermodynamic RVE loading information. Importance is given to ensuring homogenous mechanical variable values for each calculated time step. Current mathematical void closure models, lacking the effects of local microstructure, validate the former premise.
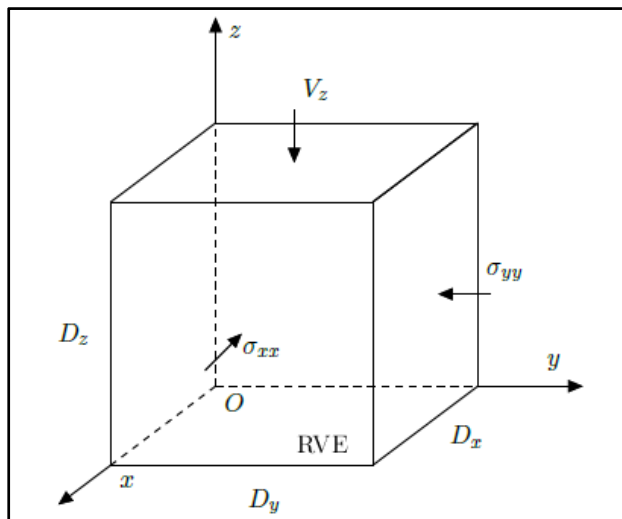
Figure 8 : RVE with applied boundary conditions

Taken from Saby (2013)

1.4.3.2   Effect on the local microstructure

Very little research has appeared on the effect of the local microstructure on void aspects in crystalline materials. Carroll et al. (2012), however, analysed the effect of local grain size on stress concentration around a void-like structure. A Dimensionless parameter denoting relative void to grain size was adopted in order to quantify the phenomenon. Grain size and anisotropy were shown to have a significant influence over the dominant mechanism causing strain in the material around the void. For a void to grain size ratio of 1 or less, the stress of a cylindrical through hole was commanded by the grain anisotropy whereas the effect was lesser for larger ratios. Concluding remarks on material behaviour were that the closer the characteristic void dimensions came to the microscopic scale (grain size), the more local elastic and plastic deformation were affected by the fluctuation in grain heterogeneity and grain orientation, see Figure 9. This was demonstrated with data collected using the Scanning Electron Microscope (SEM) and Electron Backscattered Diffraction (EBSD) measurements.

Even if the work was solely linked to grain size, it gives thought to how the microstructure may affect void closure during hot forging. If anything, it has proven the necessity to adjust classical void closure models and FE simulations to account for microstructural conditions. Roux et al. (2013) noticed this tendency and created a level set and anisotropic adaptive remeshing strategy for the modeling of void growth under larger plastic strain.
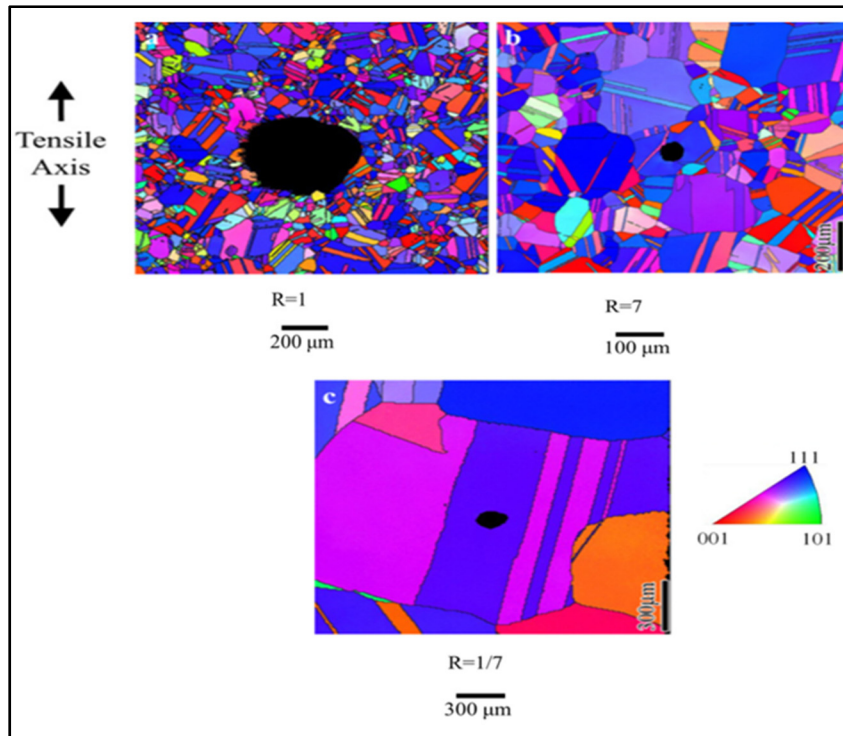
Figure 9 : Resulting local grain orientation for various values of
void to grain size ratios

1.4.3.3   Healing

Park and Yang (1996) deduced the existence of two stages in the closing of voids in large ingots, healing qualifying as the second stage in successful void closure. The current work isn't focused on this aspect of the closure mechanism. Nevertheless, it was found to be beneficial in understanding future challenges.

After mechanical closure, the void's volume has been theoretically reduced to zero. Contact has been achieved between internal surfaces and bonding must begin in order to restore superior material mechanical properties. The completion of this phase indicates a sound workpiece. Song et al. (2014) emitted the following basic assumptions and key issues with healing. Primary factors include the provision of material and energy. Fundamental sources incorporate internal surfaces, the material lattice and interface diffusion. Energy is provided

through exterior loading and temperature gradients. Diffusion plays an overriding role during the process and therefore implies a strong dependency on the materials chemical make-up. Several notable stages were defined. An initial fast healing stage followed by a reduction in healing speed. Closing stages displayed acceleration in healing caused by surface and interface diffusion. The completion of the healing process was shown to be controlled by lattice diffusion.

1.5   Comparison of existing void closure models

This section gives up to date compilation and comparison of existing void closure models, each using its own set of hypothesis, justified by the studied working scale. This extensive analysis considers models potentially viable for application to industry. Table 1 summarizes the reviewed void closure models.

Model	Scale	Type	Constants	Equation	Tendency
STB	Macro	Empirical	K_c=5	Eq. (1.8)	Linear
Ragab (2004) derived from Gurson-Tvergaard	Macro	Analytical	q_1=1.5, q_2=1	Eq. (1.10)	Exponential
Budiansky et al. (1982)	Micro	Analytical		Eq. (1.11)	Exponential
Duva and Hutchinson (1984)	Micro	Analytical	c_1,c_2, (Table 2)	Eq. (1.13)	Exponential
Zhang and Cui (2009)	Meso	Analytical		Eq. (1.17)	Exponential
Zhang et al. (2009)	Meso	Semi-Analytical	c_1,c_2,c_3,c_4 (Table 3)	Eq. (1.18)	Exponential
Saby (2013)	Meso	Analytical		Eq. (1.20)	Polynomial

Table 1: Summary of presented void closure models

1.5.1   STB model

The Stress Triaxiality Based (STB) Model was first used in Forge ®, a finite element forge prediction software, as a user defined subroutine implemented by Lasne (2008). The

description is a simplest function correlating void volume variation with stress triaxiality ratio and incremental strain. Considering a constant stress triaxiality ratio and the absence of any initial strain, an affine void closure function can be deduced, as shown in Equation (1.8).

$$\frac{V}{V_0} = 1 + K_c T_x \bar{\varepsilon} \tag{1.8}$$

The value of $K_c \approx 5$ was obtained through a series of simulation tests looking at spherical voids in a cuboid matrix. The numerical constant is also preprogrammed into Forge2011. The function's slope becomes negative taking into account a compressive material state ($T_x < 0$), and the strain range limited to $\bar{\varepsilon} \in \left[0, \dfrac{-1}{K_c T_x}\right]$. The model's limitations, induced by a macroscopic approximation, explain the discrepancies observed with real void closure. The model was observed to converge rapidly, overestimating the effect of far field strain on void closure for higher strain values.

1.5.2   Ragabs derived work of the Gurson-Tvergaard model

Introduced in 1977, Gurson (1977) established a model for rigid perfectly plastic porous materials. This considered state is denoted mathematically as $m \rightarrow 0$, Equation (1.7). Void evolution is based on the void volume fraction, f, present in the workpiece, and the plastic strain rate tensor, $\bar{\bar{\dot{\varepsilon}}}_{pl}$.

$$\dot{f} = (1-f)tr(\bar{\bar{\dot{\varepsilon}}}_{pl}) \tag{1.9}$$

Solely focusing on void closure, Ragab (2004) simplified Gurson's yield function hypothesising axial symmetric void deformation in order to formulate an expression to evaluate the volumetric strain rate $\dfrac{\dot{V}}{\dot{E}_e V}$. In the case of compressive stresses, $T_x \leq 0$, the integrated void closure function can be expressed as

$$\frac{V}{V_0} = \exp\left[-E_e \frac{3q_1 q_2}{2} \sinh\left(-\frac{3}{2} q_2 T_x\right)\right] \tag{1.10}$$

The values of the numerical constants were determined by Tvergaard (1982) upon Gurson's yield criterion. The calculated values are $q_1 = 1.5$ and $q_2 = 1$, corresponding to the closure of a continuously spherical void. Other authors have alleviated the initial expression of void volume fraction, but these studies do not correlate with the framework of the current thesis. Although widely used in void closure prediction models, the mathematical expression fails to account for material dependency.

1.5.3   Budiansky's model

Budiansky et al. (1982) and derived works from Tvergaard (1984) provided mathematical models for nonlinear viscous materials. Two formulae were obtained using the Rayleigh-Ritz Method as analytical solutions were shown to be infeasible. The respective equations were assigned to high and low stress triaxiality (HST, LST) rates. Low stress triaxiality being defined for $|T_x| \square \ 1$. Both formulae show similar results for stress triaxiality rates close to 1. Discrepancies between the two models are observed for Tx≠1, see Figure 10. Under compressive stress the HST volumetric strain rate is integrated as follows.

$$\left(\frac{V}{V_0}\right)^{HST}_{sph} = \exp\left[-E_e\frac{3}{2}\left(-\frac{3m}{2}T_x + G(m)\right)^{\frac{1}{m}}\right] \tag{1.11}$$

$$\text{With } G(m) = (1-m)(1+\frac{2\pi}{9\sqrt{3}}) \ , \ \forall T_x \leq 0 \tag{1.12}$$
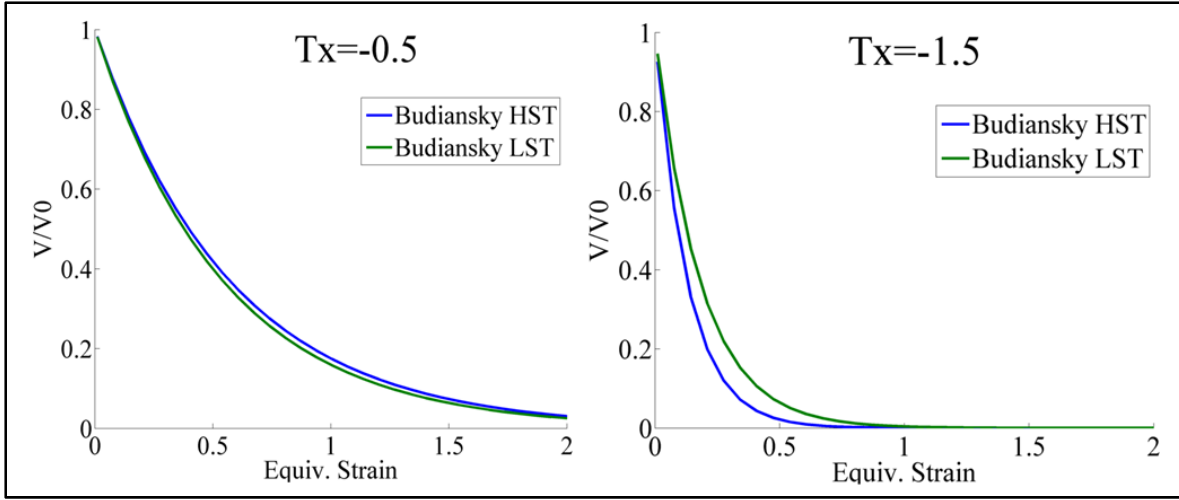
Figure 10 : Spherical Void Evolution for Budiansky's HST and LST Void Closure Models

1.5.4   Duva and Hutchinsons modified model

Duva and Hutchinson (1984) added the c_1 and c_2 coefficients to Budiansky's model, creating a unique volumetric strain function (1.13) for both Low and High Stress Triaxialities. The model successfully corrects the underestimation of the effect of the deformation rate in Budiansky's HST model as a consequence of its velocity field hypothesis. A comparison between all three models is available in Figure 11.

$$\left(\frac{V}{V_0}\right)_{sph} = \exp\left[-E_e\left(\frac{3}{2}\left(-\frac{3m}{2}T_x + G(m)\right)^{\frac{1}{m}} - c_1T_x + c_2\right)\right]$$

(1.13)

The factors c_1, c_2 are strain rate sensitivity-dependant. The corresponding values were indexed by Zhang and Cui (2009) using the Rayleigh Ritz method and can be found in Table 2.

m	0.01	0.1	0.2	0.3	0.5	1.0
c_1	1.0066	0.9002	0.7061	0.8049	0.5951	0
c_2	-0.8329	-0.7874	-0.6571	-0.7340	-0.5479	0

Table 2: Values for the coefficient c_1,c_2 in Hutchison's formula taken from Zhang and Cui (2009)
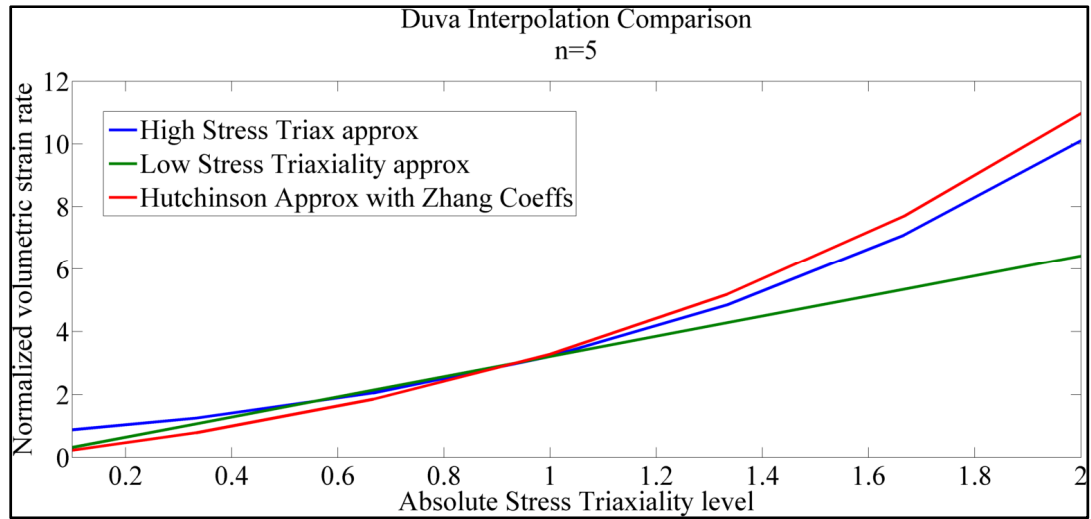
Figure 11 : Duva's Interpolated volumetric strain rate, Budiansky comparison

The interpolated function admits a maximum error of around 25 percent for extreme Norton exponent values and for stress triaxiality states close to 1 in comparison to both Budiansky's HST and LST approximations and their respective intervals of validity.

1.5.5   Zhang and Cui's analytical model

Zhang and Cui (2009) proposed a void closure model capable of predicting void closure accounting for void shape evolution during hot forging in regards to its shape parameter $\lambda = \dfrac{a}{b}$, representing the quotient of the voids semi minor and major axes, see Figure 12. Special values of this coefficient are obtained for $\lambda = 1$ and for $\lambda \to 0$, depicting respectively a spherical void and a penny shaped crack.
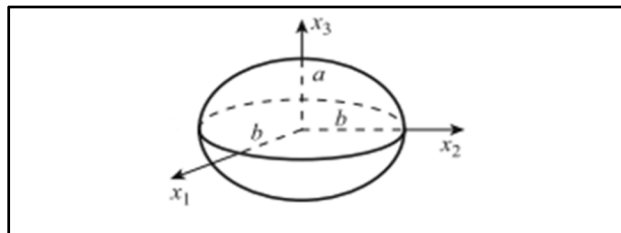
Figure 12 : Void represented with a and b
parameters taken from Zhang and Cui (2009).

The volumetric strain rate for a sphere is given by Duva and Hutchinson (1984) , application of Equation (1.14) for any value of stress triaxiality.

$$D_{sph} = \frac{3}{2}\left(\frac{3m}{2}|T_x| + G(m)\right)^{\frac{1}{m}} + c_1|T_x| + c_2, \quad \forall T_x$$

(1.14)

The Rayleigh Ritz procedure and the variational principle were also applied to the amended analytic function by He and Hutchinson (1981) and the following approximate volumetric strain rate was identified.

$$\frac{D_{cr}}{\lambda} = \frac{1}{\lambda}\frac{6}{\pi\sqrt{1+3m}}\left(|T_x| + \frac{2}{3}\right) \quad \text{for} \quad \lambda \square 1$$

(1.15)

In order to correlate with Budiansky's formula (1.11) for spherical voids with $m=1$ a closed form expression is calculated. Here $\dot{\lambda}$ is the change rate of the void's aspect ratio.

$$D_{\dot{\lambda}} = \left(\frac{\dot{\lambda}}{\dot{E}_e}\right) = 2.5 - (1-m)\left[(29-45m)\left(1 + \frac{3}{3T_x - 2}\right)^3 - \frac{2}{9}\right]$$

(1.16)

The conclusion of Zhang's aspect crack ratio work was a model that accounted for the transition from a spherical void to a penny shaped void during the latter stages of closure. The change in void volume relatively to the matrix is shown to be dependent on the materials Norton exponent, stress triaxiality and effective strain as far field variables.

$$\frac{V}{V_0} = \left|\frac{D_{\dot{\lambda}}\exp(-D_{cr}E_e) - D_{cr}\exp(-D_{\dot{\lambda}}E_e)}{D_{\dot{\lambda}} - D_{cr}}\right|\exp(D_{sph}E_e)$$

(1.17)

The formula is a weighted relative error between the crack like form and the change rate aspect balanced by the volumetric strain rate for spherical voids.

1.5.6   Zhang's semi-analytical model

Further work, Zhang et al. (2009) , established a criterion focusing on the macroscopic strain effect during void closure. An initially spherical void was considered and void shape change accounted for. Four constants were introduced and calculated using FE simulations on a cubic cell model under axisymmetric remote stresses, see Table 3. The formula for void

volume evolution, Equation (1.18), was obtained after integration of the volumetric strain rate.

$$\frac{V}{V_0} = \exp\left[-E_e\left(\frac{3}{2}\left(\frac{3m}{2}|T_x| + G(m)\right)^{\frac{1}{m}} + c_1|T_x| + c_2 E_e^2 + c_3 E_e^4 + c_4\right)\right]$$

(1.18)

Numerical simulations with this model were shown to be in good correlation with data obtained by Lee and Mear (1999). This model shows greater accuracy when compared with classical damage definitions in the case of void closure. Significant evolution of an initial spherical void occurs, collapsing in latter stages due to internal surface contact, explaining the decrease in the collapse rate. FE simulations were also developed and compared to the former description. Again, the results showed a stronger correlation to the semi-analytical void closure model in comparison with other classical models, particularly for lower stress triaxiality states.
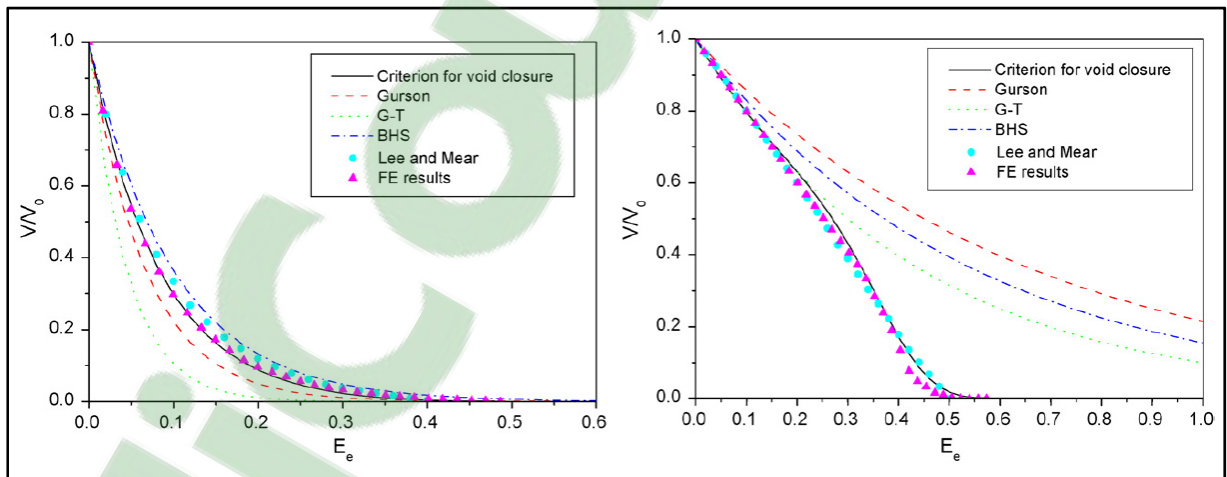
Figure 13 : Zhang semi analytical compared to other void closure models, experimental and FE results for Tx=-2 and Tx=-0.6, taken from Saby (2013).

m	0.01	0.1	0.2	0.3	0.5	1.0
c_1	6.5456	2.9132	0.6016	1.1481	0.4911	0.5048
c_2	-15.3775	-11.6464	-0.6981	-4.2026	0.8002	6.4675

c_3	324.4417	185.5622	72.6397	108.2114	53.8018	14.2610
c_4	-1.9575	-0.6511	-0.1243	-0.2480	-0.2314	-0.3379

Table 3: Values for the coefficients c_1,c_2,c_3,c_4 in Zhang's equation
taken from Zhang et al. (2009)

1.5.7   Saby's CICAPORO model

Introduced in 2013, the CICAPORO model represents void closure with a strong emphasis on initial void geometry. Morphology equivalent ellipsoids are used and the matrix material follows the Hansel-Spittel law:

$$\sigma_0 = A(\bar{\varepsilon} + \varepsilon_0)^n \dot{\bar{\varepsilon}}^m e^{m_4/(\bar{\varepsilon}+\varepsilon_0)} \tag{1.19}$$

This description denotes a dependency both on strain hardening and softening, n, m_4 and on strain rate sensitivity, m. The value of A characterizes a model optimisation parameter. The current material behavior law is an extension of Budiansky et al. (1982) and Tvergaard (1984) for a strain rate sensitivity depend-only model. An analytical function was chosen as

$$\frac{V}{V_0} = A + B\bar{\varepsilon} + C\bar{\varepsilon}^2 \tag{1.20}$$

The initial void volume condition implies that A be equal to 1. The numerical value of the B and C criterion depends on case sensitive parameters.

$$B = \sum_{i=1}^{3} \sum_{j=0}^{2} \sum_{k=0}^{1} b_{jk}(T_x)^k (\gamma_i)^j p_i \tag{1.21}$$

$$C = \sum_{i=1}^{3} \sum_{j=0}^{2} \sum_{k=0}^{1} c_{jk}(T_x)^k (\gamma_i)^j p_i \tag{1.22}$$

The p_i symbolize linear dependant void orientation, T_x the stress triaxiality ratio, and γ_i a non-dimensional geometric ratio between initial void volume and ellipsoid principal direction radii. The b_{jk} and c_{jk} coefficients were obtained using different regression techniques.

Void closure in advanced stages, $\frac{V}{V_0} \leq 0.2$, was shown to be less accurate because of the chosen ellipsoid shape evolution. However comparison with real void morphologies for closure $\in [1, 0.2]$ displayed an excellent likeliness.

1.6 Characterisation techniques

This section describes the main modern-day non-destructive void characterisation techniques used in metal forming industries. The main challenge lies in the size of the final workpiece. Void detection in large ingots is possible. However, current high resolution void analysing and visualisation technology is only available for smaller metal samples. The acquisition of a tri-dimensional image is not only used to characterize the void's morphology, but also implemented in FE software, meshed and simulated to study a materials susceptibility to void closure.

1.6.1 Traditional void characterisation

Upon realisation of insufficient mechanical health due to void apparition, industries would traditionally use destructive metallographic techniques to analyse the extent of development. For obvious reasons, non-destructive characterisation techniques were deemed preferential leading to the adoption of ultrasonic waves for the metal working environment. Defect detection via ultrasound for on the spot structural health monitoring persists today as a viable inspection technique as shown by Zhang (2016).

The physical principle is simple. The variations of wave echoes are interpreted as a modification in the studied materials internal structure. The emitted regular wave pulse is disturbed by the presence of discontinuities such as voids or inclusions and reflected back to the detector. The received electronic signal is analysed and visualised on screen as intensity vs distance. High intensity pics symbolise flaw detection. Ultrasonic testing provides the advantage of being able to investigate internal material structure not only on the surface but

also in the bulk of the workpiece. Difficulties in the application of this technique include surface curvature, roughness and lack of parallelism.

Szelążek et al. (2009) studied the application of acoustic birefringence as a measurement for the evaluation of material degradation. An encouraging technique for void detection in metal samples was found to depend on shear wave velocity changes. A shear wave is propagated in the direction of material thickness and polarized in two orthogonal directions, those of the materials acoustic axis. The birefringence, B, in steels, depends on material texture or preferred grain orientation and internal material stress state. The measure of acoustic anisotropy is calculated as in Equation (1.23):

$$B = 2.\frac{V_{12} - V_{13}}{V_{12} + V_{13}} = 2.\frac{t_{13} - t_{12}}{t_{13} + t_{12}}$$

(1.23)

V_{12}, V_{13} the velocities of the shear wave and t_{12}, t_{13} their respective time of flight in the direction 1, polarized along 2 or 3. It is interesting to note that this expression of birefringence is independent of actual material thickness at the time of measure. Wave velocities were found to be function of void densities, size and orientation in comparison with the wave's direction of propagation, therefore proving this technique to be a significant quantification parameter for the detection of internal defects.

1.6.2   Microtomography

1.6.2.1   3D microtomography

3D Tomography is an imaging technique through sectioning. The basic principal lies with the materials interaction to a penetrating wave. The information received by the equipment's detectors is reconstructed to form 2D cross sections of the analysed sample. The 2D sections are cross referenced with a projection of the 3D form and reconstruction algorithms are used to generate a 3D image. The advantages of this technology lie in the precision of the reconstructed image and the range of material application including metal matrix composites, metallic foams and alloys. The current method of identification is often employed for

studying microstructures or material defects such as inclusions, pores and voids as studied by Lecarme et al. (2014). The clear visualisation of the internal structure incorporates an improved shape description and has led to a breakthrough in applied 3D material modelling. This technique also caters for real time experiments including material compression. Observations encompass images differentiating between the workpiece's core and surface.

1.6.2.2   X-Ray microtomography

X-ray microtomography is a recent widely-used non-destructive tridimensional material analysis technique. Scientific application was studied by Maire et al. (2001). As in any tomography technique the acquisition of a 3D image requires two stages. The first entails obtaining sampled information, the second details its reconstruction. The sample is placed on a rotating support between the detector and the x-ray source. In general one complete rotation will become hundreds of images. The precision of the tomograph is function to the preprogrammed angular discretization. Initial x-ray technology used an x-ray tube as the source of photon emissions. The resulting image resolution reached 10 microns voxel size. Photons are accelerated by means of a difference in electric potentials ranging from 220kV and 450kV. Each sample must be studied to find optimal imaging parameters. Image sharpness is function to the sources focal. A radiograph obtained using a reduced acceleration tension will emit a sharper image, but can only be used on a sample with reduced thickness. To the contrary, larger samples require more energetic photons, reducing radiograph quality. The consequential beam emitted by this technology has the form of a cone, see Figure 14. (Lee et al. 2007) studied a porous steel specimen displacing the object in the x-ray tube's conic beam thus achieving magnification of the final image.
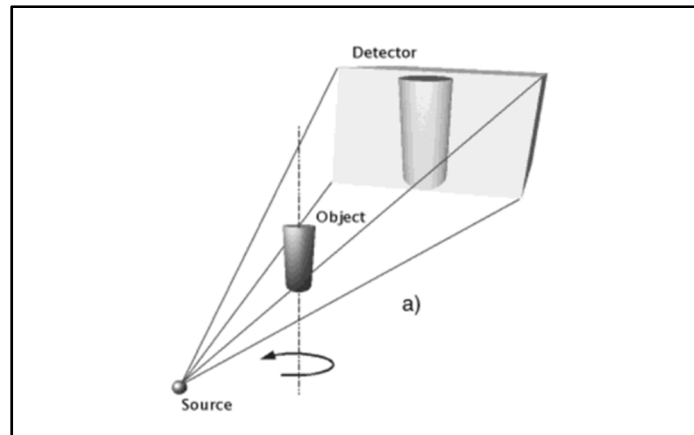
Figure 14 : X-ray tube Microtomography image
acquisition principle taken from Maire et al. (2001)

Beer-Lamberts law is used to associate the materials attenuation coefficient, alpha, to the
beam's intensity.

$$I = I_0 e^{(-\alpha D)} \qquad (1.24)$$

I_0 is the incident intensity and D the length of the path travelled by a photon.

1.6.2.3 Synchrotron X-Ray microtomography

The most recent micro-tomographs use synchrotron lighting. The last decade has proved this
new technology to be more clear-cut than its predecessors. Frequently used for steel imaging,
the light source provides a more energetic wave resulting in a higher percentage of material
interaction, consequently improving image precision. Used to study the evolution of voids
under compression in steel and other alloying metal samples, Everett et al. (2001) and Toda
et al. (2009) obtained tri-dimensional images providing a resolution around 1μm voxel size.
Unlike x-ray tube technology a parallel beam is emitted by the source, see Figure 15.
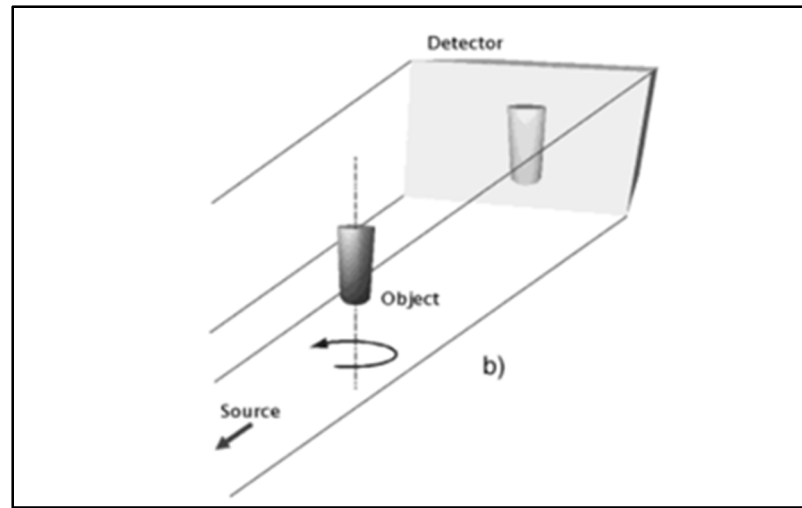
Figure 15 : Synchrotron X-ray Microtomography image
acquisition principle taken from Maire et al. (2001)

1.6.3   3D Reconstruction software

Various reconstruction algorithm software exist that produce a 3D grayscale image after numeric treatment of the 2D projections. The resulting imaging depends notably on the 2D radiographs taken during the 360º snapshot session. The detectors sensitivity range and transmitted light intensity are key factors to the amount of noise present on the final render. Image filtering is applied to eliminate unwanted noise. The median filter was shown to produce encouraging results, omitting greyscale noise without compromising image sharpness. The presence of lighter and darker zones is the result of a beam interaction surface phenomenon such as beam hardening and reflection. Treatment of these image defects include the *background subtraction or Rolling Ball* algorithm, established by Sternberg (1983). A decision is made on the level of details to be eliminated after computation of a background image, excluding extreme light and dark zones. Saby (2013) used x-ray tube micro-tomography to determine the presence of voids in a JD20 sample, see Figure 16.
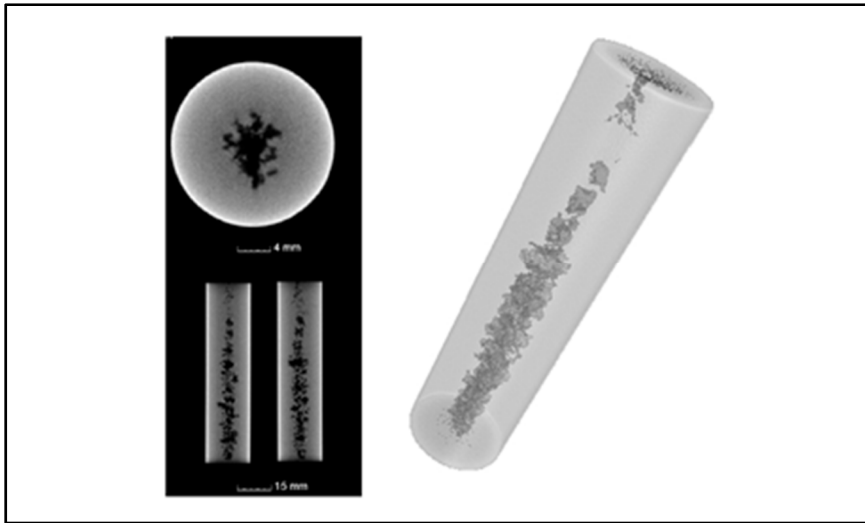
Figure 16 : 2D cross sections and consequential raw 3D image
of JD20 steel sample taken from Saby (2013)

CHAPTER 2

PRELIMARY ANALYSIS OF THE OPEN DIE FORGING PROCESS

2.1   Industrial partner and process selection

The current M.A.Sc was carried out in collaboration with FINKL Steel, a metal transformation company specialised in high performance steels. Time was accorded to visit one of the subsidiaries, Sorel Forge, in order to analyse the current open die forging process.

Sorel Forge manufactures numerous parts, all various sizes. The largest cast ingot is 63 inches in diameter and was selected for initial geometry in order to respect the framework of this thesis.

The shape most often forged from the 63'' ingot is a parallelepiped, and more precisely, a rectangular prism. Internally, the process is known as slab forging. This process was selected for the current study.
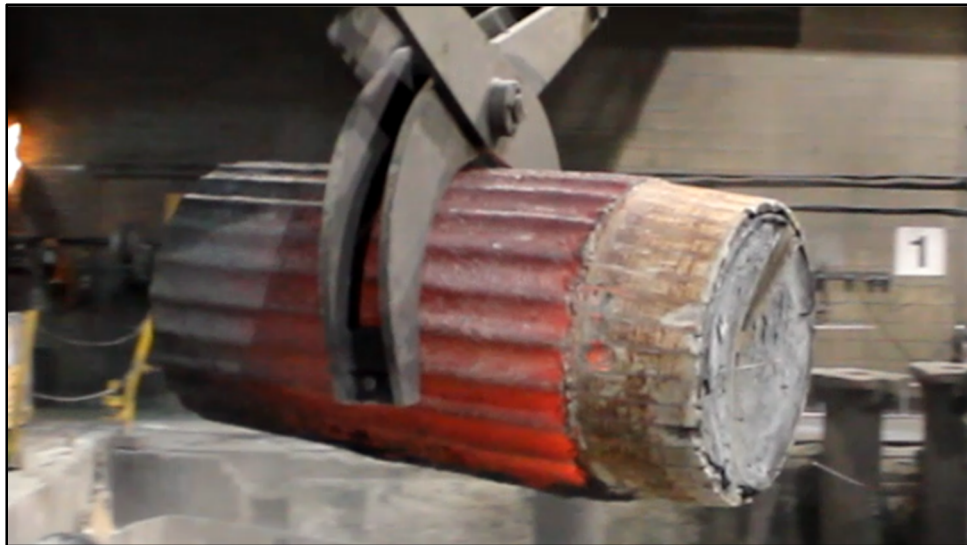
Figure 17: 63" cast ingot after demoulding

2.2 Forging sequence identification

Observations were made during normal part production in order to qualify the different sequences that make up slab forging. A number of forgings were filmed using two different camera angles for future reference and analysis. A GoPro Hero3+ was placed in the forger's cabin directly in front of the forging press. A Canon EOS Rebel T3i was placed filming at 90 degrees respectively to the former to capture the cross section morphology evolution.

Initially the cast ingot is flame cut to separate the feeder head (hot top) from the body of the casting. The feeder head is represented by the non-fluted surface in Figure 17. The ingot is then preheated to 1250°C until obtaining a homogenous temperature. The ingot is transferred from the furnace to the press using a clamp on bridge cranes. A manipulator grasps the part, allowing for travelling (horizontal translation) and rotation around the travelling direction. The large forging press is a 5000T hydraulic press. The upper die can only move vertically, whereas the lower die is attached to a metal plate (floor level) which can translate horizontally.
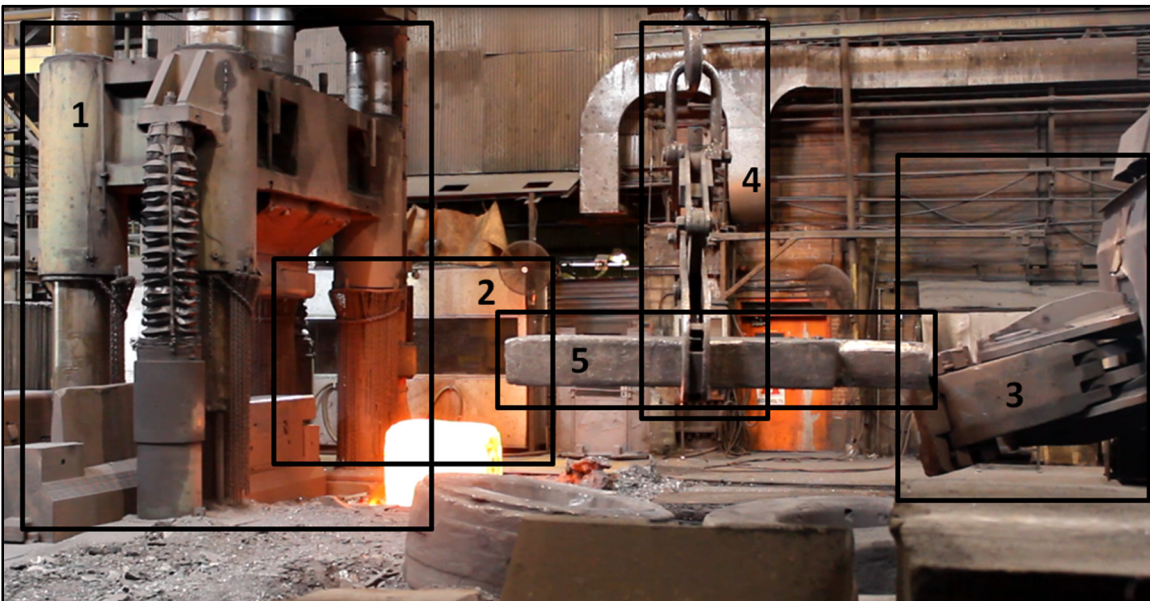
Figure 18 : The forge; 1: The press. 2: The forger's cabin. 3: The manipulator. 4: Bridge crane clamp. 5: Intermediate die.

2.2.1 Sequence 0: Initial forming

Initially, the top of the ingot, extreme left in Figure 17, is held by the manipulator. The ingot is worked with both the upper and lower press dies. A slight deformation is applied to the ingot side, which can be characterised as a side-upsetting. The manipulator rotates the part 90 degrees around the ingots longest dimension and the operation is repeated in order to obtain a square base and squarer sides. Dimensions vary from an average base primitive cylinder diameter of 63 inches to a 49.5 inch square base. Initial forming was not retained as a significant transformation sequence because of the minor shape modification, low levels of deformation and consequential induced stresses.
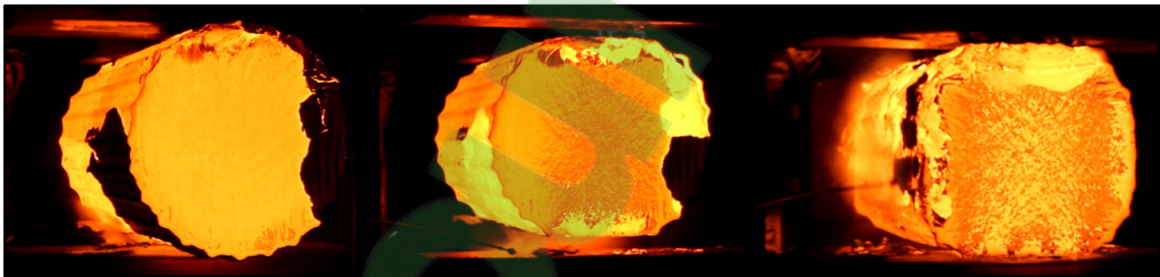
Figure 19 : Initial forming: Steps for obtaining a square base

2.2.2 Sequence 1: Upsetting

After having formed a square base, the part is manipulated upright and placed on the metal plate (floor level). The manipulator will always hold the part upon initial deformation whilst working with a part in contact with the floor. When the part is stable, the manipulator releases.

The first hit aims to remove the dish stool print left after casting, see Figure 20, a) and b). The intermediate die, #5 in Figure 18, is placed between the upper die and the flat ingot top for the second hit. This procedure spreads the forging force for an equal distribution on the

entire ingot top. The sequence ends when the height upset represents around 35% of the initial ingot height.

This sequence is notable for the deformation induced upon the workpiece. The reduction in height produces an increase in workpiece diameter. The geometry after sequence is considered as cylindrical and the barrelling effect is accounted for.
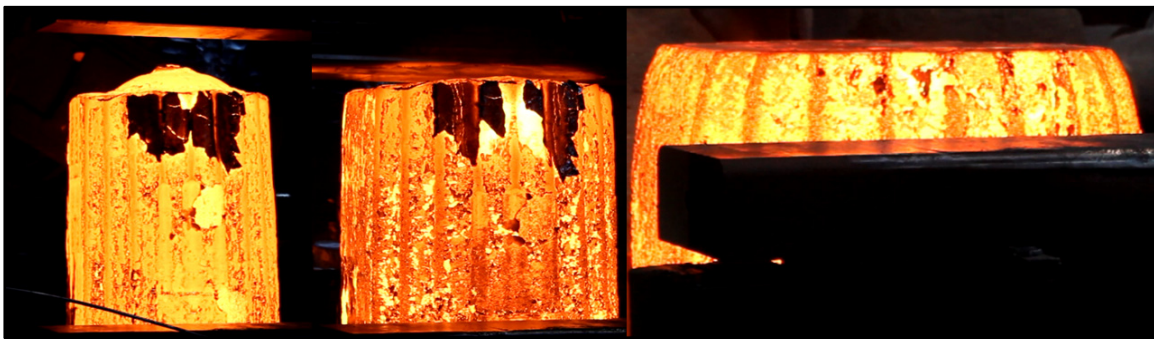
Figure 20 : Upsetting a) Left: Ingot with dish stool, b) Middle: Dish stool removal

2.2.3 Sequence 2: FM process

The FM process (Free from Mannesman effect) is the most recent addition to the open die forging process at Sorel. This step is characterised by an additional deformation and aims to work the material that was displaced around the part's middle during upsetting.

After upsetting, the ingot is laid on its side and grasped by the manipulator. The intermediate die is also necessary for this sequence. The upper die closes the gap until contact is achieved between the intermediate die, the part and the floor. Part shape is considered as a quasi-cuboid, marking a notable change in workpiece geometry.

A second FM process, characterised as a FML (FM on the parts length), can occur if the part is not initially wide enough for final tolerances. The process is identical apart from the ingot having a different initial position. The second FM process will not be considered in a

generalised model of the forging process because it only being necessary for five percent of the observed forged parts.

Figure 21 : FM Process

2.2.4   Sequence 3: Cogging

The intermediate die is no longer necessary for the rest of the forging procedure. The part is constantly held by the manipulator, moving the ingot to and from the press. The lower die is used and remains still whilst the upper die translates vertically. The cogging process is the fusion of these two movements.

The part is worked in two steps. The half which is not held by the manipulator is forged before using the bridge crane for a 180 degree rotation and forging the second half. Part shape is considered as quasi-rectangular.

During forging, the press is used so that the material flows towards the free end of the ingot. This technique allows for a continual increase in part length considering strong topological changes. The billet is worked consecutively on its side and along its edge (alternative 90 degree rotations of the manipulator) until meeting specifications.

The billet is returned to the furnace for temperature re-homogenisation at the end of this process. The first four steps last over 30 minutes. Consequently, a considerable amount of energy has been lost during forging and a temperature gradient has developed. Therefore continuing to forge would induce surface cracks.
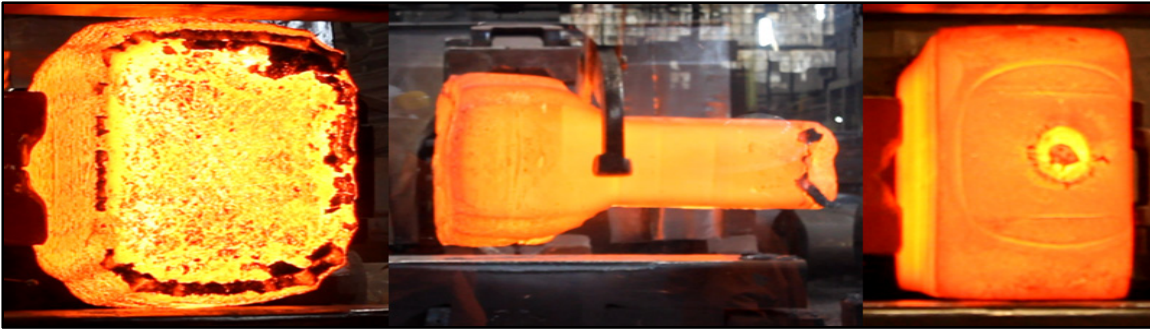
Figure 22 : Cogging Process

2.2.5 Sequence 4: Finishing

Finishing is the last notable sequence is the forging process, ending when the part meets specified tolerances. The deformation sequence is identical to that used during the cogging process. However, shape variation is minor: length and width are increased, height decreased. The functional dimensions are width and height, meaning the resulting length can be variable. An estimated overall length is given. Dimensions and tolerances are verified by the manipulator sensors combined with a laser line.

Figure 23 : Finishing Process

2.3 Process variability observation

Slab forging is an industrial forging process used hundreds of times each year. However, each forged part has unique specifications, mechanical characteristics and dimensional tolerances. This means that the process has to be repeatable, but will contain inevitably a

certain amount of variability. The most successful industrial processes are controlled and aim to reduce variability in order to produce standard parts that act as a base-line for product quality control and assessment. In order for a procedure to be controlled, indicators or variables must be defined. Observations during slab forging at Sorel Forge has led to establishing significant sequence indicators, see Table 4.

Table 4 : Indicators of process variability

	Indicator	*Unit*
For all sequences	Press velocity	mm.s^{-1}
	Force usage	%
	Process time	s or min
	Geometry evolution	mm*mm*mm
	Weight evolution	kg
	Sequence efficiency	%
For Upsetting and FM sequences	Total amount upset	mm
	Reduction	
For Upset only	Percentage of upset	%
For Cogging and Finishing sequences	Total number of passes	
	Number of bites per pass*	
	Bite depth per pass*	
	Bite width*	
	Half forging ratio	

*: Separate calculations are advised for work on height and width.

External factors can also cause process variability whilst forging, for example leaving open a factory door and letting a cold winter breeze accelerate ingot cooling. External factors will not be considered in this report for simplification reasons.

Process variability can be the cause of unsuccessful forgings. Current practice dictates that an unsuccessful forging be dealt with in one of three ways depending upon the seriousness of the defect:

- Surface crack repair, commonly known as scarfing. A blow torch is used to locally heat the ingot surface causing it to melt and then 'spread' the crack until it disappears.

- Reheating: Frequent surface crack repair is characteristic of excessive heat loss. In this case the part can be returned to the furnace.

- Re-melting: If the part cannot be recovered, it is melted down.

The indicators mentioned in Table 4 are each characteristic for a single forging. Therefore large amounts of data must be gathered and evaluated in order to validate the significance of the results.

2.4   Preliminary analysis

2.4.1   Data collection

In order to analyse the current forging process, data was obtained from sensors previously installed in the forge; two position sensors and one force measurement. The following models were available:

- Steel cable encoder on the upper die, BEI model: H25D-SS-2000-ABC-28V-EM15.

- Pressure effector, maximum limit 600bar, model: BN3060.

- Steel cable encoder on the manipulator.

The data was exported as .csv files and read with an in house Matlab code. The sampling period for the different sensors was from two to three seconds for data saved on the company server. Data could be saved instantaneously at a higher sampling frequency (every 5 milliseconds) at two hour time intervals. The second option was deemed non-viable because of the shear amount of information to process in relation to the precision gained in position

and force (20,000 lines to compute in comparison to 1000 lines per forging). The data representation from a typical forging is shown in Figure 24.
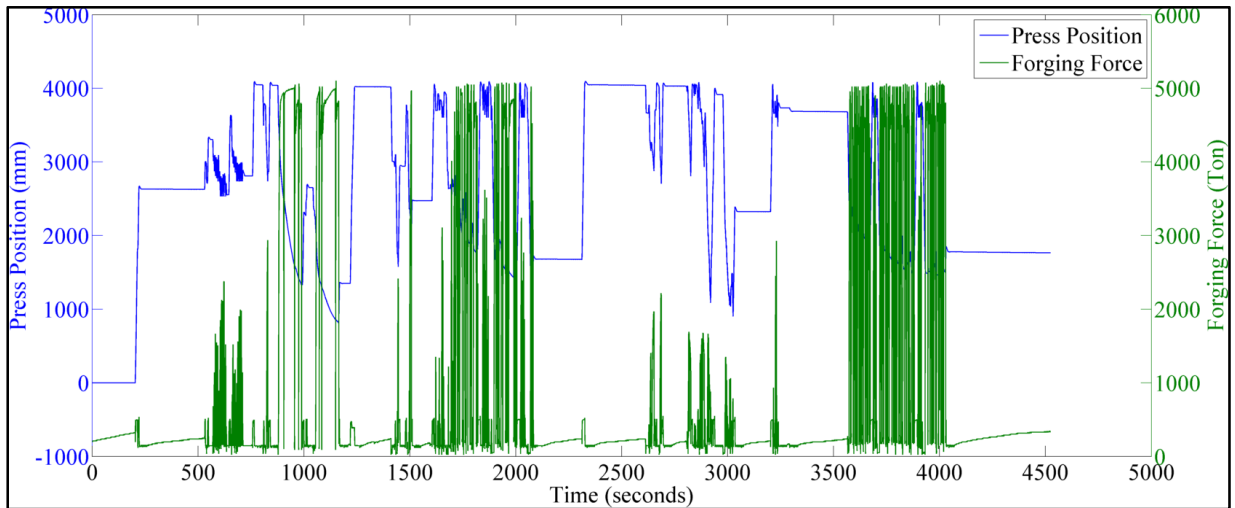
Figure 24 : Typical forging position and force graph

2.4.2   Forging sequence characterisation

The characterisation of each sequence was rapidly achieved after synchronising the video of each forging with the corresponding position and force graph. Three observations are necessary in order to successfully read the graphs:

- The press position sensor should be recalibrated every morning, setting the value '0' when the top and lower press dies initially come into contact.
- The maximal forging force observed is 5000T, which is in agreement with the press's capacity. The applied forging force is often the maximal forging force.
- A variation in press position without an increase in the corresponding forging force is insignificant and does not contribute directly to part forging.

The upsetting and FM sequences respectively the cogging and finishing sequences will be presented simultaneously because of the observed similarity in the position and forging data.

Upsetting and FM process:

Two working zones, defined by maximal forging force and a significant decrease in the press position, are visible in Figure 25. They are delimited between 850 and 1000s and 1060 and 1180s respectively. The decrease in press position is equivalent to the drop of the upper die in the direction of the ingot top. As the forging force increases, contact occurs. Forging is carried out for the duration of the increased forging force. The drop in press position during upsetting (Zone 1, 1877mm) is greater than during the FM process (Zone 2, 1143mm). However, maximal forging force is used in both cases for a similar length of time implying that the deformation during upsetting has left significant residual stresses in the material that need to be overcome during the FM sequence. The ingot must be rotated 90 degrees in between both sequences. The interpass time is calculated at 68 seconds in this case.
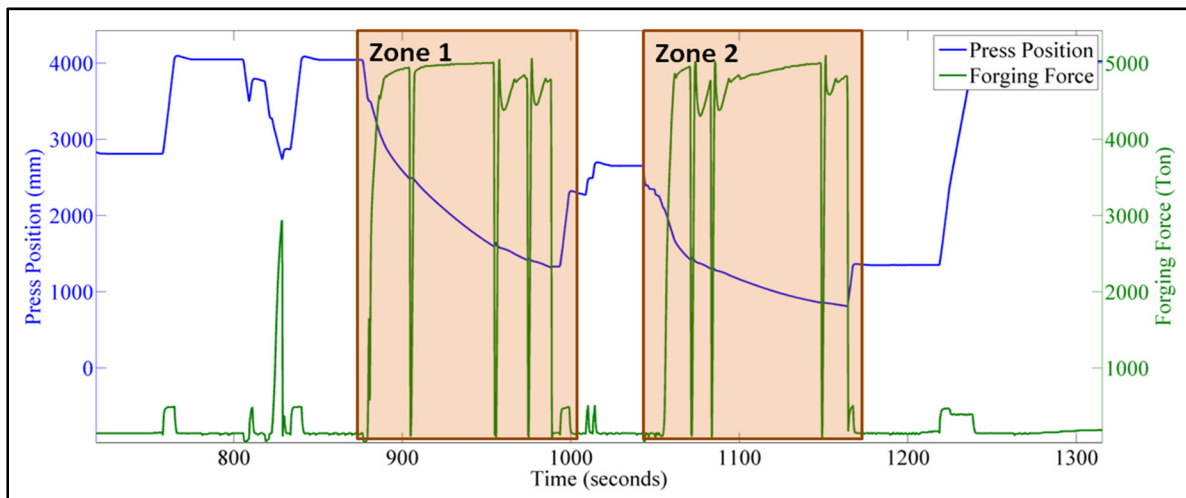
Figure 25 : Upsetting and FM characterisation

Cogging and Finishing

The cogging sequence is also defined by two zones which correspond each to the forging of one half of the ingot, see Figure 26. The zone in between zone one and two corresponds to the manipulation and 180 degree rotation of the ingot. The figure shows this to last around 20 minutes. The time of this operation is greatly increased because of a simultaneous surface crack repair, image of process variability. Standard operation time is less than a few minutes.

A second characteristic trait inherent to the cogging sequence is the similarity between the position curve and a square wave, visible in the zoom of Figure 26. The maxima and minima represent working on part width and height respectively. Therefore the amplitude gives a measure of the part width during forging. During cogging in particular, a variation in part height is observed during passes especially whilst working on the first half. This observation is also notable in the data concerning press position, characterised by the slope or 'steps' formed by the curve. The characterisation of this cogging phenomenon is known as 'staircase forging'. An example is given in Figure 27.
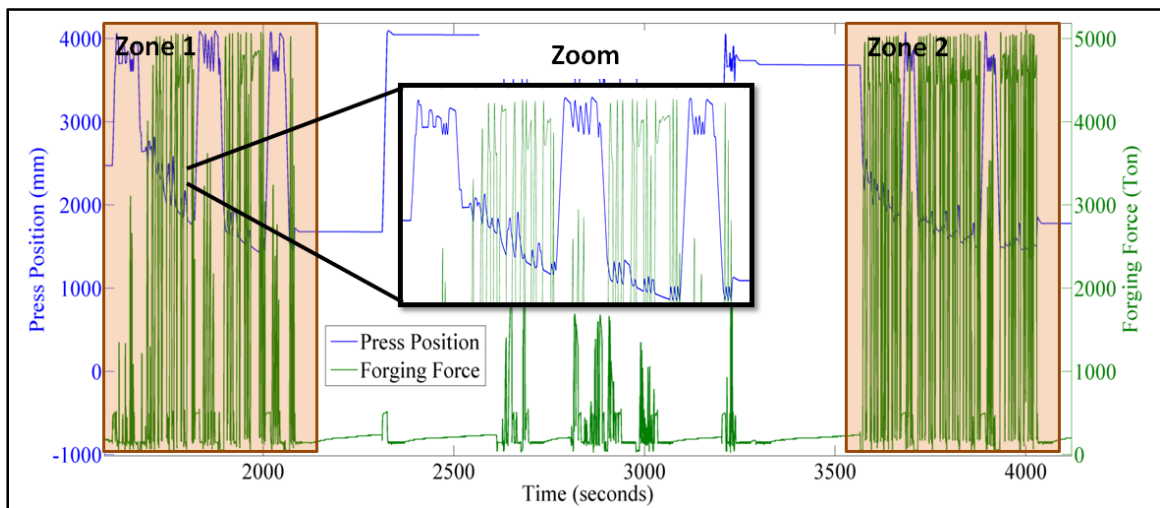
Figure 26 : Cogging characterisation

A staircase is formed between two floors, confirming that part height and not part width is being worked. The data shown in the top part of Figure 27 shows four steps in the staircase, delineated with coloured rectangles. Each step is made up of a combination of deformations from the press on the workpiece, also known as 'hits' or 'blows', and manipulator and workpiece movement. The direction of workpiece movement alternates between steps. The manipulator translates either towards or from the press. The zoom in Figure 27 shows 17 significant maxima corresponding to 17 hits of the press for four steps and consequently three changes in the direction of part movement. The last hit of each step is deeper than the precedent, depicted in the lower part of Figure 27. The incrementation continues until the desired part height is reached. The depth of last hit of the last step matches the previous hit in

order to maintain height homogeneity. The steps of the staircase forging can be seen on the workpiece surface. This defect is eliminated during the second half cogging. In this example average press position after hit for each pass reduces from 1786mm to 1591mm. Average part height after each pass is calculated as [516,415,362,321] mm.
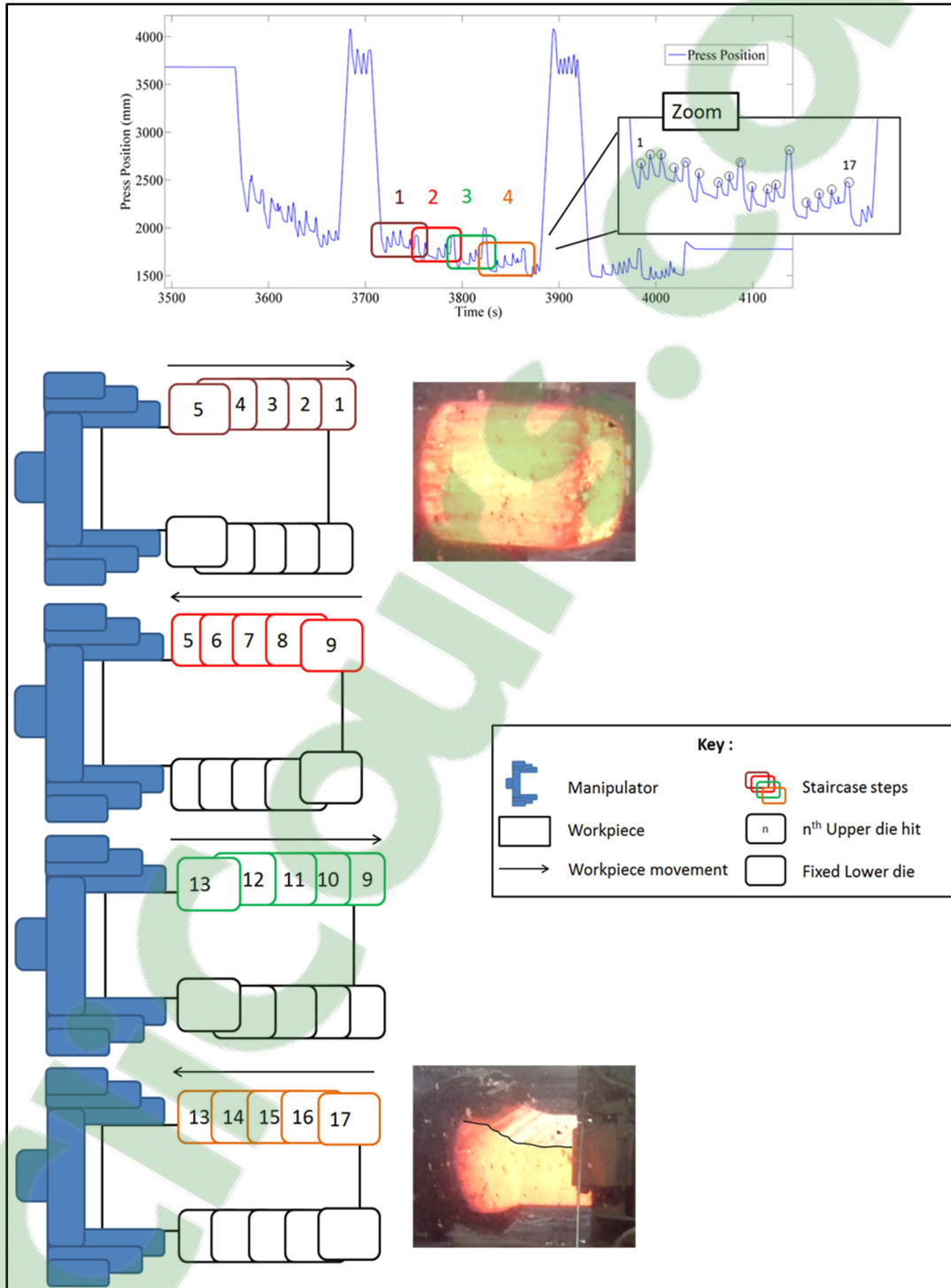
Figure 27 : Example of Staircase Forging

The identification of the finishing sequence is simpler than the previous sequences because it appears in a self-contained file, meaning that it is the only sequence in the file. This is because of temperature re-homogenisation after cogging. The analogy with a square wave is even more apparent during finishing due to minimal variation in part topology, see Figure 28. At the end of the cogging sequence a slab has been formed. During finishing, the slab increases around a meter in length whilst reducing in width (8 inches = 203.2mm) and in height (12 inches = 304.8mm) but keeps its shape during the entire process. The position curves for this sequence are therefore easier to analyse and the results more precise.
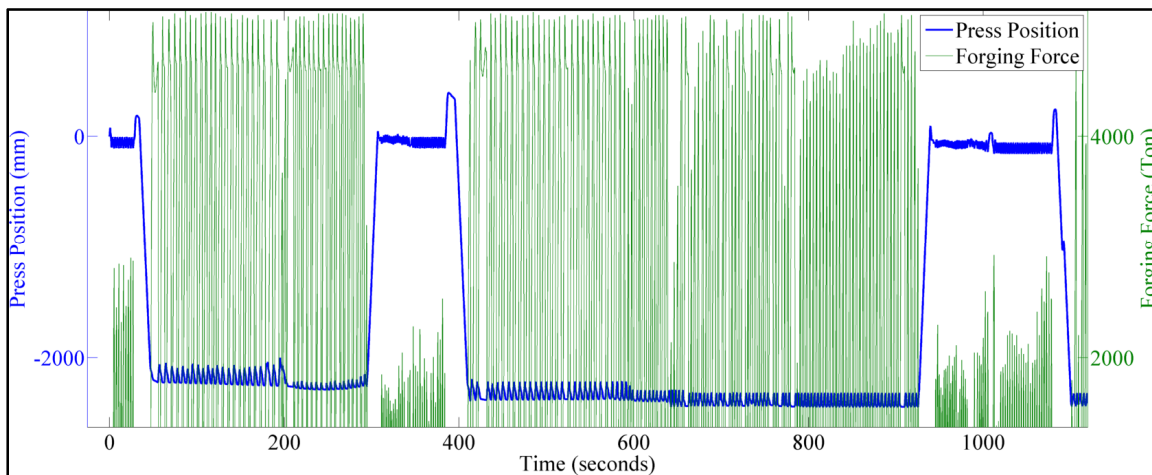
Figure 28 : Finishing characterisation

2.5 Preliminary conclusions

The current forging process can be broken down into four significant sequences; Upsetting, FM process, Cogging and Finishing. Each sequence contains variability and the potential for standardisation based on the indicators defined in Table 4. Video analysis helped identify the different sequences in relation to the data collected from position and force sensors during forging. Initial data analysis shows similarity between upsetting and the FM process. The same is true for cogging and finishing. 'Staircase forging' was shown to be characteristic of the cogging sequence. Similarity was noted between Finishing position curve and a square wave. The indicators in Table 4 were shown to be accessible from the data collected. Large

amounts of data must be analysed in order for results to be meaningful. The following chapters, and in particular CHAPTER 5, use the previous analysis for the development of a new Forge analysis software.

CHAPTER 3

DEVELOPMENT OF A FAST CONVERGING MATERIAL SPECIFIC VOID CLOSURE MODEL DURING INGOT FORGING

After an initial analysis of the forging process, the following work aims to identify and evaluate the applicability of current void closure models to large size ingots, ultimately tailoring the most adequate model for specific materials including P20, that of the industrial partner. The coupled effect of void closure parameters for the newly developed void closure model is studied. Results show the triaxiality state and deformation to be of high influence for successful void closure. Increased values of Norton exponent, material parameters, were shown to influence void closure on a lesser scale. An initial study as to the effectiveness of in billet void positioning is carried out. An in depth analysis is detailed in CHAPTER 4. Initial results show the upsetting process as the most effective sequence for concerning void closure. This Chapter is submitted as an article and is currently under review in Journal of Manufacturing Processes.

DEVELPOMENT OF A FAST CONVERGING MATERIAL SPECIFIC VOID CLOSURE MODEL DURING INGOT FORGING

Nathan Harris[*], Davood Shahriari, Mohammad Jahazi

École de Technologie Supérieure, Département de Génie Mécanique, 1100, rue Notre-Dame Ouest Montréal, Québec, H3C 1K3, Canada
nathan.harris.1@ens.etsmtl.ca

3.1   Abstract

The current paper focuses on the subject of internal voids and the process of hot forging used for their elimination in the manufacturing of large steel billets. A new method is proposed to identify and compare the applicability of six different void closure models to large size ingots. The effects of remote equivalent strain, stress triaxiality state and material parameters are considered in the analysis. The Hansel-Spittel flow stress law is implemented as a foundation for the development of original rational polynomial equations capable of predicting the value of void closure equation material dependant constants. Void closure is simulated for an extended range of materials and specifically applied to a newly developed high strength steel. Coupled parameter effects and material sensitivity are visualised using novel animated 3D mapping. FEM is used to give a quantified evaluation of the effect of void positions during forging. The effectiveness of the upsetting process concerning void closure in central upper billet and core regions are discussed and optimum conditions identified.

Keywords: Void Closure, Ingot Forging, Material Specific, FEM, Optimisation.

3.2   Introduction

Over the last decade Steel forging industries have experienced significant growth leading to larger castings for critical metal components in Aerospace, Transport and Energy production. Large ingots are prone to more defects, including internal voids which, as confirmed by Li et al. (2014), are developed during solidification. These material heterogeneities must be

eliminated in order to improve workpiece microstructure quality. Open die hot forging is the main technique used for the removal of voids during ingot breakdown. However, due to cost and the length of this process, trial and error cannot be used, particularly when it comes to large size ingots. The development of fast calculating mathematical models is therefore necessary. Material properties must be well accounted for to avoid model deficiencies. In addition, the complexity of establishing analytical models has confirmed a need for numerical simulations which nevertheless lack precision in comparison.

Numerous investigations have been dedicated to the understanding and modelling of void closure. Budiansky et al. (1982) introduced expressions for the volumetric strain rate of a spherical void in nonlinear viscous materials for both High and Low Stress Triaxiality states (HST, LST). This model lacked information enabling a continuous transition between the HST and LST. Duva and Hutchinson (1984) later generalised the model using an interpolation approximation, (3.1) .Zhang and Cui (2009) showed Duva and Hutchinson's model constants $\{c_1, c_2\}$, to be function of the materials Norton exponent, considering the strain hardening phenomenon.

$$\frac{\dot{V}}{\dot{E}_e V} = sign(\Sigma_m) \left[\frac{3}{2} \left(\frac{3}{2n} |T_x| + \frac{(n-1)(5n+2)}{5n^2} \right)^n + c_1 |T_x| + c_2 \right] \tag{3.1}$$

The model is based on the fundamental assumption that the void remains spherical during the extreme deformation cycle, which is a strong simplification. The authors agreed that it is probably because of this assumption that the generalised model showed discrepancies for intermediate triaxiality states mainly related to an underestimation of the deformation rate. The importance of stress triaxiality in effective void closure was also underlined by P. M.Dixit (2008). However, a generalisation of the coupled effect of this parameter with other influencing factors is yet to be analysed.

Ragab (2004) proposed a volumetric strain rate function, with optimised numeric constants, based on previous work by Tvergaard (1982). While the model is capable of predicting more adapted void shape evolution it omits the Norton exponent effect and is therefore undistinguishable when applied for different materials. Zhang and Cui (2009) successfully

predicted morphological evolution from initially elliptical voids to penny shape cracks by also taking material effects into consideration. However the model failed to link the ellipse hypothesis to real complex internal cavities observed in large ingots. Saby (2013) justified the use of an ellipse to represent real void morphologies using an equivalent inertia matrix. An analytical volumetric strain rate function was found and numerical results obtained via application of the Rayleigh Ritz (RR) procedure, a method earlier analysed by Zhongxiao and Stewart. (2000). This solidified the theory and implication of void closure for real morphologies in Finite Element (FE) software programs. Therefore, the use of analytical solutions alone, in order for the accuracy of void closure models to progress, has become out-dated.

Data generation with FEM software has led to refined semi-analytical mathematical models. Zhang and Cui (2009) developed an analytical void closure model, with a dependency on the void shape factor λ, allowing for void shape evolution depending on cumulated strain. This model was the basis for an improved semi-analytical model by the same authors with a more accurate interpretation concerning the effect of the macroscopic effective strain. It's implementation into FE software enabled the identification of four inherent material dependant constants $\{q_1, q_2, q_3, q_4\}$ using a cubic cell model containing an initially spherical void Zhang et al. (2009), Equation (3.2).

$$\frac{\dot{V}}{\dot{E}_e V} = sign(\Sigma_m) \left[\frac{3}{2} \left(\frac{3}{2n} |T_x| + \frac{(n-1)(5n+2)}{5n^2} \right)^n + q_1 |T_x| + 3q_2 E_e^2 + 5q_3 E_e^4 + q_4 \right] \qquad (3.2)$$

The void closure model correlated well with experimental results obtained by Lee and Mear (1994), particularly for intermediate triaxiality states used in industrial forging, showing the model's potential for use on large ingots.

Based on the above analysis it is clear that the present models suffer from reliability in relation to material parameters and clarity of representation concerning the interaction between significant void closure parameters making their evaluation for large ingots difficult. The aim of the present work is to generalise the representation of the above void closure models with original evolving surface functions of the materials Norton exponent, applied

remote equivalent strain and triaxiality states. An authentic visualisation is sought out for the qualification and quantification of the effects of these parameters. New constitutive equations for the respective factors $\{c_1, c_2\}$ and $\{q_1, q_2, q_3, q_4\}$ in the mathematical formulation of void closure were developed targeting reduced calculation time and easy application for specific materials. FE modelling was then used to simulate void closure for a large size ingot made of a newly developed high strength steel using the proposed void closure model.

3.3 Mechanical and material conditions

3.3.1 Ingot breakdown process

The ingot breakdown process is a key step in the forging of extra-large cast ingots as it marks a radical microstructural reorganisation. The process is generally composed of two phases. These are Upsetting, the pressing on the end of a heated bar with intent to increase workpiece diameter, and Free form Mannesman effect, FM, forging. Finite element simulations of the former showed increased stress and strain levels leading to greater localised deformation and optimised conditions for void closure Lin et al. (2008). The upsetting process was therefore selected as the current investigation's focal point.

The ingot breakdown for high strength steels occurs during the hot forging process at temperatures around 1260ºC. Tkadlečková et al. (2013) demonstrated that large ingots house a conglomeration of voids mainly along their principal axis and in particular in central locations as shown in Figure 29. They also showed that internal temperature variation depends on the considered location of void within workpiece. Recently, K.Chadha et al. (2015) using finite element simulations verified minimal temperature variation for centreline positions during ingot breakdown of large size ingots. On the basis of the above findings, in the present investigation the study will focus on central locations of the ingot and temperature is considered constant in these regions during the void closure process.
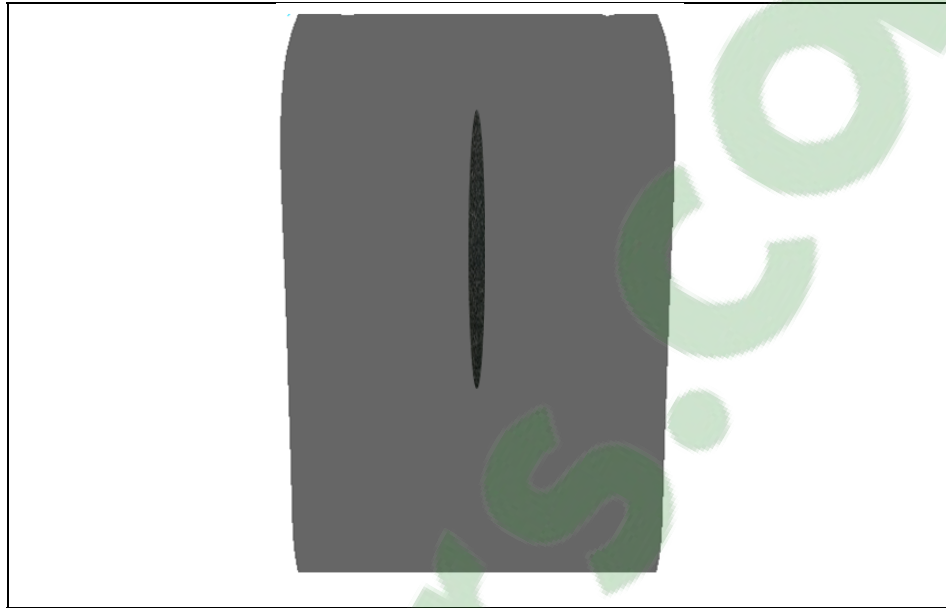
Figure 29 : Schematic view of concentration of shrinkage
voids in a large size ingot.

3.3.2   Stress and material behaviour assumptions

Data on characteristic void dimensions by Saby (2013) were found to range from microns to millimetres. The dimensions of the analysed matrix volume containing void is therefore considered very small compared to the characteristic dimensions of a large ingot which are at least 30 times bigger. In the present investigation a cubic cell was used to model constitutive matrix material. The cell dimensions were evaluated acknowledging the temperature of the investigated material to be homogenous and constant for an instant in time. A maximal edge size of 50mm was calculated from FE simulations.

The Hansel-Spittel (H-S) flow stress function was selected to model material behaviour during hot deformation because of its frequent use in FE codes for bulk metal forming. Specifically, Kakimoto et al. (2010) using the H-S model developed a forging process model for internal void colsure which was later improved by Kim et al. (2011) and applied to large size ingots.   The model predicts a viscoplastic flow stress taking into account material

phenomena such as strain hardening, material softening, material sensitivity to strain and coupled effects with the temperature.

$$\sigma = Ae^{m_1 T} \varepsilon^n \dot{\varepsilon}^m \qquad (3.3)$$

Where A is a corrective model coefficient and m_1 a temperature dependant exponent. The model's material dependant constants are n and m, respectively the Norton and strain rate sensitivity exponents.

The mathematical void closure models represented in a following section of this paper all hypothesize a direct relationship between the Norton exponent, n, whose values were taken from FORGE NxT 1.0® software database, and the strain rate sensitivity exponent m through equation (3.4). Considering process temperatures, error induced by the former hypothesis is shown to be negligible for the considered material study, as discussed by Montheillet and Jonas (1996).

$$n = \frac{1}{m} \qquad (3.4)$$

The assumptions made on cell size and location in the ingot simplify the temperature dependant material parameter used in the material law in equation (3.3) as follows:

$$\sigma = Cte(t)\varepsilon^n \dot{\varepsilon}^m \qquad (3.5)$$

Where $Cte(t)$ is a time dependent constant relative to forging process completion. In the present investigation, the selected temperature, $1260°C$, is that of the ingot core prior to the upsetting process. Strain values were obtained from FE simulations of a large ingot and were found to correlate with ranges also used by other authors Lee et al. (2011). The strain rate value, $1s^{-1}$, was selected from the higher end of the industrial forging bracket with the aim to quantify the effect of a more severe upsetting process on the material's flow stress levels. Both the strain range and strain rate values are representative of the actual industrial process.

A comparison between equation (3.3) and (3.5) can be seen in Figure 30. The two curves display alike trend evolutions. The impacts of the simplification on material flow stress

appear as a slightly less severe strain hardening phenomenon (a 3.4MPa decrease in maximum yield stress). However, material softening effects occurring after the peak stress are identical in both cases, indicating that the simplification does not affect the kinetics of microstructure evolution. A constant relative error of about 6.8% was observed between both models for strains exceeding $\varepsilon = 0.2$ The simplified material model therefore allows application of the void closure expressions formulated above whilst displaying low relative error.
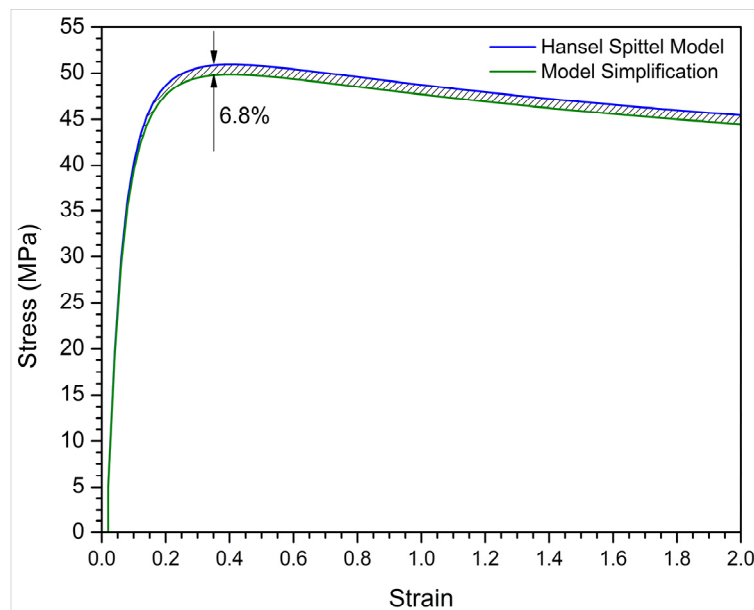
Figure 30 : Stress strain curve for 25CrMo4.

3.4   Determination of material dependant void closure constants

As indicated in equations (3.1) and (3.2) both analytical Duva and Hutchinson (1984) and semi-analytical Zhang et al. (2009) models contain material dependant factors $\{c_1, c_2\}$ and $\{q_1, q_2, q_3, q_4\}$ influencing the volumetric strain rate. To date no exact analytical solution has been provided for the above equations and therefore other mathematical procedures must be used. The RR method was employed in the two previous papers for the determination of the constants $\{c_1, c_2, q_1, q_2, q_3, q_4\}$. In the present investigation the RR method was also used to determine the numerical values of the constants as shown in Table 5 and Table 6. Using these

values, the influence of the material parameters, stress triaxiality and deformation can now be analysed.

The influence of parameters c_1, c_2 on the volumetric strain rate function was evaluated for compressive triaxiality states ranging from -1 to 0, Figure 31. For a highly compressive triaxiality state, $T_x \geq 0.9$, the second member, $\left[c_1 |T_x| + c_2 \right]$ is principally positive. The effect of this term on equation (3.1) is thus accentuated making the void closure function more deformation dependent. However, as reported by Saby (2013) the triaxiality state during forging reaches $|T_x| \leq 0.8$, and the Norton exponent values range from $n \in [1, 20]$, FORGE NxT 1.0 ®). Therefore, $\left[c_1 |T_x| + c_2 \right]$ cannot be considered as constant nor positive. As a result, the material parameters c_1, c_2 are shown to reduce the influence of deformation in Duva and Hutchinson's void closure model for industrial hot forging.
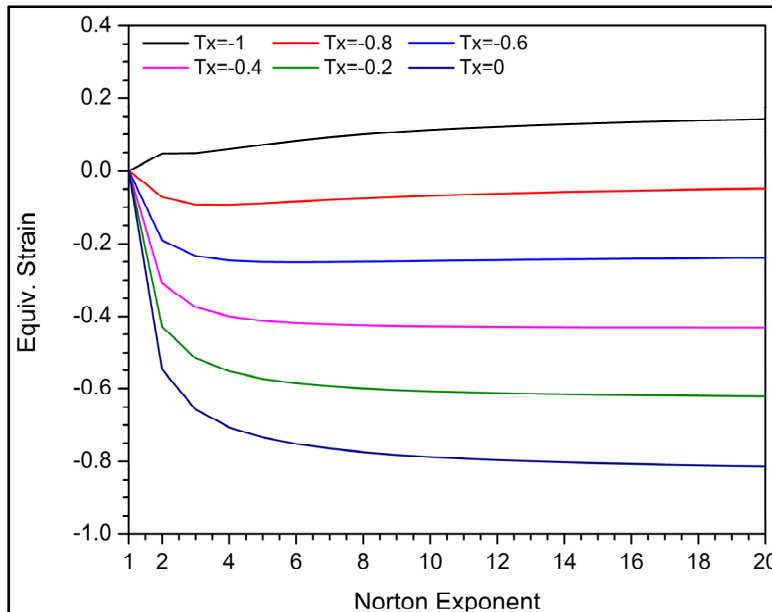
Figure 31 : Influence of c_1, c_2 on volumetric strain rate.

The influence of combined material parameters, $[q_1 |T_x| + 3q_2 E_e^2 + 5q_3 E_e^4 + q_4]$, on void closure for different volumetric strain, E_e, and triaxiality, T_x, values was analysed and the

results are illustrated in Figure 32 and Figure 33. The value of $[q_1|T_x|+3q_2E_e^2+5q_3E_e^4+q_4]$ is shown to vary for $n \in [1,20]$ before reaching an asymptote for $n>25$. The triaxiality state greatly influences the impact of the constants $\{q_1,q_2,q_3,q_4\}$ for small accumulated deformation, $E_e \leq 0.2$. As shown in Figure 32, the negative slope of the curves is less apparent for greater absolute triaxiality showing that the influence of $\{q_1,q_2,q_3,q_4\}$ on void closure is not monotonic at the beginning of the upsetting process.

In the case of greater macroscopic strain, $E_e \geq 0.4$, as shown in Figure 33, the variation of $[q_1|T_x|+3q_2E_e^2+5q_3E_e^4+q_4]$ is monotonic and quasi-linear for $n \in [1,20]$. This shows a direct relationship between the material's Norton exponent and the material constants $\{q_1,q_2,q_3,q_4\}$. Analysis of Figure 33 indicates that, the influence on void closure grows for increasing Norton exponents and for greater absolute triaxiality states. Further evaluation was carried out for $E_e \geq 0.4$ and an asymptote was obtained, reaching a maximum of 1600 for $E_e =1$. It is also important to note that, as shown in Figure 32 et Figure 33, the influence of triaxiality decreases as more deformation is applied. The parameters $\{q_1,q_2,q_3,q_4\}$ are therefore seen to become more influent for void closure as E_e increases throughout the forging process.

Figure 32 : Influence of $\{q_1, q_2, q_3, q_4\}$ on volumetric strain rate, $E_e = 0.2$.

Figure 33 : Influence of $\{q_1, q_2, q_3, q_4\}$ on volumetric strain rate,

$E_e = 0.4$.

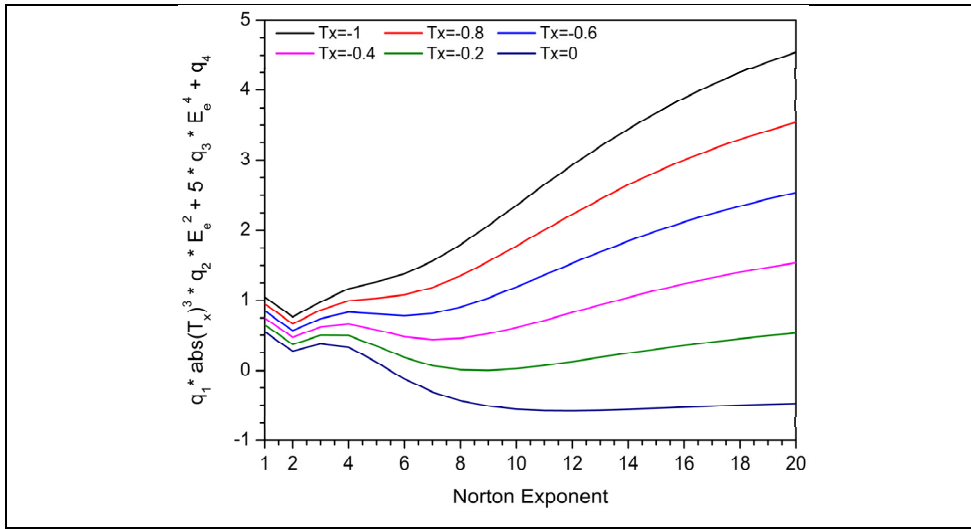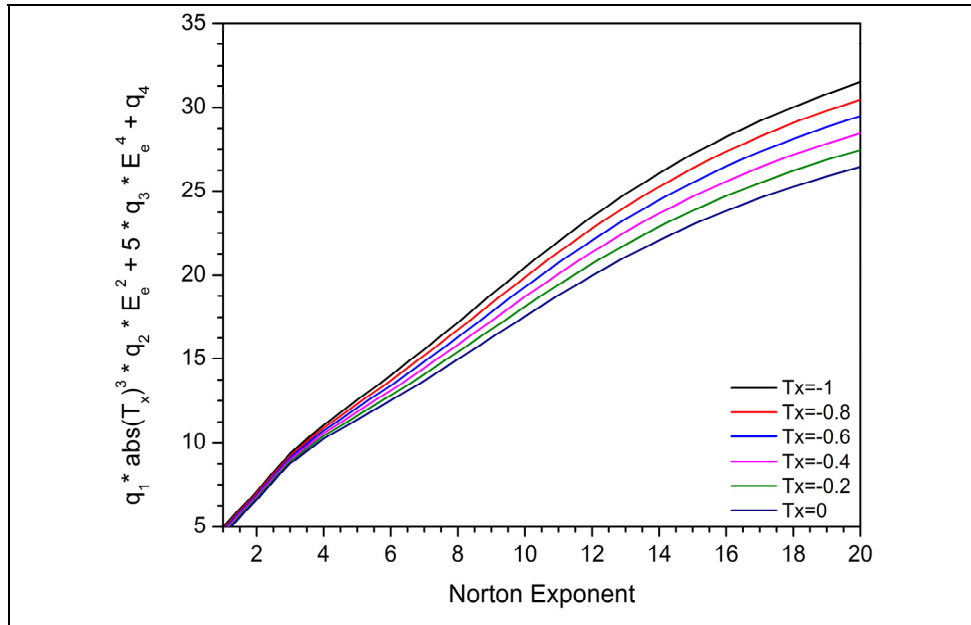## 3.4.1   Development of material dependant model constant functions

As discussed the RR formalism has been used to determine material dependant void closure model constants. However, the RR method is computationally costly, prolonging the

application of equations (3.1) and (3.2) for different materials. In the present investigation a novel method, quicker and less demanding in terms of calculation, is proposed for the determination of the material constants.

As shown in Figure 34, the form of the initial plotted data for $\{c_1, c_2\}$ (Table 5) against variations of n values has hyperbolic trends with two inverse tendencies and non-exact symmetry. Similar observations can be made for $\{q_1, q_2, q_3, q_4\}$ (Table 6), shown in Figure 35 to Figure 37, using varying degrees of the Norton exponent as the plotting variable. The verification of the curve identification algorithm results was approved (Table 7) averaging two different statistical indexes, R^2 and adjusted R^2. All the data presented in Table 5 and Table 6 best fit a rational function described in equation (3.6) with function f representing each of the six model constants, $\{c_1, c_2, q_1, q_2, q_3, q_4\}$.

MATLAB 2013 was used to define the proposed material dependent constant functions.

$$f_i(x) = \frac{p_i(x)}{r_i(x)} \text{ with } i \in [1,6] \tag{3.6}$$

The numerator and denominator respectively, $p_i(x)$ and $r_i(x)$, both fit polynomial functions of the third degree with x a varying degree of an inverse power function of n. Their expressions are as follows:

$$p_i(x) = \sum_{k=1}^{4} p_k x^{k-1} \text{ and } r_i(x) = \sum_{k=1}^{4} r_k x^{k-1} \tag{3.7}$$

$$\text{with } x = \frac{1}{n^j} \text{ for } j \in [-1,3] \tag{3.8}$$

The model constant varying value of x is obtained by applying the given values of j in Table 8 to Equation (3.8). The developed form of the established functions is denoted in Equation (3.9).

$$f_i(x) = \frac{p_{i4}x^3 + p_{i3}x^2 + p_{i2}x + p_{i1}}{r_{i4}x^3 + r_{i3}x^2 + r_{i2}x + r_{i1}} \tag{3.9}$$

Individual coefficient values, p_i, r_i, for each material model constant and respective relative errors are shown in Table 7, Table 9 and Table 10.

All constants, discounting q_3, showed a maximum relative error lower than 1% over all confirmed data points in comparison with the R R procedure. Results were deemed satisfying with maximal relative error calculated at 1.68% in all simulations for a varying Norton exponent covering high strength steels, $n \in [1,15]$. The above proposed methodology introduces quicker computation times than the traditional RR procedure on top of a simple pre-programmability. The new model, based on Hutchinson's and Zhang's models, is able to calculate material specific void closure providing that either the materials Norton exponent or strain rate sensitivity is known. Equation (3.4) is used with equation (3.8) and the resulting values with equation (3.9). This procedure is repeated in order to obtain all coefficients $\{c_1, c_2\}$ or $\{q_1, q_2, q_3, q_4\}$, and applied to equation (3.1) or (3.2) respectively.

Table 5 : Raleigh Ritz calculated values for c_1, c_2

n	1	2	3	5	10	100
c_1	0	0.5951	0.7061	0.8049	0.9002	1.0066
c_2	0	-0.5479	-0.6571	-0.7340	-0.7874	-0.8329

Table 6 : Raleigh Ritz calculated values for q_1, q_2, q_3, q_4

n	1	2	3	5	10	100
q_1	0.5048	0.4911	0.6016	1.1481	2.9132	6.5456
q_2	6.4675	0.8002	-0.6981	-4.2026	-11.6464	-15.3775
q_3	14.261	53.8018	72.6397	108.2114	185.5622	324.4417
q_4	-0.3379	-0.2314	-0.1243	-0.248	-0.6511	-1.9575

Table 7 : Relative error and statistical data verification index values

Model Constant	Maximum Relative Error	Statistical Verification Indexes	
		R^2	Adjusted R^2
c_1	0.173%	1	1
c_2	0.015%	1	1
q_1	0.025%	1	NaN
q_2	0.013%	NaN	NaN
q_3	1.687%	1	0.9998
q_4	0.872%	1	NaN

Table 8 : Value of j in equation (3.8) for calculated coefficients

Model Constant	Value of j
c_1	-1
c_2	-1
q_1	2
q_2	3
q_3	2
q_4	-1

Table 9 : Numerator coefficient values used in equation (3.9)

Model Constant	Coefficients			
	p_1	p_2	p_3	p_4
c_1	-0.7606	-0.2601	1.021	0
c_2	-0.1901	1.028	-0.8378	0
q_1	0.0629	0.1761	2.392	0
q_2	-0.0011	-0.0421	0.6915	6
q_3	1.047	22.3	0	0
q_4	-7.915	3.933	-0.4851	-0.0139

Table 10 : Denominator coefficient values used in equation (3.9)

Model Constant	Coefficients			
	r_1	r_2	r_3	r_4
c_1	-1.554	1.131	1	0
c_2	-0.009498	-0.6396	1	0
q_1	0.009496	1.251	2.952	1
q_2	7.36E-05	2.68E-02	1	0
q_3	0.003199	0.3607	0.3607	1
q_4	19.45	-7.184	1	0

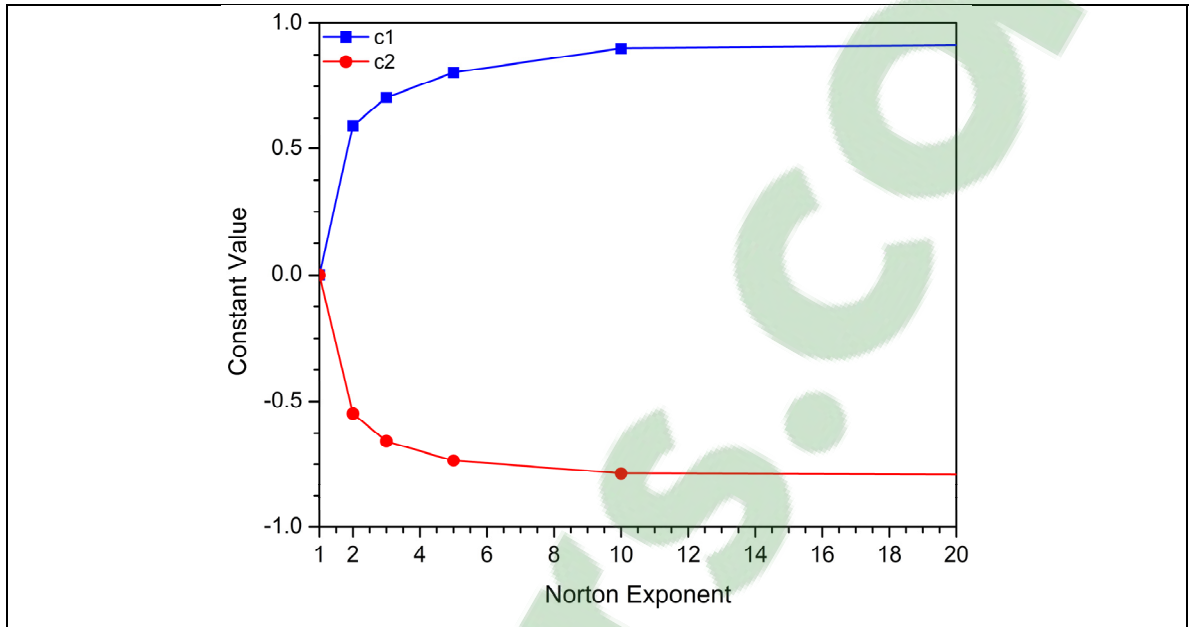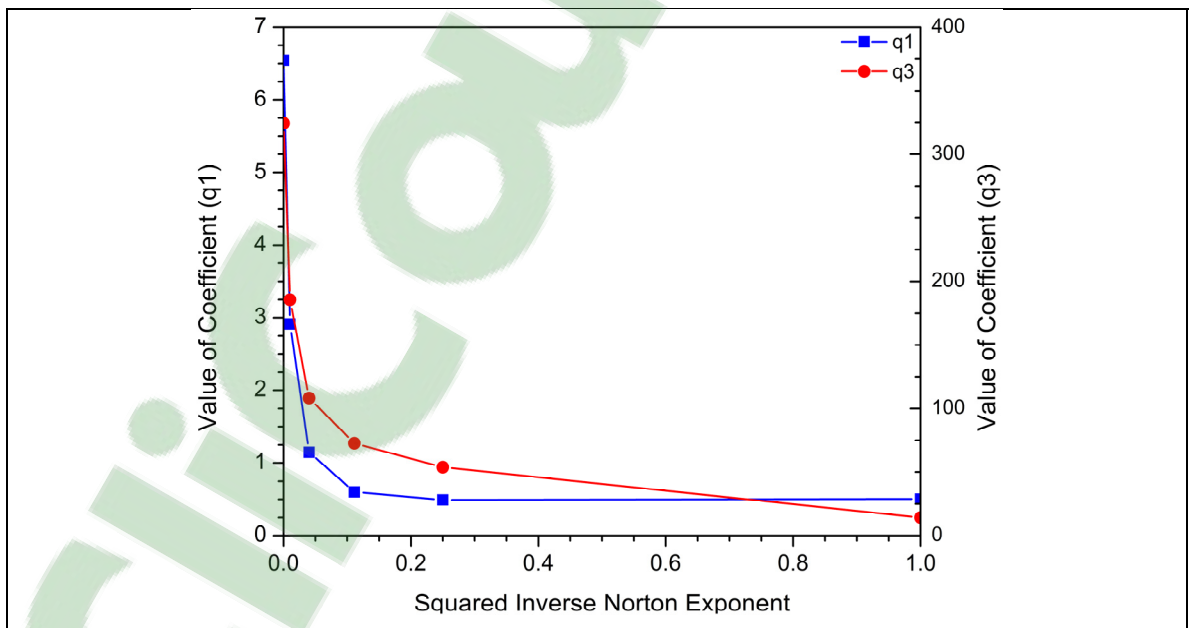Figure 34: The evolution of constants $\{c_1, c_2\}$ in equation (3.1) with the Norton exponent.

Figure 35 : The evolution of constants $\{q_1, q_3\}$ in equation (3.2) with squared inverse of the Norton exponent.
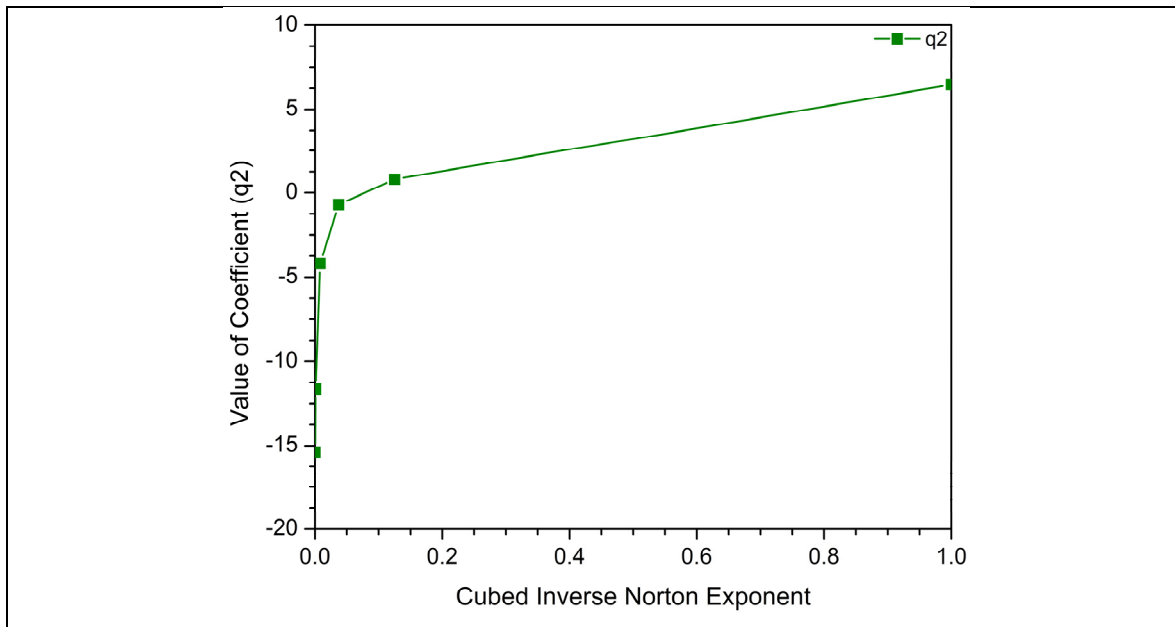
Figure 36: The evolution of constant q_2 in equation (3.2) with cubed inverse of the
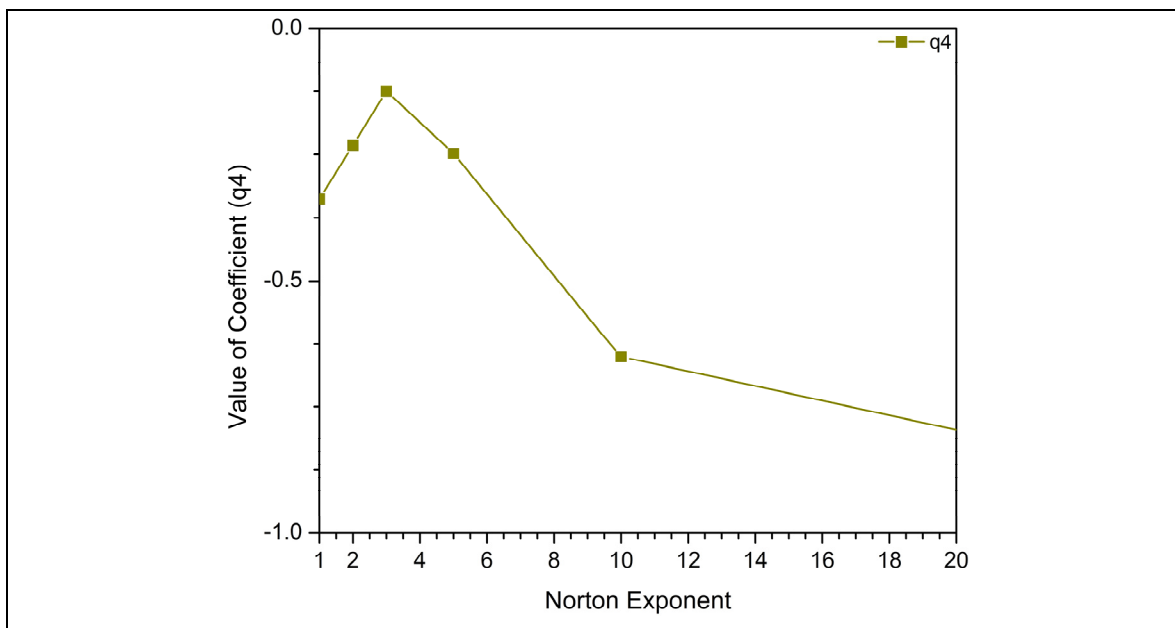
Norton exponent.

Figure 37: The evolution of constant q_4 in equation (3.2) with the Norton exponent.

3.5 Results and discussion

3.5.1 Evolution of void closure

The multifaceted effects of the triaxiality state, strain hardening coefficient and remote equivalent strain on void closure was investigated using animated 3D representation. A 4D matrix was generated to stock data on void closure for the discussed mathematical models. Norton exponents from 1 to 15 were considered in the model in order to widen the simulation's field of application to account for plastic perfectly rigid materials $(m \rightarrow 0)$ and linear viscous Newtonian solids $(n = m = 1)$. Forge Nxt $1.0^{®}$ Database extreme Norton exponent values of $n = 3.71$ (brass) and $n = 13.3$ for an Al-Cu-Mg alloy both non-linear viscous Newtonian solids $(0 < m < 1)$ were selected. Extreme values were sought out to widen the range of studied materials, increasing the spectrum of comparisons. Steels, superalloys and titanium alloys were also investigated and found to lie inside this bracket.

Triaxiality states were selected from industrial hot forging ranges, $Tx \in [-1, 0]$, (Saby 2013). Three values of the stress triaxiality parameter were chosen to represent the selected scope at equal intervals. Optimal visual representation was considered for industrial values of known remote equivalent strain and Norton exponents ranging respectively from $E_e \in [0, 1]$ and $n \in [1, 10]$, high strength steels averaging a Norton exponent of around 7. Results are regrouped in Table 11, showing a comparison of four out of the six different void closure models previously studied. These models were visualised because of their showing material dependency. The two remaining void closure models, conjecturing material independence, were not deemed beneficial to the discussions development concerning 3D visualisation. The vertical axis illustrates relative void closure, the value of 1 indicating a fully open void, the value of 0 indicating successful void closure.

Table 11 : 3D mapping for material dependant void closure models
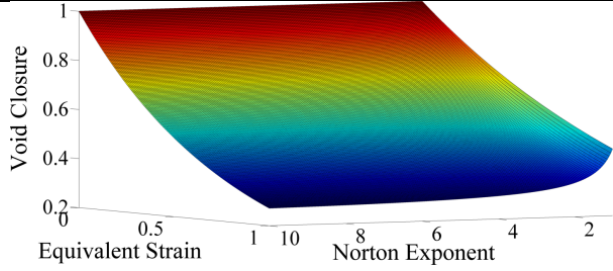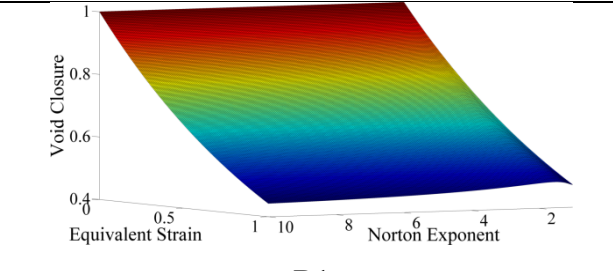
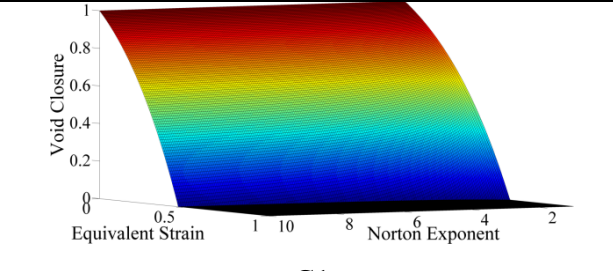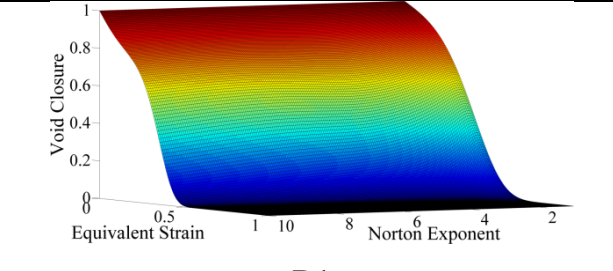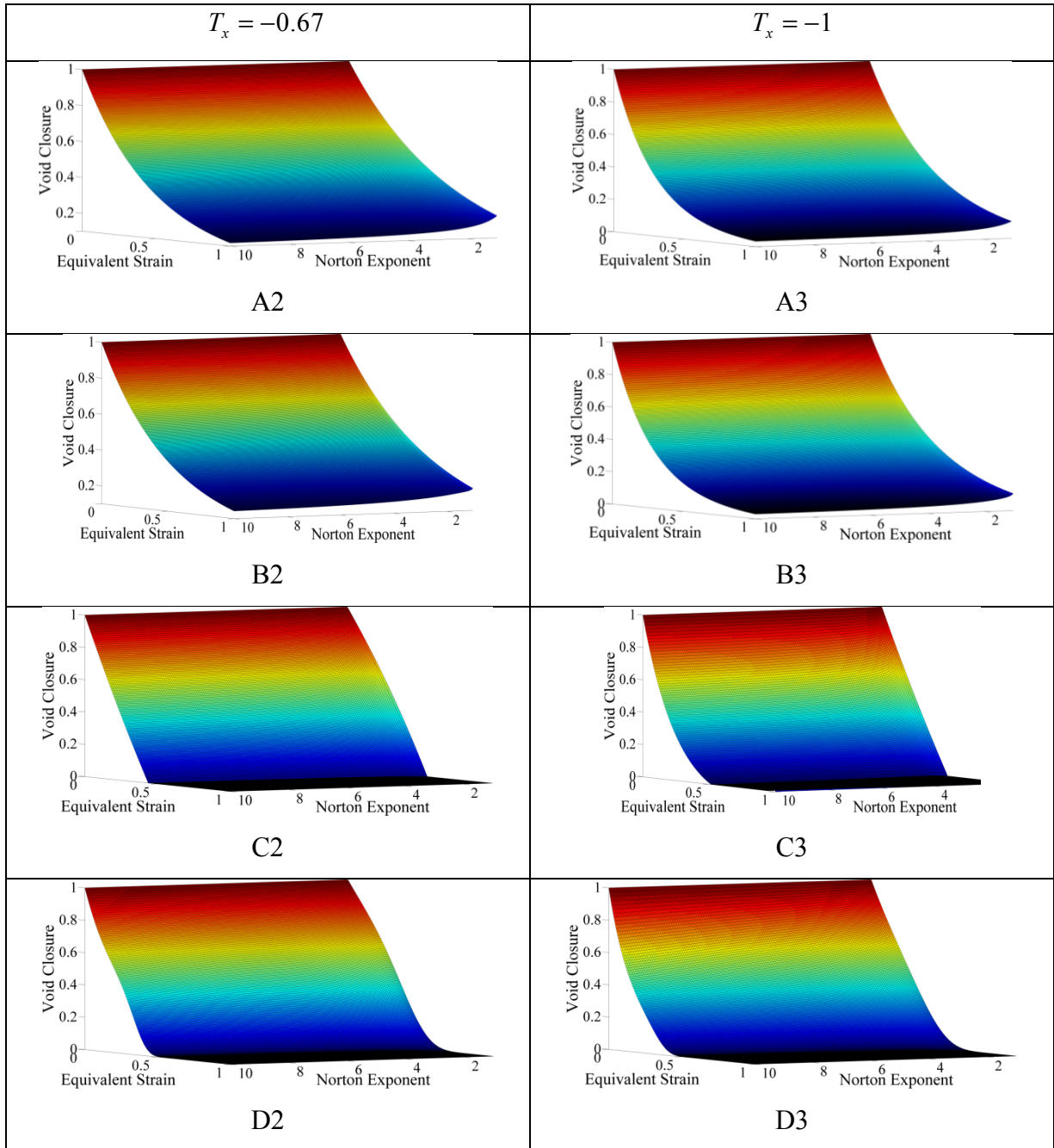|	$T_x = -0.33$
Budiansky model	 A1
Duva & Hutchinson model	 B1
Zhang analytical model	 C1
Zhang semi-analytical model	 D1

Table 11 : (Continuation)

$T_x = -0.67$	$T_x = -1$
A2	A3
B2	B3
C2	C3
D2	D3

Void closure model comparison

Mathematical model applicability for hot forging was evaluated by comparing previously discussed void closure functions. Figure 38 and Figure 39 both show a superposition of sections from maps $\{A1, B1, C1, D1\}$ $(T_x = -0.33)$ and $\{A3, B3, C3, D3\}$ $(T_x = -1)$ from Table 11 for $n = 7.25$, applied to high strength steel 14NiCrMo13.

Analysis of these figures reveals that the STB model is the simplest affine function capable of correctly modelling void closure for initial stages of hot forging only FORGE NxT 1.0 ®) software void closure predictions, based on the STB model, are in accordance with the more complicated models for an equivalent strain ranging from 0.15 to 0.3 and a triaxiality state between -0.2 and -0.5. The preprograming of this model in Forge NxT $1.0^{®}$ software is therefore justified when considering that in large ingots, stress triaxiality states range from $T_x \in [-1, 0]$ with strain levels consequentially bounded by 0.1 and 0.8.

However, the validity of the STB model is observed to decrease as $|T_x|$ increases. The tendency is inversed with void closure models by Budiansky et al. (1982) , Duva and Hutchinson (1984) and Ragab (2004) showing more accurate predictions for high compressive absolute stress triaxiality states superior to 0.6. The models were observed to under evaluate void shape deformation inferior to this threshold. Both of the Zhang models displayed an exponential decay of void closure with increased equivalent strain and correlating results for all triaxiality states.
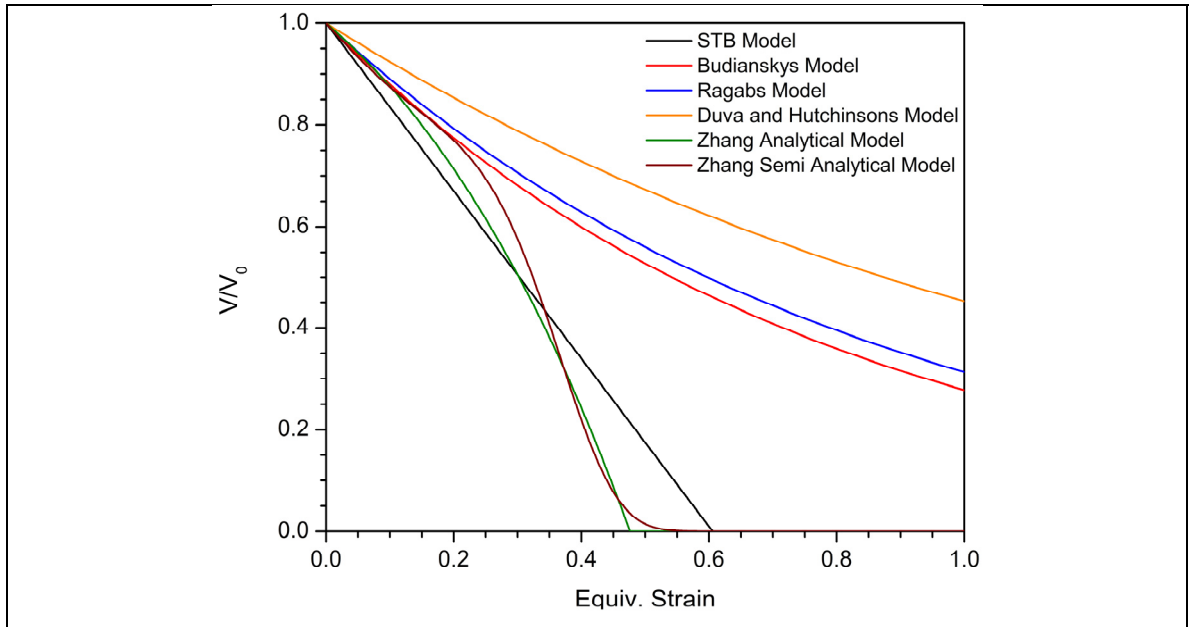
Figure 38 : Void closure comparison for 14NiCrMo13, $T_x = -0.33$.
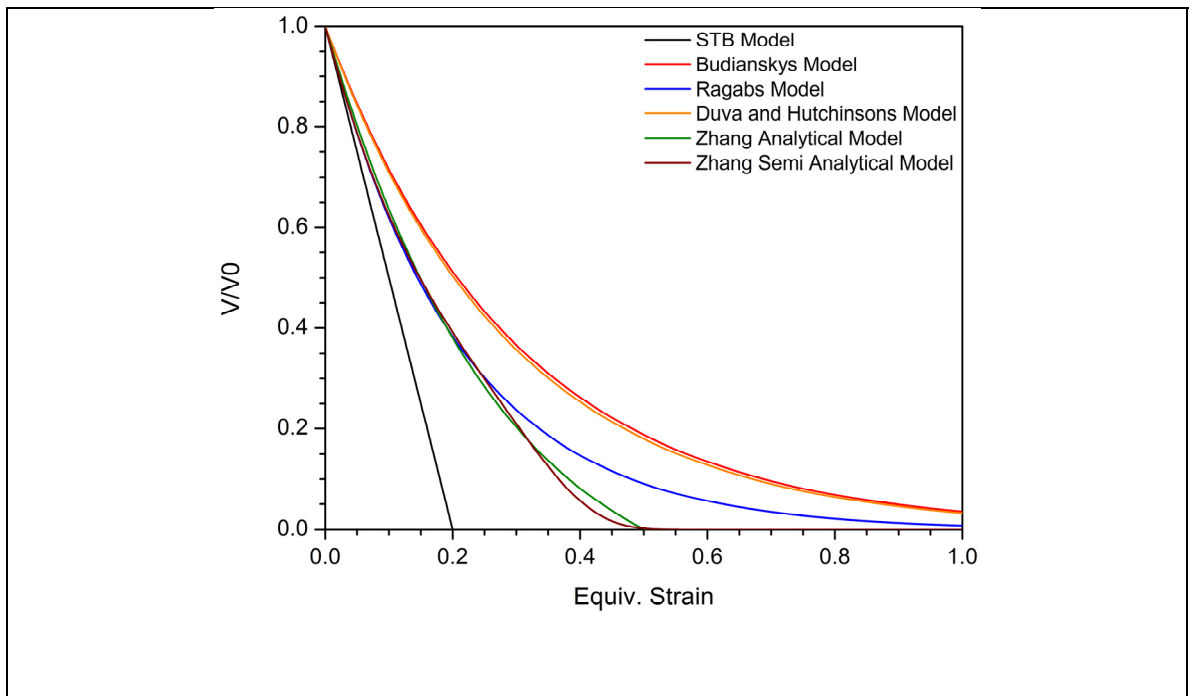

Figure 39 : Void closure comparison for 14NiCrMo13, $T_x = -1$.

3.5.2 Influence of the triaxiality state

The triaxiality state spectrum was discretised in order to successfully integrate the volumetric strain rate equations (3.6) and (3.7). A constant triaxiality state was therefore considered at each point of integration. The integration step was minimized to emulate a more continuous output for void closure illustration. Consequently, animation was added to the 3D representation to include for the void models third integration variable. Considering the compressive nature of the open die forging process, triaxiality values cannot exceed zero nor be smaller than -1, positive triaxiality values signifying tensile stresses. Absolute values of triaxiality superior to 1 do exist and could later be investigated for application in ductile damage studies. Nevertheless, the current investigation focuses on understanding void closure during hot forging and therefore only negative triaxiality values above -1 were considered.

All models showed a more compressive triaxiality state to be beneficial for void closure. Figure 40 shows the influence of different triaxiality states on void closure for $n = 7.25$, corresponding to the high strength steel, 14NiCrMo13. The curves for $T_x = \{-0.33, -0.66, -1\}$ are respective sections of maps $\{D1, D2, D3\}$ in Table 11. For Zhang's semi-analytical model a difference of 26% is observed in the closure of voids from a semi-compressive, $T_x = -0.5$, to a fully compressive material state, $T_x = -1$ for an equivalent strain of 0.3. For the same equivalent strain at a semi-compressive state, Hutchinson's model shows 21% less closure. This finding proves that triaxiality is a significant factor for void closure and that relative void closure variation is similar between models for triaxiality states ranging between -0.5 and -1.
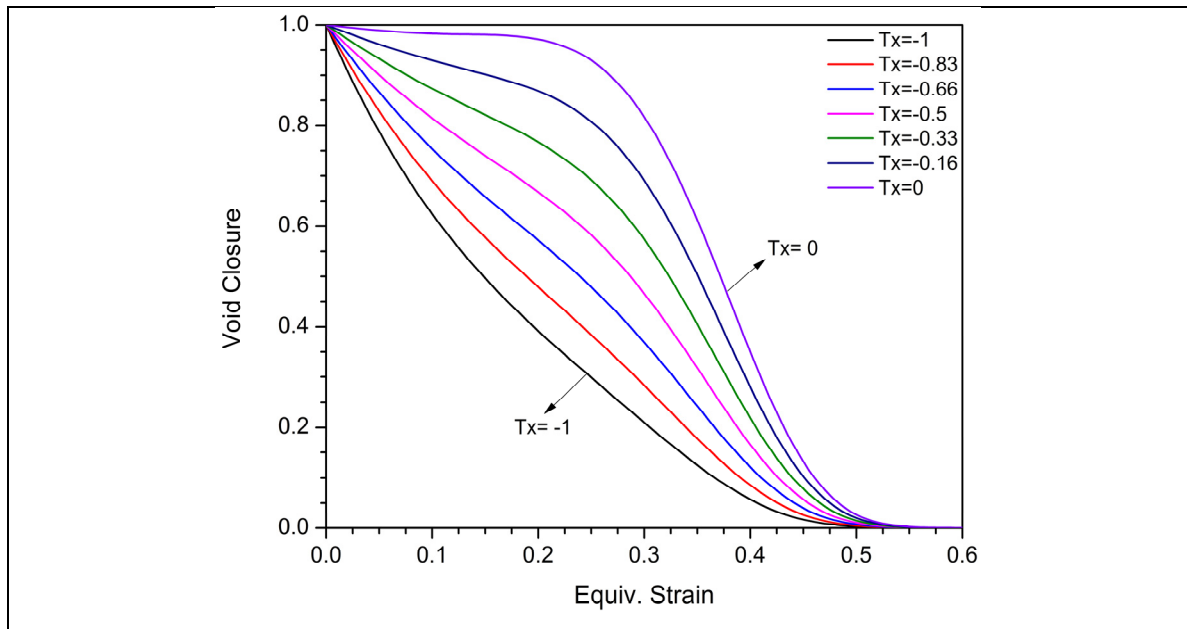
Figure 40 : Influence of triaxiality state for 14NiCrMo13, n=7.25.

3.5.3   Influence of material parameters

The effect of material parameters were also shown to benefit void closure, particularly for higher absolute values of triaxiality state. Significant improvement in void closure becomes apparent for $|T_x| \geq 1$. Rigid perfectly plastic materials showed equivalent closure for a lesser strain. Figure 41 illustrates the influence of the Norton exponent on void closure. The figure was obtained by the superposition of 9 sections from map $D3$ $(T_x = -1)$ for a highly compressed material. Void closure conditions for hot forged steels are compared. Bracket values were $n = 6.54$ for 100Cr6 and $n = 10.09$ for 316L. Data was acquired from Forge NxT $1.0^{\circledR}$ software.

As shown in Figure 41 using Zhang's semi analytical model, for a constant triaxiality state, as the Norton exponent increases lower equivalent strains are required to achieve void closure. The finding can be generalised for all four material dependant models. The limit of convergence illustrates that regardless of the material's ability to work harden during forging, void closure remains only partially influenced. This also indicates the necessity of a triaxiality state coupling for improved void closure.

In the light of the above analysis, it can be said that equation (3.2) proposed by Zhang and Cui on the basis of their semi analytical model is the most accurate for analysing void closure during the ingot breakdown process of the large size ingot high strength steel, P20, from Sorel Forge (Finkl Steel) used in the present investigation.
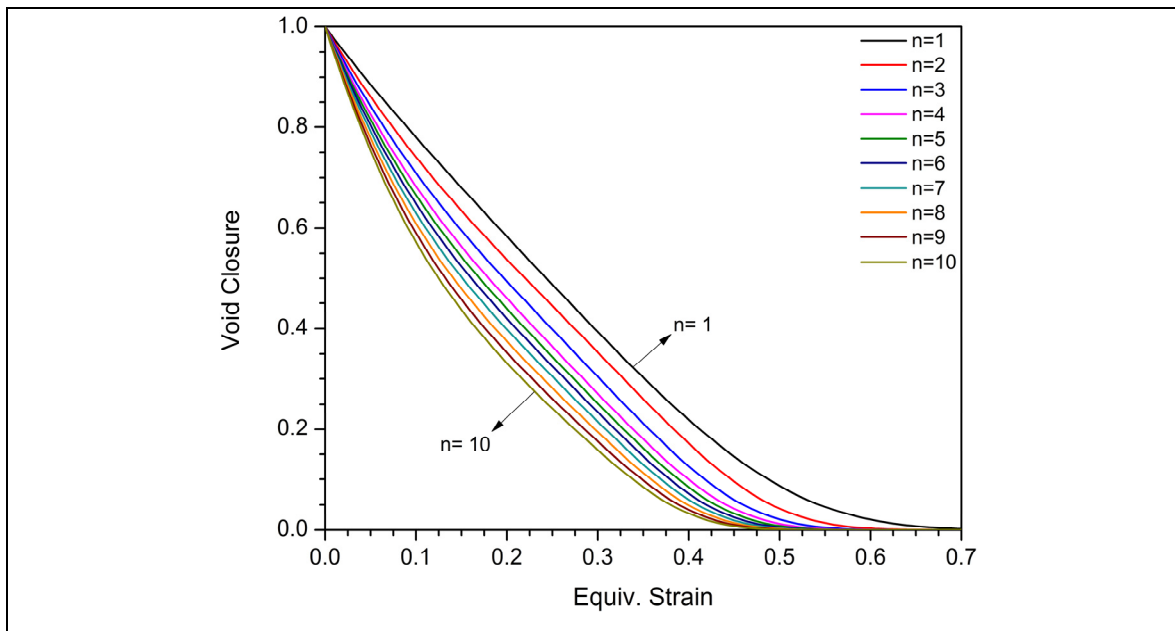
Figure 41 : Influence of Norton exponent on void closure for Tx=-1.

3.5.4   Characteristics of the investigated alloy

P20's chemical composition, similar to that of well-known hot forged steel 42CrMo, is described in Table 12. The 40 tons P20 cast ingot possesses an inhomogeneous dendritic microstructure prone to macrosegregation and cavity development, making it a fitting choice for the intended application. A Hansel-Spittel flow stress law previously developed using the Gleeble 3800 thermomechanical simulator, K.Chadha et al. (2015), was incorporated into the current investigation in order to evaluate the models applicability concerning void closure. The material's Hansel-Spittel parameters were applied in simulation for conditions identical to those described above for mechanical and material considerations. The selected temperature was $1260°C$. The value of the P20's Norton exponent was evaluated at $n = 8.2$. Figure 42 shows the results obtained from FE simulations. As it can be seen a very good

agreement is observed between the Hansel-Spittel and the simplified material model introduced in equation (3.5). The difference is below 4%, confirming the validity of the simplified material model used in the proposed model.

Table 12 : P20 chemical composition (%wt)

C	Mn	Si	Ni	Cr	Mo	Cu
0.37	0.84	0.39	0.25	1.87	0.46	0.16

3.5.5   Material sensitivity

Material sensitivity was evaluated for adapted void closure models. Material dependant function constants defined previously were applied for an extended range of metals, including high strength steel P20, and for several triaxiality states. Figure 43, a superposition of sections from surface map D_1, shows the applicability of Zhang's adapted void closure model to these steels.

An Al-Cu-Mg alloy and brass were considered as boundary materials with extreme n values. Aluminium was identified as the most suitable metal for efficient void closure, showing advanced states of closure with regards to other studied materials for an equivalent strain. Maximum differences were found for intermediate strain values between 0.2 and 0.35 independent of triaxiality states. High strength steels, titanium alloys and superalloys were revealed to display comparable void closure for triaxiality states ranging from -0.33 to -1. A maximum variation of 3.7% was calculated between the investigated alloy, P20, and Ti6AlV4 titanium alloy, proving similar states of void closure possible for materials with significantly different chemical compositions. Brass was shown the most inefficient for void closure as a consequence of a subdued strain hardening phenomenon.
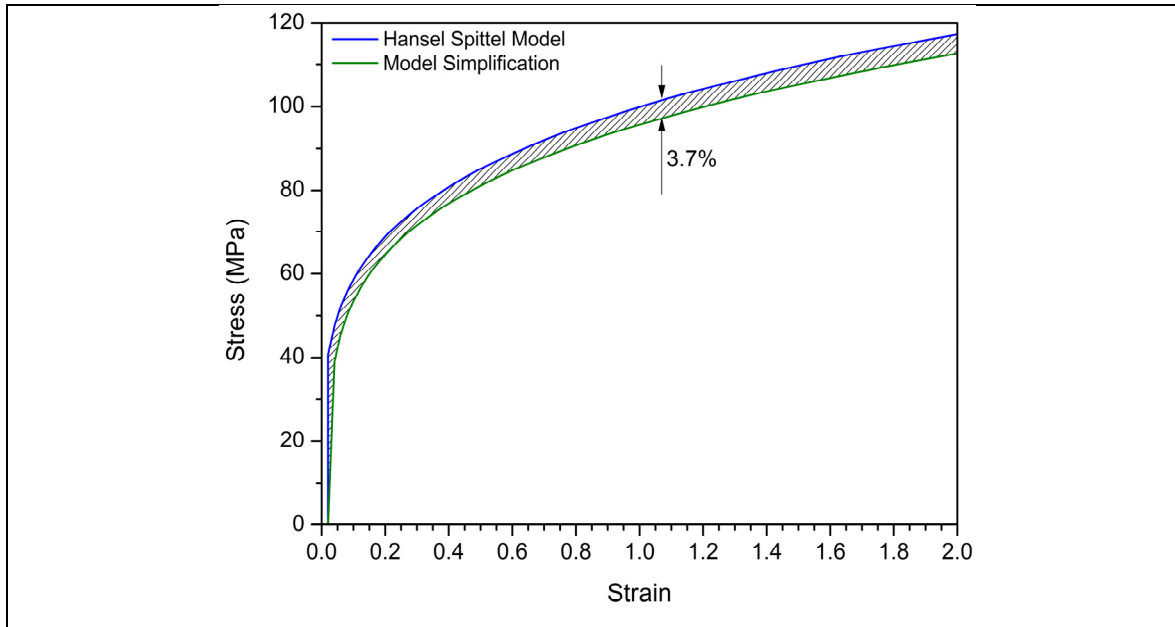
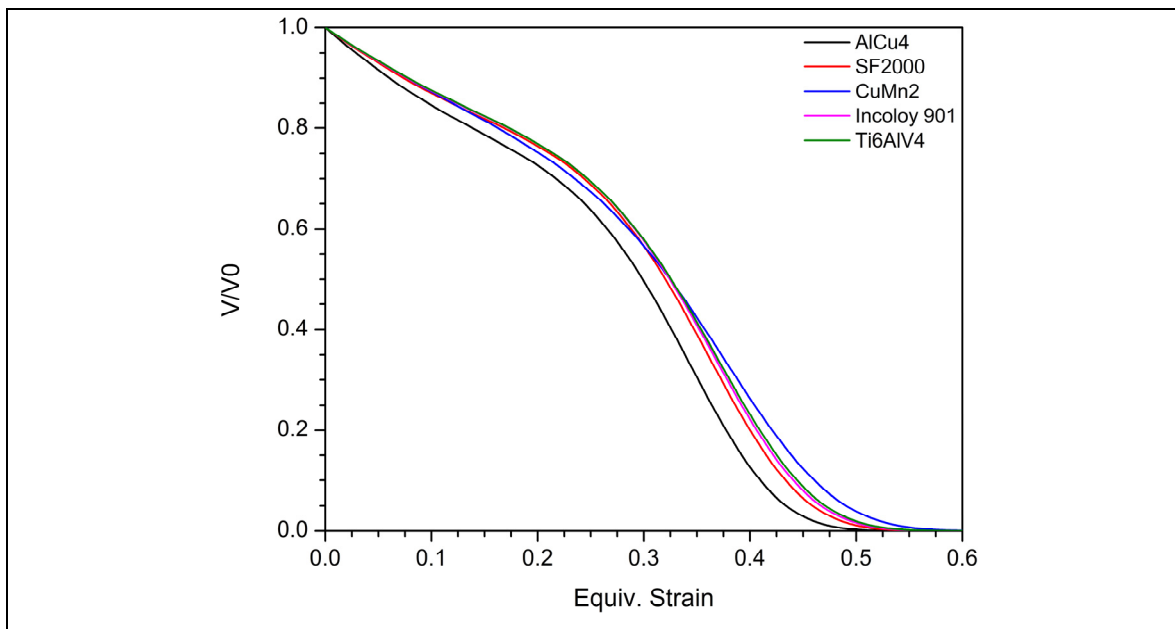Figure 42 : Flow stress comparison between model and simplification.

Figure 43 : Material sensitive void closure, $T_x = -0.33$.

3.6 Model validation for large size ingots based on experimental observations

FE simulations of the upsetting process for large size ingots were run using Forge NxT 1.0 ® software. Void closure was evaluated along a vertical, horizontal, and a 45 degree inclined axis in billet using Zhang's adapted semi-analytical mathematical model during the upsetting process. Model geometry and thermo-mechanical boundary conditions were obtained for the investigated alloy.

3.6.1 FEM simulation setup

Ingot geometry was modelled using CATIA V5® 3D modelling software. Initial hot forging phases such as casting and the pre-form were reproduced in order to replicate exact ingot geometry before the upsetting process. The model measures 2225mm high by 1471mm in diameter. The complex form is doted with a central axial symmetry. Upper and lower die geometries were both modelled by identical cuboids. Importance was placed on the planar nature of contact between the upper die and the ingot top.

Homogenous 3D volume meshing was used to mesh ingot geometry. 25mm sided tetrahedrons were selected as optimal meshing components based on meshing time and ability to successfully reproduce ingot geometry. Both die meshes were selected to be coarse as post computation information were only needed for the billet part. Figure 44 shows the meshing strategy applied to the simulation model.

An initial temperature of 1260 degrees was implemented. Thermal exchange was considered with the surrounding heated ambient air and with the press die, see Figure 45. Industrial practice sees the ingot exterior hosed down regularly with a pressurised air-water mix to help crust metal flake and homogenise the forging effects. This heat exchange was considered negligible.
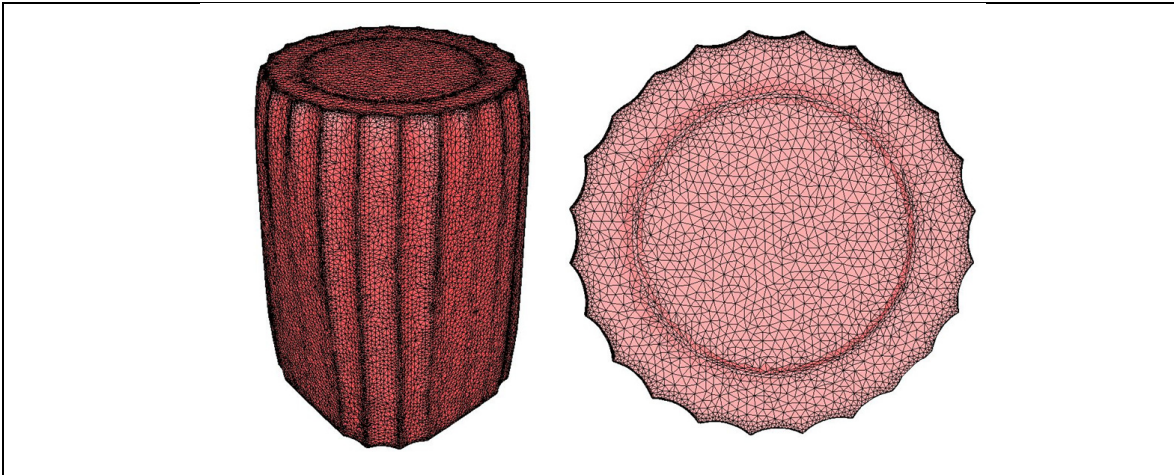
Figure 44 : Ingot geometry and meshing, mesh size 25mm**.**
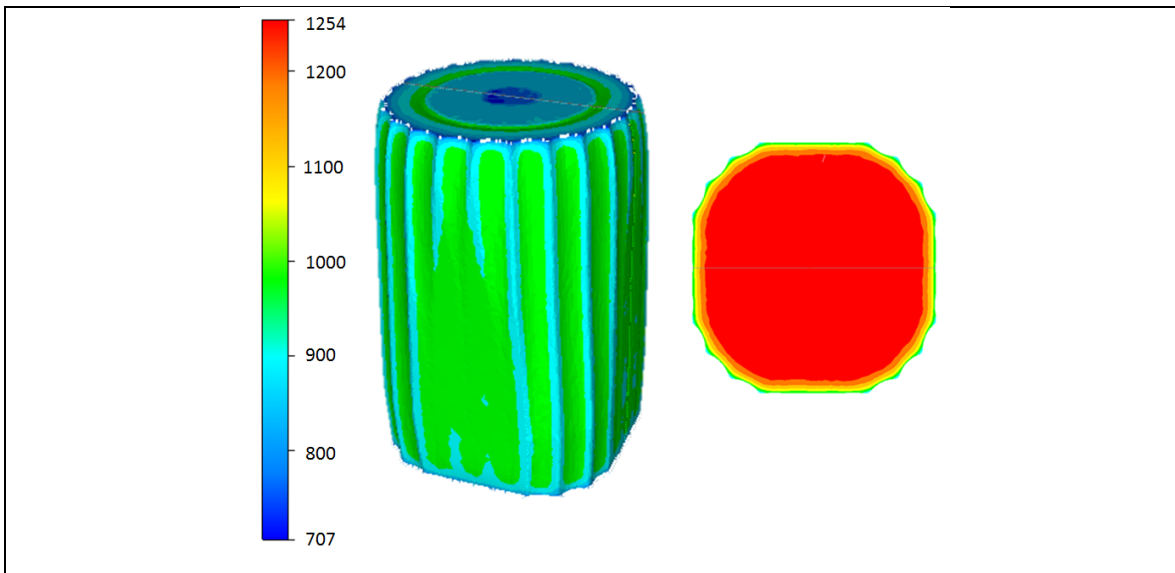
Figure 45 : Interior and exterior ingot temperature (degree C) before upsetting.

3.6.2   In ingot sensor positioning

Sensors were positioned for data recuperation in specific zones during the upsetting simulation. The positioning was based on the observation of actual voids found in a cross-section of an as-cast ingot, see Figure 46. Void closure evolution was targeted along a vertical (sensors A, B, C and D), horizontal (sensors A, E, F and G) and diagonal axis (sensors A, J, I and H). Table 13 shows the positioning of the different sensors, considering

the centre of the ingot's base as the origin, Y and Z horizontal and vertical axis, respectively. All sensors were positioned in a central cut-plane.

Experimental data concerning the press position and forging force were recorded during the entire forging process. The sensor was physically attached to the upper die. Following industrial forging methods, an intermediate die measuring 393.7mm (or 15.5 inches) in thickness, was positioned between the upper die and ingot for upsetting. Post-experiment data processing identified the upsetting stage of the forging process in the initial stages of forging thanks to a characteristic decrease in billet height. A one pass hit with an average press velocity was chosen to simplify initial full field simulations. The most significant press position reduction was selected because of its relevance to the modelling of the upsetting phase.

Reduction was evaluated using initial and final press positions accounting for the intermediary die. The slope of the press position curve was hypothesised constant at 7.5mm.s^{-1} to simplify press velocity calculations, Forge NxT 1.0$^®$ software only allowing a first degree approximation. Possible error, calculated at less than 10%, from FE simulations could come from slope assumptions.
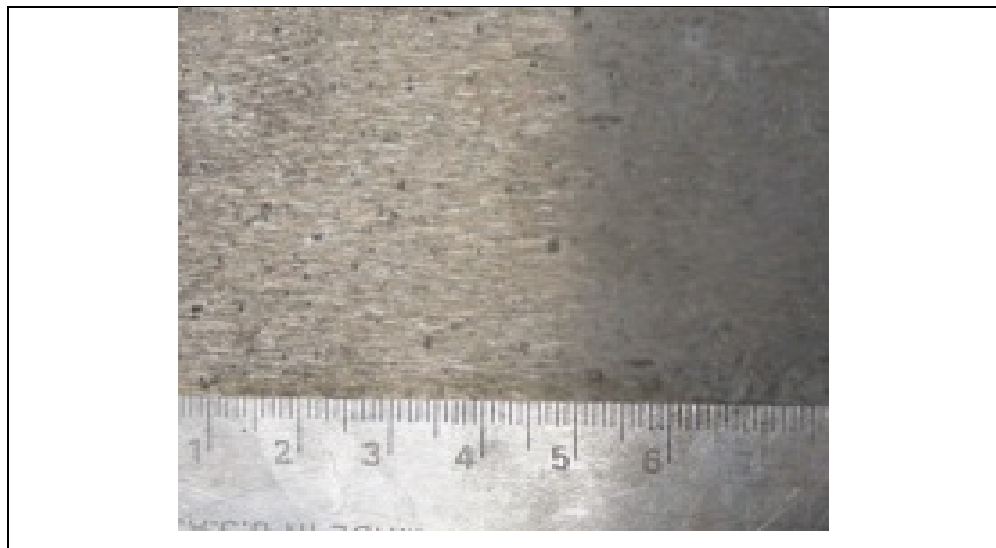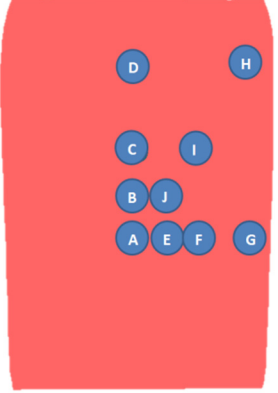

Figure 46 : Internal voids (~1mm) observed from ingot cross-section.

Table 13 : Sensor positioning in billet

Sensor	Y coordinate (mm)	Z coordinate (mm)
A	0	850
B	0	1110
C	0	1350
D	0	1850
E	150	850
F	300	850
G	600	850
H	600	1850
I	300	1350
J	150	1110

3.6.3   Stress and strain evaluation

The evolution of equivalent strain is illustrated in Figure 47. Initial analysis reveals increased deformation in all areas of the workpiece as the upsetting process progresses. Significant deformation, $E_e > 1$ occurs for positions A, B, C, E and J. Positions G and H showing considerably lower strain accumulation $E_e < 0.7$ during the whole process. Deformation is strong initially for position D, but fails to increase consequentially throughout the upsetting process. This can be explained by position D being part of the dead metal zone (DMZ) during forging.

The evolution of the different triaxiality states in billet is shown in Figure 48. Calculations of stress triaxiality using the methodology proposed by Kut (2009) shows the most compressive triaxial state during upsetting for position D. This may be explained because of the proximity of this point to the press's upper die. Intermediate triaxiality states, $T_x \in [-0.3, -0.6]$, are shown for positions A,B,C,E,F,H,I and J. The latter showing a less variable internal compression during the process. Position G, however shows a low triaxiality state, $T_x \in [-0.1, -0.3]$ and an inversed variation contrary to all the other positions in billet. This could be because position G is located outside of the shear bands, and therefore a weaker

level of compression is present at the end of the upsetting process in comparison with that of the beginning.
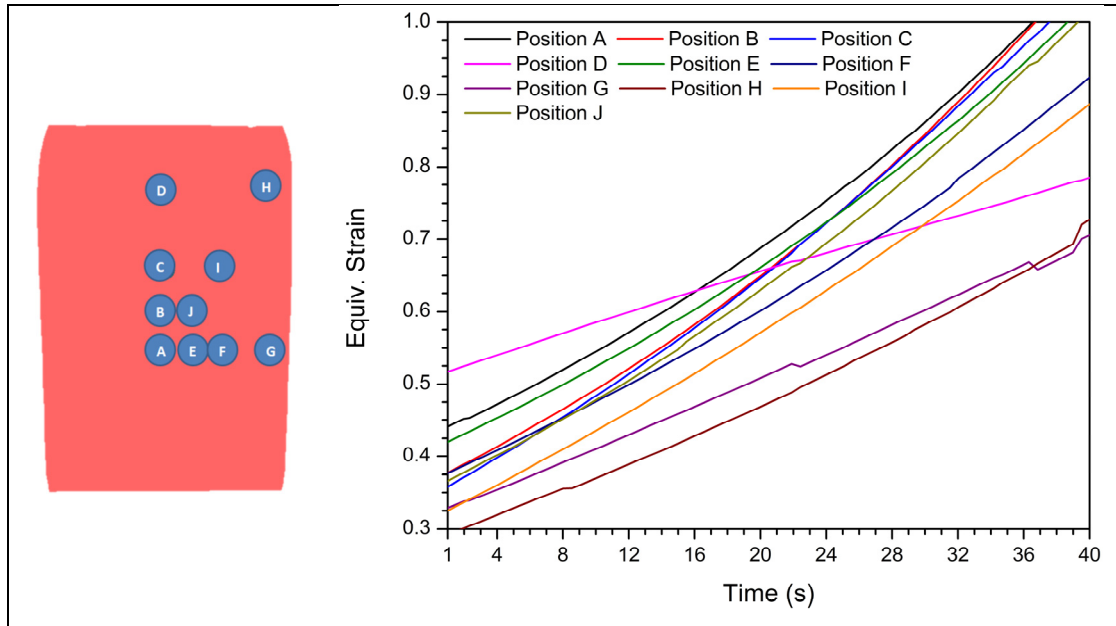

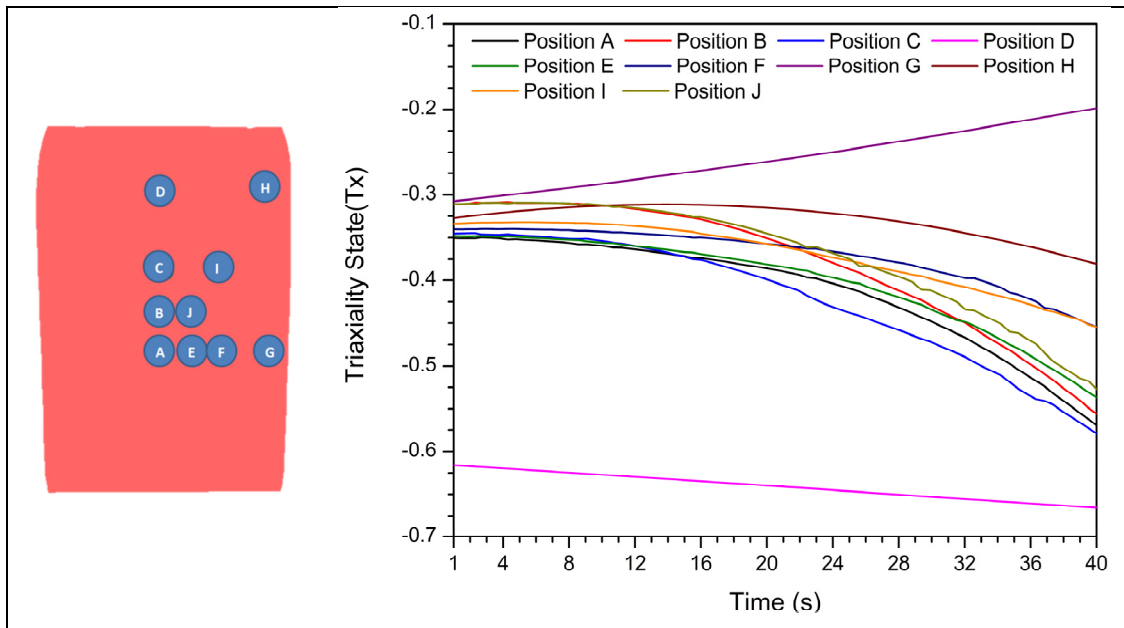Figure 47 : Equivalent strain for large size ingot during upsetting.

Figure 48 : Triaxiality state for large size ingot during upsetting.

3.6.4   Simulation results

Void closure was evaluated during the upsetting process for different positions in the ingot as shown in Figure 49. Initial analysis concluded that a linear study, along either the vertical, horizontal or inclined axis was ill-suited. A decortication by zone of the billet was therefore selected identifying the following areas: the inner core (position A), the outer core (positions B, C, E and J), a mid-billet band (positions F and I), the outer ingot (positions G and H) and finally the upper billet region (position D).

Position D, closest to the upper die in press, was observed to show rapid closure. Interestingly, void closure in the centre of the workpiece, positions A and E, were also demonstrated to regroup conditions for effective void closure. An intermediate zone can be identified, covering positions B, C, F and J in which void closure occurs at a slower rate. Positions G and H, situated close to one of the external ingot faces on the horizontal axis, exhibit prolonged void closure in comparison with all other locations. A correlation can be found with the weak accumulated deformation and triaxiality state in these areas.

Figure 49 also helps understand the effectiveness of the current industrial forging process. An ingot rotation of 90 degrees followed by several hits with the press was found necessary, after the upsetting process, in order to eliminate internal cavities. In this configuration, positions G, F and E are turned respectively into positions D, C and B. More effective void closure for external positions along the diameter of the ingot is therefore achieved using this disposition. However, position H is still situated in the outer ingot after rotation, making void closure in this zone arduous using the upsetting and FM process.
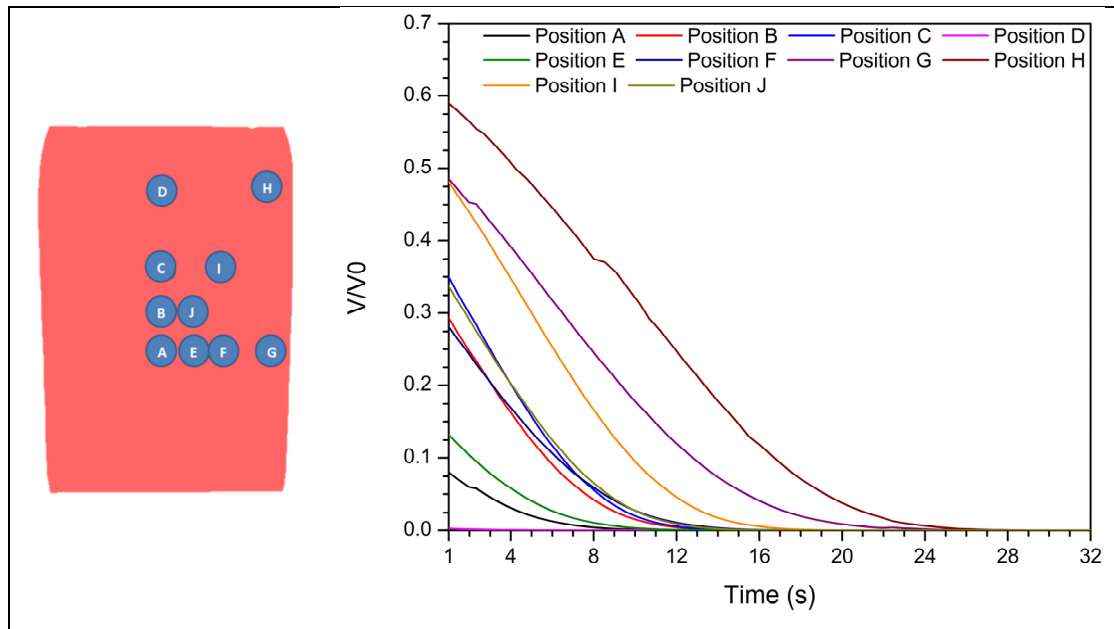
Figure 49 : Void closure for large size ingot during upsetting.

3.7   Conclusions

The following conclusions can be drawn from the present study:

1. The coupled effect of high triaxiality states and values of norton exponent were shown to increase void closure potential.

2. The novel method for void closure evaluation in large ingots proved successful for a wide range of materials.

3. The upsetting process was revealed to be most effective for void closure in central upper billet and core regions. Used as part of the FM process, it was demonstrated to accelerate void closure for initially hard-to-close external positions. Outer ingot positions, particularly in the upper region, were found the most difficult to target.

3.8   Acknowledgements

86

3.9   References

(FORGE NxT 1.0 ®). 694 av. Donat, 06255 Mougins Cedex, France, Transvalor S.A. .

Budiansky, B., et al. (1982). "Void growth and collapse in viscous solids." Pergamon Press, Oxford: 32.

Duva, J. M. and J. W. Hutchinson (1984). "Constitutive potentials for dilutely voided nonlinear materials." Mechanics of Materials **3**(1): 41-54.

K.Chadha, et al. (2015). "An Approach to Develop Hansel-Spittel Constitutive Equation during Ingot Breakdown Operation of Low Alloy Steels." FiMPART: 6.

Kakimoto, H., et al. (2010). "Development of forging process design to close internal voids." Journal of Materials Processing Technology **210**(3): 415-422.

Kim, Y., et al. (2011). "Efficient forging process to improve the closing effect of the inner void on an ultra-large ingot." Journal of Materials Processing Technology **211**(6): 1005-1013.

Kut, S. (2009). "State of Stress Identification in numerical modeling of 3D issues." Archives of Metallurgy and Materials **54**(3).

Lee, B. J. and M. E. Mear (1994). "Studies of the Growth and Collapse of Voids in Viscous Solids." Journal of Engineering Materials and Technology **116**(3): 348-358.

Lee, Y. S., et al. (2011). "Internal void closure during the forging of large cast ingots using a simulation approach." Journal of Materials Processing Technology **211**(6): 1136-1145.

Li, J., et al. (2014). "Simulation of macrosegregation in a 2.45-ton steel ingot using a three-phase mixed columnar-equiaxed model." International Journal of Heat and Mass Transfer **72**: 668-679.

Lin, Y. C., et al. (2008). "Numerical simulation for stress/strain distribution and microstructural evolution in 42CrMo steel during hot upsetting process." Computational Materials Science **43**(4): 1117-1122.

Montheillet, F. and J. J. Jonas (1996). "Temperature dependence of the rate sensitivity and its effect on the activation energy." Metallurgical and Materials Transactions **27**(10): 3.

P. M.Dixit, U. S. D. (2008). Modelling of Metal Forming and Machining Processes: by Finite Element and Soft Computing Methods, Engineering Materials and Processes.

Ragab, A. R. (2004). "Application of an extended void growth model with strain hardening and void shape evolution to ductile fracture under axisymmetric tension." Engineering Fracture Mechanics **71**(11): 1515-1534.

Saby, M. (2013). "Compréhension et modélisation des mécanismes de refermeture de porosité dans les procédés de mise en forme des métaux à chaud." 234.

Tkadlečková, M., et al. (2013). "The effect of boundary conditions of casting on the size of porosity of heavy steel ingot." Journal of Achievements in Materials and Manufacturing Engineering **56**(1): 9.

Tvergaard, V. (1982). "On localization in ductile materials containing spherical voids." International Journal of Fracture **18**(4): 237-252.

Zhang, X.-X. and Z.-S. Cui (2009). "Theoretical study of void closure in nonlinear plastic materials." Applied Mathematics and Mechanics **30**(5): 631-642.

Zhang, X.-X., et al. (2009). "A criterion for void closure in large ingots during hot forging." Journal of Materials Processing Technology **209**(4): 1950-1959.

Zhongxiao, J. and G. W. Stewart. (2000). "An analysis of the rayleigh-ritz method for approximating eigenspaces." Mathematics of computation **70**(234): 10.

CHAPTER 4

ANALYSIS OF VOID CLOSURE DURING OPEN DIE FORGING

Following the previous work, CHAPTER 4 uses the newly developed material specific void closure model to study the effect of initial void positioning in large ingots during an open die forging process for high strength steel P20. The in depth study aims to find high priority locations within the ingot that the current forging process neglects in regards to deformation. Results show that void closure in core regions is particularly efficient during upsetting and the FM process. However, peripheral regions around the ingots centre lack sufficient deformation during upsetting proving the necessity of the FM process for these locations. This Chapter is submitted as an article for Metal Forming 2016 and will be published in a special edition of this Journal.

ANALYSIS OF VOID CLOSURE DURING OPEN DIE FORGING

Nathan Harris [1, a *], Davood Shahriari [1, b], Mohammad Jahazi [1, c]

[1]École de Technologie Supérieure, Département de Génie Mécanique, 1100, rue Notre-Dame Ouest Montréal, Québec, H3C 1K3, Canada
[a]nathan.harris.1@ens.etsmtl.ca, [b]davood.shahriari@etsmtl.ca, [c]mohammad.jahazi@etsmtl.ca

Keywords: Void Closure, Hot Forging, Large Steel Ingot, FEM

4.1 Abstract

Large size forged ingots, made of high strength steel, are widely used in aerospace, transport and energy applications. The presence of internal voids in the as-cast ingot may significantly affect the mechanical properties of final products. Thus, such internal defects must be eliminated during first steps of the open die forging process. In this paper, the effect of in-billet void positioning on void closure throughout the ingot breakdown process and specifically the upsetting step in a large ingot size steel is quantitatively investigated. The developed Hansel-Spittel material model for new high strength steel is used in this study. The ingot forging process (3D simulation) was simulated with Forge NxT 1.0® according to existing industrial data. A degree of closure of ten virtual existing voids was evaluated using a semi-analytical void closure model. It is found that the upsetting process is most effective for void closure in core regions and central upper billet including certain areas within the dead metal zone (DMZ). The volumetric strain rate is determined and two types of inertial effects are observed. The dependence of void closure on accumulated equivalent deformation is calculated and discussed in relation to void in-billet locations. The original combination of information from both relative void closure and the volumetric strain rate provides a way to optimize the forging process in terms of void elimination.

4.2 Introduction

Internal voids can have harmful consequences on material integrity if left unchecked. Their elimination has therefore become a necessary part of the ingot forging process. One such prevailing technique is open die forging, shown to have a significant effect upon material transformation during ingot breakdown Dudra and Im (1990). Voids, developed during the solidification of a large cast steel ingot Lee and Mear (1994) and mostly found in the central upper ingot and in core regions along the central axis Tkadlečková et al. (2013), are significantly affected. Their closure ensures a sound material, an effective forming process and industrial progress in this field. To this end, void closure predictions for large forgings have become a necessity.

The quantification of void closure predictions has been investigated by different researchers. Zhang et al. (2009) propose a semi-analytical formulation of the volumetric strain rate and relative void closure for the introduction of void closure models. Both indicators are dependent of physically interpretable notions such as material influence, n, triaxiality state, T_x and accumulated deformation in-billet, E_e. It is the strain and the Norton exponent effect which reflects material sensitivity. The triaxiality of the stress state is known to greatly influence the amount of the plastic stain which a material may undergo before ductile failure occurs. It is defined as the ratio of hydrostatic pressure, or mean stress, to von Mises equivalent stress. Stress triaxiality factor is mathematically given as:

$$\frac{\sigma_H}{\sigma_{VM}} = T_x = \frac{\frac{1}{3}\sigma_1 + \sigma_2 + \sigma_3}{\frac{1}{\sqrt{2}}\sqrt{(\sigma_1 - \sigma_2)^2 + (\sigma_2 - \sigma_3)^2 + (\sigma_1 - \sigma_3)^2}} \tag{4.1}$$

Although these parameters give a significant amount of information for successful void closure Saby et al. (2015), their applicability to industrial size forgings demands the use of powerful simulation tools Lin et al. (2008).

Numerical modelling of the forging process using the Finite Element (FE) method in a 2D Kakimoto et al. (2010) or 3D Lee et al. (2011, Saby et al. (2013) environment has been a cornerstone for the optimisation of ingot forging in recent decades. Mostly based at a theoretical level, the relevance to industry was limited. As commercial codes and advanced theory Huang. and Wang. (2006, Zhang and Cui (2009, FORGE NxT 1.0 ®) developed, larger forgings were successfully simulated Xu et al. (, Chen et al. (2012) and more complex geometries/problems accounted for Zhang et al. (2012). This meant that the simulation of internal defects, such as porosities and macro-segregation, began to give significant results in terms of understanding ingot forgeability Saby et al. (2014). Quicker and more precise computations consequently put 3D simulations at the cutting edge of process optimisation. However, industrial size ingot simulations remain computationally costly, their fully-combined potential with leading void closure models unexploited.

The current investigation aims to quantify the influence of volumetric strain rate on void closure and the importance of this parameter for a complete void closure analysis. A FE simulation of an industrial size high strength steel forging is developed to study the influence of void position on closure conditions. A dual sided justification for void closure is presented for several positions in-billet. The effects of the combined criteria are discussed for a plausible optimisation of the forging process.

4.3 Finite element analysis

Due to the size and weight of the considered ingot, 40 metric tons, finite element formulations were selected for resolution. The upsetting process was chosen because of the large deformation effects and consequent impacts upon the development of significant void closure factors such as triaxiality and macroscopic equivalent deformation. The latter is a technique aimed at increasing the width of a heated workpiece whilst reducing its length. The very large deformations during upsetting suffered by the material, result in large finite element distortions that require remeshing. The arbitrary Lagrangian Eulerian formulation proposes a very good understanding between these approaches. It has been implemented into

the implicit code Forge NxT 1.0® FORGE NxT 1.0 ®). Throughout the actual upsetting process simulation via this software, thermo-mechanical fields are computed in a Lagrangian manner by implicitly solving the weak form of the balance and heat equations. The mesh velocity, w, is calculated in order to keep the best quality of elements to prevent mesh distortions. Remeshing allows transferring the state variables on the update mesh by considering $(\frac{d_g\varphi}{dt} - \dot\varphi)$ terms that appear in the total derivative $\frac{d_g\varphi}{dt}$ of any variable φ:

$$\frac{d_g\varphi}{dt} = \dot\varphi + (w-v)\nabla\varphi \qquad (4.2)$$

Where $\dot\varphi$ is the material derivative of φ representing the material's internal velocity, v.

4.3.1   Finite element model

A full field finite element simulation was generated in order to obtain significant data for macroscopic equivalent strain and stress tensor components using Forge NxT 1.0®. Initial ingot geometry was modelled using CATIA V5® and pre-upsetting geometry obtained as a result of previous forming techniques in a chain simulation. A schematic diagram is shown in Figure 50. Element size was set at 25mm in order to obtain sufficient precision in results. About 375000 tetrahedrons elements (80000 nodes) were used to discretize the ingot. The dies were modelled as rigid bodies and elastic-viscoplastic behaviour was assumed for the ingot material. An adaptive remeshing on deformation algorithm was implemented in order to increase resulting data precision. Two directions, press direction (vertical axis) and transverse direction (horizontal axis) were identified, as shown in Figure 51. Thermal exchanges including conduction (die and ingot) and convection (circulating air and ingot) were considered in this model. The dies were preheated to 450°C and the ingots initial core temperature set at 1260°C. Heat loss due to radiation was neglected. Contact between the ingot and the press dies was modelled using Coulomb's friction law.

A hydraulic press process was simulated using height reduction and press velocity parameters that were calculated thanks to data supplied by industrial partner, Finkl-Sorel Forge. An intermediate rigid die, was inserted between the upper die and the ingots top.

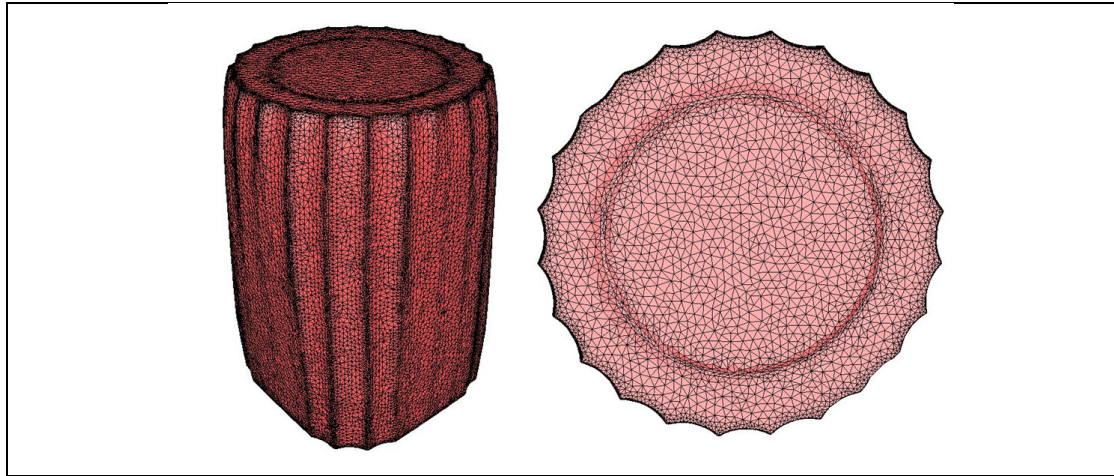Industrial data was analysed and a one hit pass equivalent for upsetting was identified for simulation.

Figure 50 : Ingot geometry and meshing.

4.3.2   Rheological material model

P20, high strength steel, as shown in Table 14, was selected for the present investigation. Hot compression tests were carried out on a Gleeble 3800^{TM} with uniform temperatures ranging from 1050 ˚C to 1200 ˚C for strain rates from 0.25 s^{-1} to 2 s^{-1}. The temperatures were chosen based on industrial ingot forging operating conditions.

Table 14 : Chemical composition of P20 (%wt)

C	Mn	Si	Ni	Cr	Mo	Cu
0.37	0.84	0.39	0.25	1.87	0.46	0.16

The Hansel-Spittel law, Eq (4.3), was adopted using recently characterised material parameters to indicate the dependency of the flow stress on strain, strain rate and temperature K.Chadha et al. (2015).

$$\sigma = 2136.313 e^{-0.00243T} \varepsilon^{0.2315} \dot{\varepsilon}^{0.1215} e^{\frac{0.0001}{\varepsilon}} (1+\varepsilon)^{-0.01T} e^{0.3235\varepsilon} \tag{4.3}$$

This constitutive model is then implemented in the process in order to provide accurate prediction parameters.

4.3.3   Void closure model

Zhang's semi analytical void closure model Zhang et al. (2009) was selected as a base model to calculate void closure for large size ingots. The volumetric strain rate function, Eq (4.4), is obtained in order to account for void shape evolution which is essentially a factor to the specific material's macroscopic strain and internal stress state histories. Relative void volume, Eq (4.5), is achieved through hydrostatic integration, applying constant triaxiality values. The integrated form is therefore a discretised equation.

$$\frac{\dot{V}}{\dot{E}_e V} = sign(\Sigma_m)\left[\frac{3}{2}\left(\frac{3}{2n}|T_x| + \frac{(n-1)(5n+2)}{5n^2} \right)^n + q_1|T_x| + 3q_2 E_e^2 + 5q_3 E_e^4 + q_4 \right] \tag{4.4}$$

$$\frac{V}{V_0} = \exp\left\{ -E_e\left[\frac{3}{2}(\frac{3}{2n}|T_x| + \frac{(n-1)(5n+2)}{5n^2})^n + q_1|T_x| + q_2 E_e^2 + q_3 E_e^4 + q_4\right]\right\} \tag{4.5}$$

4.3.4   Definition of virtual existing voids

In order to obtain sufficient information on void closure for a significant segment of the ingot, ten virtual existing voids (A to J) were designated. Their positioning in regards to a section from the ingot centre/diameter is shown in Figure 51. The workpiece and loading symmetry involved during the upsetting process legitimizes the present investigation for all of the ingot volume situated above the virtual line (A, E, F, G). Therefore, the effect of void position on void closure in a large size ingot can be examined in this area. The effect was studied along a vertical, horizontal and 45° inclined axis in one of the billets diametric planes. The positioning was optimized to suit both the press (Z) and transverse (Y) forging directions.
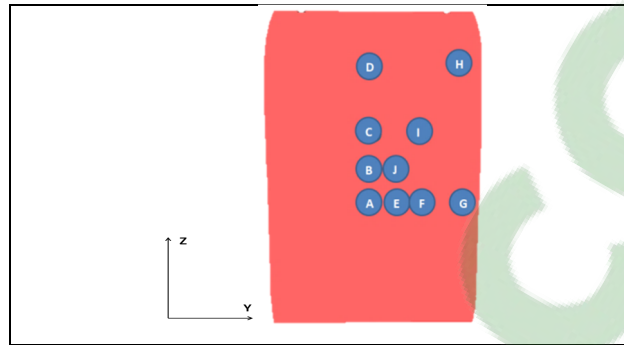
Figure 51 : Void positioning scheme.

The positioning also allows the regrouping of several virtual existing voids to make up characteristic zones in the ingot. The designated zones, shown in Table 15, are useful for a global void closure analysis in a following paragraph.

Table 15 : Characteristic Ingot Regions

Positions regrouped	Characteristic ingot region	
A,E	Ingot core	Inner core
B,C,J,F	Ingot core	Outer core
I	Mid ingot ring	
G,	Outer ingot	Central outer ingot
H	Outer ingot	Upper outer ingot
D	Inner upper ingot (part of the DMZ)	

4.4　　Results and discussion

4.4.1　　Void closure calculation method

Data on triaxiality and macroscopic equivalent strain was gathered using a point tracking technique for the different positions described above. Figure 51 Triaxiality was also calculated, using Eq (4.1), from stress tensor components considering a three dimensional state of stress Kut (2009). Both calculated and triaxiality taken from Forge NxT 1.0® software were found to differ less than 1%. Figure 52 and Figure 53show

triaxiality and strain maps in a diametric plane towards the beginning of the upsetting process (t=10s).

The FE data was used in volumetric strain rate calculations with Matlab 2013, as shown in Figure 54, evaluated using Zhang's semi analytical void closure model Zhang et al. (2009), Eq (4.5). The current model was selected after its predictions were found to correlate with many findings concerning void closure during hot forging processes Lee and Mear (1994). In order to account for specific high strength steel P20 material properties, adapted material constants $\{q_1, q_2, q_3, q_4\}$, used in equations (4.4) and (4.5), were calculated using rational polynomials, function to the materials Norton exponent, identified and approved using curve identification algorithms. The volumetric strain rate function, Eq (4.4), was integrated for constant triaxiality states for $T_x \in [-1, 0]$ in order to obtain relative void volume, Eq (4.5), as shown in Figure 55, for this triaxiality range.

4.4.2   FE results

Triaxiality is initially strongest, $T_x \rightarrow -1$, closest to the forging dies. The characteristic "blacksmith's cross" is visible for this parameter, the weakest compressive state, $T_x \rightarrow -0.2$, observed in the outer ingot mid-section close to the surface. Intermediate triaxiality states, $T_x \in [-0.3, -0.5]$, are detected in the inner upper ingot.

Initial macroscopic equivalent strain is observed strongest, $E_e \rightarrow 0.56$, in the heart of the Dead Metal Zone (DMZ). The applied force from the upper die concentrates in this area also characterised by viscous material unable to move. Internal pressure therefore rises leading to increased strain. A second core for severe strain appears to develop just below the ingot centre.
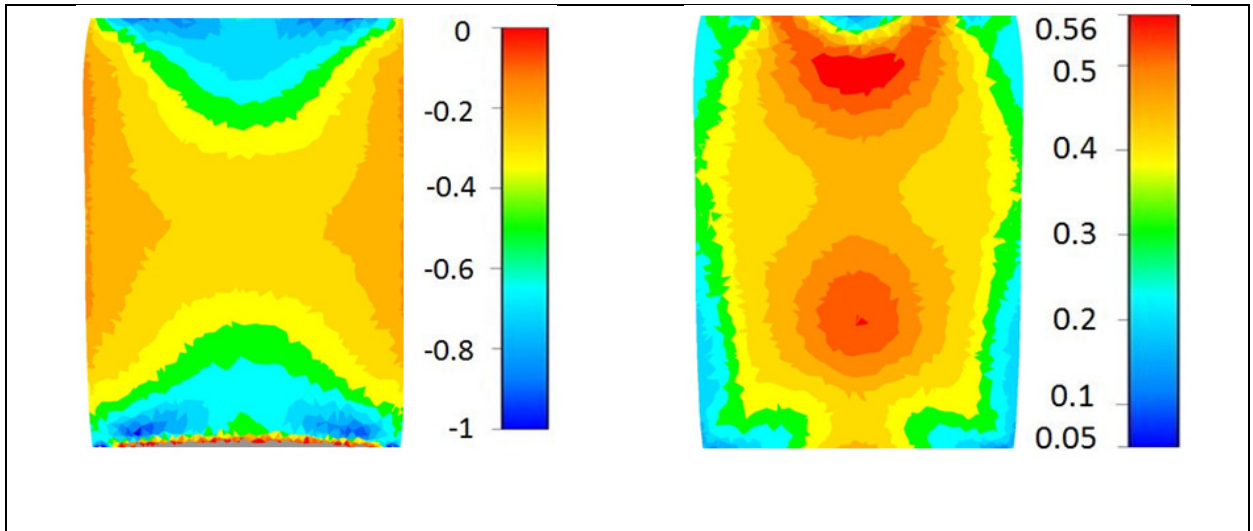
Figure 52 : Initial triaxiality evaluation during upsetting (t=10s).

Figure 53 : Initial macroscopic equivalent strain during upsetting (t=10s).

4.4.3   Void closure analysis

Two types of inertial effects were observed in accordance with in billet positioning. The first, a monotonous decreasing rate of closure was recognized for core locations, sensors A, B, J, E and F, and along the ingots principal axis, sensors A, B, C and D. This type of closure corresponds to elevated terminal accumulated deformation and triaxiality state. The second, in a bell curve form, illustrates a strain rate dependence that increases during the initial phases of the upsetting process before decreasing at its end. It has been noted that the corresponding positions, I, G and H, are all located far from the core in the ingots outer regions, mostly close to the surface.

Relative void volume is shown in Figure 55. Initially all voids are considered completely open, $\dfrac{V}{V_0} = 1$. These values were not represented for considerations concerning graph clarity only. As a general rule, the upsetting process is observed to become less effective, regarding void closure, the further the void location is found from the billets centre (position A). Void closure effectiveness can be found in Table 16. This rule is confirmed along all three studied axis with the exception of position D, found in the Dead Metal Zone (DMZ), for which, void closure appears almost immediate. A closer look at relative void volume, Figure 55, reveals that void closure in function to void position is a gradual phenomenon that can be quantified

by zone. Similar rates of void closure were observed for: positions A and E (the inner core) and positions B, C, J and F (the outer core). Other zones, characterised in Table 15, all showed unique results for void closure. The outer region, central outer region (position G) and the upper outer region (position H), showed the least favourable conditions for void closure. Out of these two, position H, displayed the least effective void closure for the upsetting phase.

Combining the information from both Figure 54 and Figure 55 can better illustrate the results. Figure 55 shows the void position D to be the most effective for void closure. However, position D is also shown to appear in the billets DMZ figuring no material displacement. Figure 54 reveals a near non-existent dependence (less than 5%) on strain at this particular location during the entire upsetting phase. Position H shows the least gain in void closure, Figure 55. This in-DMZ location exhibits low triaxiality states, $|T_x| < 0.4$, but not as little as in the central outer region, $|T_x| < 0.3$. However, the relative void volume in position G decreases quicker than in position H. Figure 55 helps clarify the phenomenon. Position H has longer time related dependence on strain variation (larger bell curve), even though maximum volumetric strain rate is similar. Void closure for H is therefore more difficult because of it being more strain dependent for a longer period of time than in G.

Table 16 : Void closure effectiveness per axis

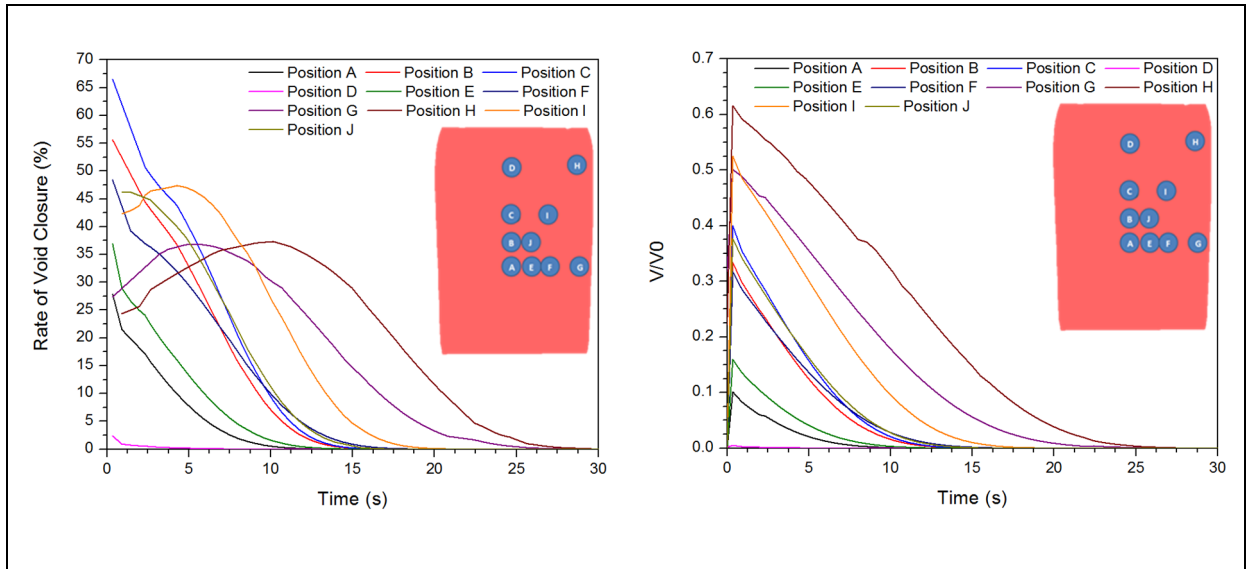| Axis	Void Closure Effectiveness			
	Most Effective			Least Effective
Vertical	D	A	B	C
Horizontal	A	E	F	G
45° inclined	A	J	I	H

Figure 54 : Accumulated equivalent deformation dependence during ingot upsetting.

Figure 55 : Relative void closure during the upsetting process.

4.5 Conclusion

A methodology is proposed to evaluate void closure and observe corresponding forging effects in an industrial size high strength steel ingot. Initial void positon (particularly central regions) and relative strain dependence have significant effects on the void closure. Void closure, although linearly gradual (axis Y and Z), can be observed by zone. The outer ingot, especially upper outer ingot, must be targeted in order to optimize the forging process.

4.6 Acknowledgements

4.7   References

[1]   Dudra, S.P. and Y.-T. Im, *Analysis of void closure in open-die forging.* International Journal of Machine Tools and Manufacture, 1990. **30**(1): p. 65-75.

[2]   Lee, B.J. and M.E. Mear, *Studies of the Growth and Collapse of Voids in Viscous Solids.* Journal of Engineering Materials and Technology, 1994. **116**(3): p. 348-358.

[3]   Tkadlečková, M., K. Michalek, K. Gryc, B. Smetana, P. Machovčák, and L. Socha, *The effect of boundary conditions of casting on the size of porosity of heavy steel ingot.* Journal of Achievements in Materials and Manufacturing Engineering, 2013. **56**(1): p. 9.

[4]   Zhang, X.-X., Z.-S. Cui, W. Chen, and Y. Li, *A criterion for void closure in large ingots during hot forging.* Journal of Materials Processing Technology, 2009. **209**(4): p. 1950-1959.

[5]   Saby, M., P.O. Bouchard, and M. Bernacki, *Void closure criteria for hot metal forming: A review.* Journal of Manufacturing Processes, 2015. **19**(0): p. 239-250.

[6]   Lin, Y.C., M.-S. Chen, and J. Zhong, *Numerical simulation for stress/strain distribution and microstructural evolution in 42CrMo steel during hot upsetting process.* Computational Materials Science, 2008. **43**(4): p. 1117-1122.

[7]   Kakimoto, H., T. Arikawa, Y. Takahashi, T. Tanaka, and Y. Imaida, *Development of forging process design to close internal voids.* Journal of Materials Processing Technology, 2010. **210**(3): p. 415-422.

[8]   Lee, Y.S., S.U. Lee, C.J. Van Tyne, B.D. Joo, and Y.H. Moon, *Internal void closure during the forging of large cast ingots using a simulation approach.* Journal of Materials Processing Technology, 2011. **211**(6): p. 1136-1145.

[9]   Saby, M., M. Bernacki, E. Roux, and P.O. Bouchard, *Three-dimensional analysis of real void closure at the meso-scale during hot metal forming processes.* Computational Materials Science, 2013. **77**(0): p. 194-201.

[10]   FORGE NxT 1.0 ®, Transvalor S.A. : 694 av. Donat, 06255 Mougins Cedex, France.

[11]   Zhang, X.-X. and Z.-S. Cui, *Theoretical study of void closure in nonlinear plastic materials.* Applied Mathematics and Mechanics, 2009. **30**(5): p. 631-642.

[12]   P., H.Z. and W. J., *Nonlinear Mechanics of Solids containing Isolated Voids* Applied Mechanics Review, 2006. **59**: p. 20.

[13]   Chen, K., Y. Yang, G. Shao, and K. Liu, *Strain function analysis method for void closure in the forging process of the large-sized steel ingot.* Computational Materials Science, 2012. **51**(1): p. 72-77.

[14]   Xu, B., M. Sun, and D. Li, *Modeling of The Void Close Behavior in a 100t Ingot during Hot Forging.* Metal Forming: p. 4.

[15]   Zhang, X., F. Ma, K. Ma, and X. Li, *Multi-scale Analysis of Void Closure for Heavy Ingot Hot Forging.* Modern Applied Science, 2012. **6**(10): p. 11.

[16]   Saby, M., M. Bernacki, and P.-O. Bouchard, *Understanding and Modeling of Void Closure Mechanisms in Hot Metal Forming Processes: A Multiscale Approach.* Procedia Engineering, 2014. **81**(0): p. 137-142.

[17]   K.Chadha, D.Shahriari, and M.Jahazi, *An Approach to Develop Hansel-Spittel Constitutive Equation during Ingot Breakdown Operation of Low Alloy Steels.* FiMPART, 2015: p. 6.

[18]   Kut, S., *State of Stress Identification in numerical modeling of 3D issues.* Archives of Metallurgy and Materials, 2009. **54**(3).

CHAPTER 5

DEVELOPMENT OF A PREDICTION TOOL FOR SUCCESFUL FORGING

5.1   Forge Calculus – prediction tool

Forge Calculus is an in house code which was developed and continues development in the framework of the current M.A.Sc. The program was written and is run using Matlab 2012.The code analyses .csv files exported directly from the position and force sensors used at Sorel Forge.

Forge Calculus analyses forging data with a minimum of human input. A forging plan is needed initially, see example p131, in order for a complete analysis to run. The code is written to calculate and quantify indicators for each of the sequences described in 2.2. Individual or global results can be visualised.

Global results include a statistical analysis of the forging database formed with the initial data analysis code. Results show trends and standardisation measures for over 70 forged parts. The amount of data analysed validates the significance of the averages calculated. The quantification of indicator values and variability can then be used for comparison with real-time forgings. These three functions are separated in order to increase program usability. The main user interface can be seen in Figure 56.
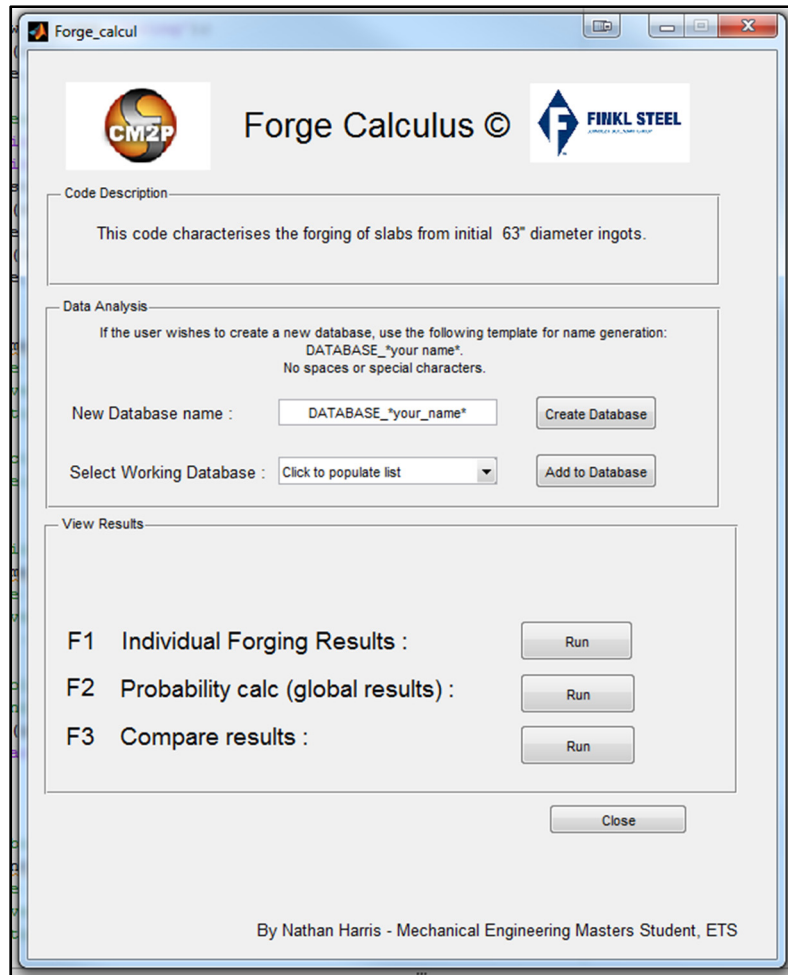
Figure 56 : Forge Calculus main interface

5.1.1 In depth analysis of successful forgings

This section contains the models and algorithms used for studying each of the different sequences in 2.2. The similarities observed in the forging process between upsetting and FM respectively Cogging and Finishing are also reflected in the models conceived and the code generated.

5.1.1.1 Sequence models

Upsetting and FM model

The first two sequences use the mathematical model in Figure 57 based on the following premises:

- Contact is achieved between the workpiece and the factory floor.
- An intermediate die is needed during forging.
- The position sensor was successfully calibrated at the beginning of the working day. ('0' occurs when the upper and lower dies touch).
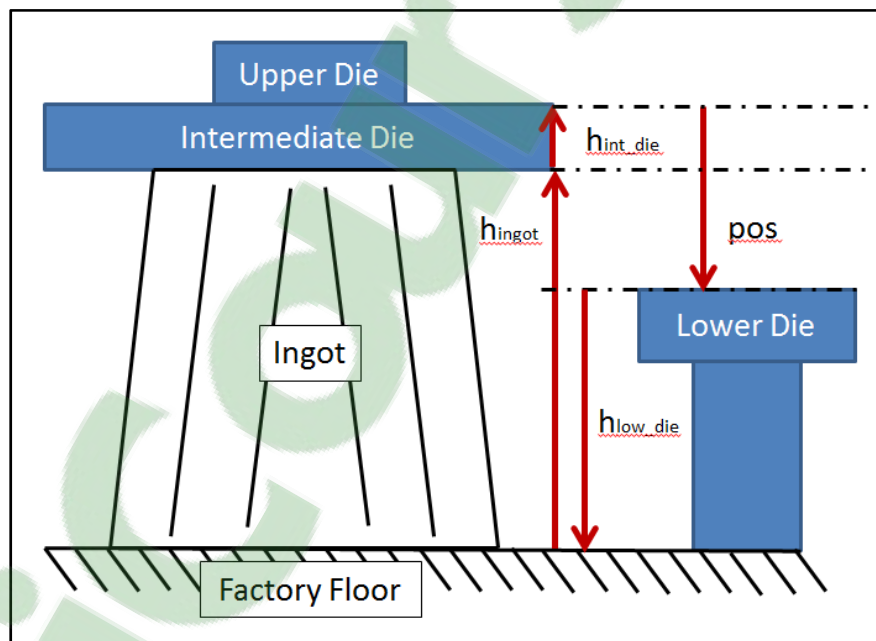
Figure 57 : Upset and FM modeling diagram

The height of the ingot during forging is thus deduced as shown in (5.1).

$$h_{ingot} = pos + h_{low\_die} - h_{int\_die} \qquad (5.1)$$

Ingot width or height is given directly by *pos* during cogging and finishing because no intermediate die is used and contact is therefore produced between upper die, workpiece and the lower die.

A constant volume hypothesis is used in order to calculate ingot diameter and other initial sequence indicators for upsetting and FM process. The loss of oxidised layers is accounted for in a later calculation. Calculations for the upsetting sequence are derived from Figure 58 which shows both initial and final forms. h_1 represents the height loss of the upset material.
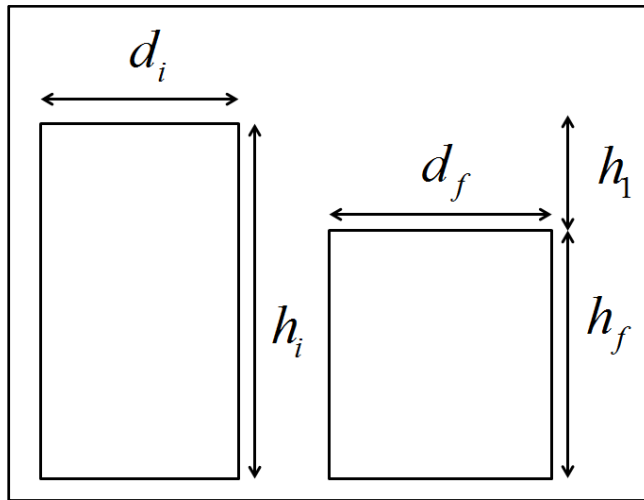

Figure 58 : Upsetting initial and final states

The percentage of upset material is calculated as:

$$r_{upset} = \frac{h_1}{h_i} \tag{5.2}$$

The reduction is deduced using:

$$r = \frac{h_i}{h_i - h_1} \tag{5.3}$$

Reduction is verified according to the following formula and ingot height after upsetting (5.1) :

$$h_f = \frac{1}{r} h_i \tag{5.4}$$

The final workpiece diameter is then calculated as:

$$d_f = d_i . \sqrt{r} \tag{5.5}$$

An identical method is applied for FM sequence calculations.

Cogging and Finishing model

Cogging and Finishing models are based on Figure 59. Three stages are depicted; before bite, after bite and before the consecutive bite. The third stage shows the manipulator having advanced the workpiece of a certain feed length in order to continue forging.
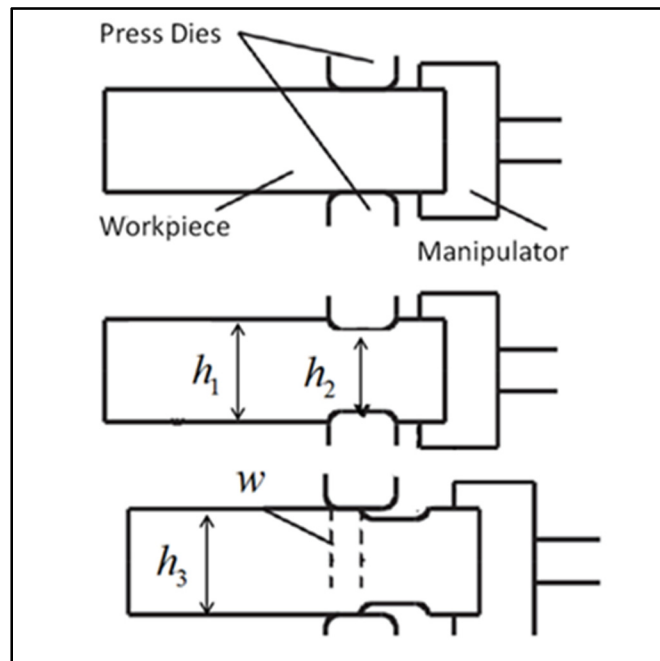

Figure 59 : Cogging and finishing model

Bite depth and width (or Anvil Width Ratio – AWR) are calculated as

$$\Delta h = h_1 - h_2 \tag{5.6}$$

$$r_{AWR} = \frac{w}{h_3} \tag{5.7}$$

The half forging ratio indicates the time taken to forge half of the part in comparison to total forging time.

$$r_{hf} = \frac{t_{hf}}{t_{tot}} \tag{5.8}$$

All sequence models

All equations in 5.1.1 are initially calculated as instantaneous values before using the averages for individual forging indicator results, see 0. This allows the visualisation of indicator evaluation during forging before consulting mean values. Upper die velocity, v_i, and force ratio, r_{F_i}, are given as an example: For an instant i:

$$v_i = \frac{\Delta h_i}{\Delta t_i} = \frac{h_{i+1} - h_{i-1}}{t_{i+1} - t_{i-1}} \tag{5.9}$$

$$r_{F_i} = \frac{F_i}{F_{max}} \tag{5.10}$$

Δh_i and Δt_i representing the variation in part height and the time taken respectively during the instant i.

Averages are calculated using the arithmetic mean value:

$$\bar{x} = \frac{1}{n} \sum_{i=1}^{n} x_i \tag{5.11}$$

n being the amount of samples.

Material loss during forging

The forging plan, see APPENDIX I, p131, shows final measurements and weight for a forged part. The length displayed corresponds to the length of useable material after machining. The metal density per forging can therefore be deducted using (5.12) knowing the final shape is a slab.

$$\rho = \frac{weight}{length * height * width} \tag{5.12}$$

This formula assumes the metal density to be constant in the solidified steel slab.

Metal density is used to calculate initial volume before forging, knowing initial weight (Appendix I, p131) and the volume percentage of the ingot hot top.

$$V_i = \frac{(1 - perc_{hottop}) * initial\_weight}{\rho} \tag{5.13}$$

Ingot geometry after finishing can be found in Appendix I, p131. A more precise calculation for volume after forging is considered, accounting for the billet's rounded edges using the following hypothesis:

- The length of useable material after machining is equal to l_1

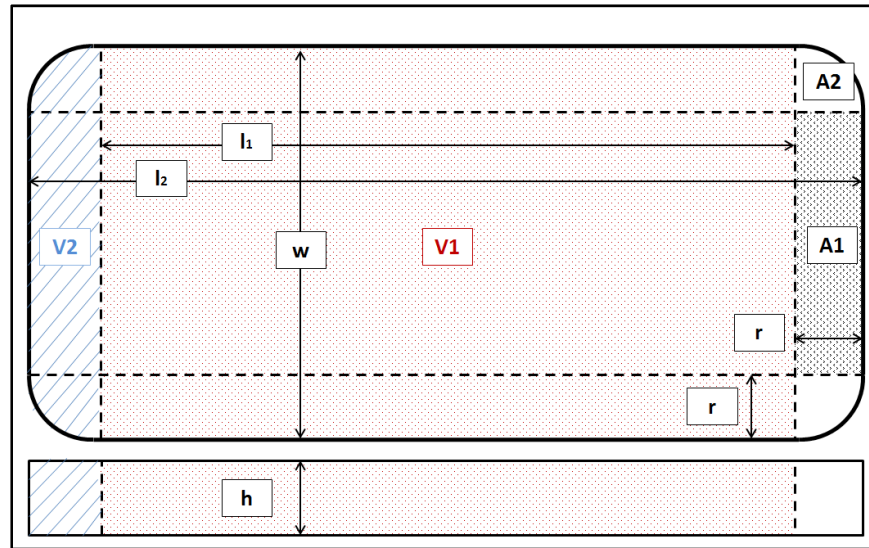- The corners all have the same radius, r, after forging.

Figure 60 : Billet final volume schematic

Final width and height are read using Appendix I, p131, and verified using sensor data. The final volume is calculated as:

$$V_f = V_1 + 2*V_2 \tag{5.14}$$
$$V_1 = l_1 * w * h$$
$$V_2 = (A_1 + 2*A_2)*h$$
$$A_1 = (w - 2*r)*r$$
$$A_2 = \frac{\pi r^2}{4}$$
$$r = l_2 - l_1$$

Process efficiency in terms of volume, or loss of volume, can be calculated with (5.15).

$$\eta_{tot} = \frac{V_f}{V_i} \tag{5.15}$$

The weight of lost material can be quantified as can the associated cost using equations (5.16) and (5.17).

$$weight\_loss = (1 - \eta_{tot}) * V_i * \rho \tag{5.16}$$

$$worth = \kappa_{steel\_grade} * weight\_loss \tag{5.17}$$

With κ_{steel_grade} the cost of the specific steel per kilo.

The efficiency of the finishing sequence can be assessed using the previous method with the part volume after cogging, see Appendix I, p131.

$$\eta_{finish} = \frac{V_f}{V_{after\_cog}} \tag{5.18}$$

Process efficiency can also be calculated for the first three sequences in the following manner:

$$\eta_{tot} = \prod_i \eta_i = \eta_{upset} * \eta_{FM} * \eta_{cog} * \eta_{finish} \text{ with } \eta_{seq1-3} = \eta_{upset} * \eta_{FM} * \eta_{cog} \tag{5.19}$$

$$\eta_{seq1-3} = \frac{\eta_{tot}}{\eta_{finish}} \tag{5.20}$$

5.1.1.2 Sequence algorithms

The main algorithms used in Forge Calculus are detailed in this paragraph. A simplified code is presented for a better understanding of the software's logic. The accuracy of the results obtained from the previous models depends on sensor precision, namely the sampling frequency and discretisation. Elimination of unwanted movements or noise was also an important task.

Terminology:

DB: Database

<u>Underlined word:</u> Major sub-routine that will be explained

Bold word: Important step in the program

Main

Program description: The main is used to run Forge Calculus and all sub-routines when they are asked to. The information is read, analysed and the results displayed using an intuitive user interface.

Simplified code:

Initialisation
Generate Main User Interface
    Create new /Load existing DB
Collect Information if asked
    Read sensor .csv files
    Determine if the file is new/ the next part of an existing file/ or has already been analysed.
    If file=new
        Then   Create new entry in DB using a standardised template
               Data Analysis
               Fill the template
    If file=next part of an existing file
        Then   Load existing file template
               Data Analysis
               Fill existing file template
    End If
    Save DB
Analyse DB if asked (see Appendix II, p133, for DB structure at this point)
    Sort DB into Sequences
    Create new Sequence DB's
    Save Sequence DB's
    If Individual results selected
        Then   Display selected data
    Else if Global results selected
        Then   **Run Statistical Analysis for selected indicator**
               Show Results
    End If
End of Main

Data Analysis

Program description: This sub-routine is the bedrock for the Forge Calculus. All future analysis for individual and global results depends on the values calculated in Data Analysis. The data file is separated into several parts equivalent to different identified sequences. An essential part of each sequence is determining the moment when contact is established

between the upper die and the workpiece (local force condition) and the moment when the contact is broken (local position condition). As previously explained, upsetting and the FM process respectively cogging and finishing both have similar source code. The mathematical formulae can be found in 5.1.1.1.

Simplified code:

Determine which sequence is currently under analysis
If sequence = Upsetting
    Then load initial geometry for specific casting number
    Identify specific sequence time delimiters, t_1 and t_2
    For t_1 to t_2
        Calculate start and finish stroke times, t_i
    End for
    Calculate the variations in position, speed and force for the t_i
    Calculate Upsetting indicators (5.1.1.1)
    Calculate Geometry and weight after upsetting
Else if sequence = FM
    Then load end of upset geometry for specific casting number
    Identify specific sequence time delimiters, t_1 and t_2
    For t_1 to t_2
        Calculate start and finish stroke times, t_i
    End for
    Calculate the variations in position, speed and force for the t_i
    Calculate FM indicators (5.1.1.1)
    Calculate Geometry and weight after FM
Else if sequence = Cogging
    Then load end of FM geometry
    Calculate the time delimiters, t_1 to t_n, that correspond to a 90 rotation of the workpiece
    Assign work on 'width' or 'height' to corresponding delimiters
    i=1
    While i<=n
        For t=t_i to t=t_{i+1}
        Calculate time delimiters, tt_2 to tt_m, that correspond to start of pass (reversal in travelling)
        j=1
        While j<=m
            For t=tt_j to tt_{j+1}
            Calculate start and finish stroke times, ttt_i
            Calculate the variation in position, speed and force for the ttt_i
            Calculate Cogging Indicators
            End For

j=j+1
End While
End For
i=i+1
End While
Calculate cogging geometry
Else If sequence = Finishing
Then load end of cogging geometry
Calculate the time delimiters, t_1 to t_n, that correspond to a 90 rotation of the workpiece
Assign work on 'width' or 'height' to corresponding delimiters
i=1
While i<=n
For t=t_i to t=t_{i+1}
Calculate time delimiters, tt_2 to tt_m, that correspond to start of pass (reversal in travelling)
j=1
While j<=m
For t=tt_j to tt_{j+1}
Calculate start and finish stroke times, ttt_i
Calculate the variation in position, speed and force for the ttt_i
Calculate Finishing Indicators
End For
j=j+1
End While
End For
i=i+1
End While
Calculate finishing geometry
End If
End of Data Analysis

Statistical Analysis

Program description: The statistical analysis program analyses the individual sequence databases created in Main. Twenty probability density models, see Appendix III, p135, are available for comparison. The selected indicator distribution is analysed using relevant density functions and the results are classed. The most suitable model is integrated between limits set by the user to calculate event probability.

Simplified code

Create a simplified histogram
For i=1 to the number of distributions to compare
If the data meets model requirements
   Then **Calculate probability density function**
       Calculate comparison indexes: NLogL, BIC, AIC, AICc
End If
Compare results and sort list
Create a more detailed histogram
Add three best comparisons
Integrate most suitable function if probability calculation is required
End of Statistical Analysis

5.1.1.3 Example of application

The following section shows application of the previous code to one forged part. This particular file was chosen because of the high frequency of measure and precision entailed in the ensuing calculations. The data for the forged part is split into two files. The first regarding the Upsetting, FM and Cogging processes. The second concerns the Finishing process. Both files contain between 20000 and 25000 lines of data to be analysed each representing two hours of data recording. Part temperature was homogenised in a furnace during the two recordings in order to obtain better workability for the finishing sequence.

Forging Charts

The forging chart (hydraulic press position – blue, and Forging Force – green) for Files 1 and 2 can be seen in Figure 61 and Figure 62. The global index on the x axis corresponds to the number of the line of data. In this case the data from 15000 to 22000 was removed because the forging had already completed. The different sequences of Upset (1), FM (2) and Cogging (3) have been outlined in order to cross reference the following analysis with the Forging chart, Figure 61. The whole of the Figure 62 is the second and final forging for this part, also known as Finishing.
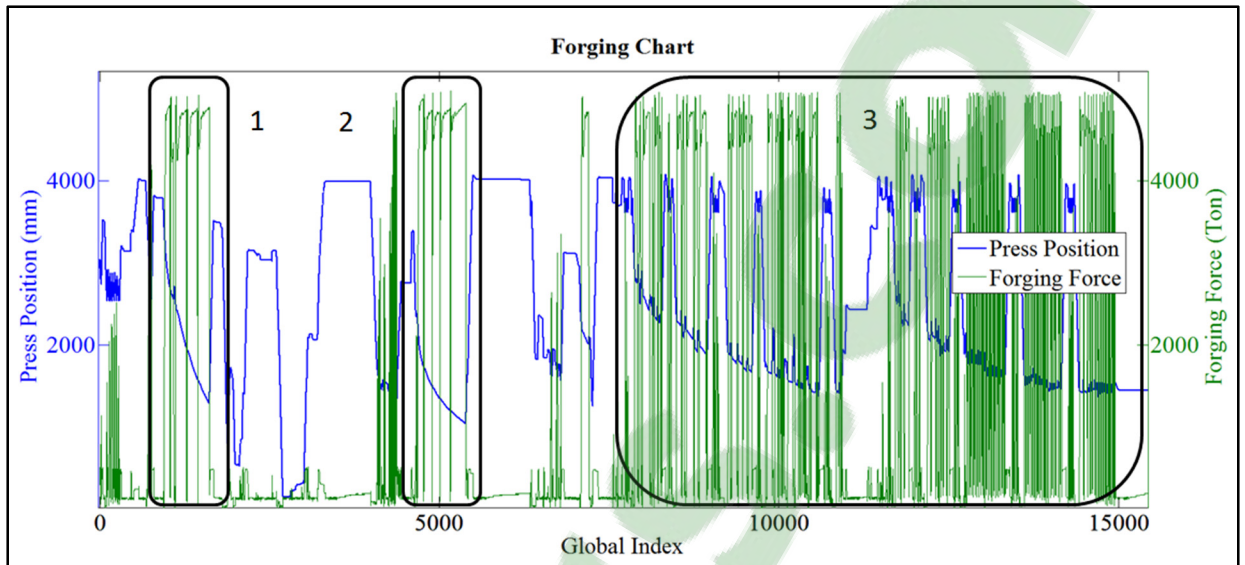
Figure 61: Forging chart – First forging, 1: Upsetting, 2: FM, 3: Cogging
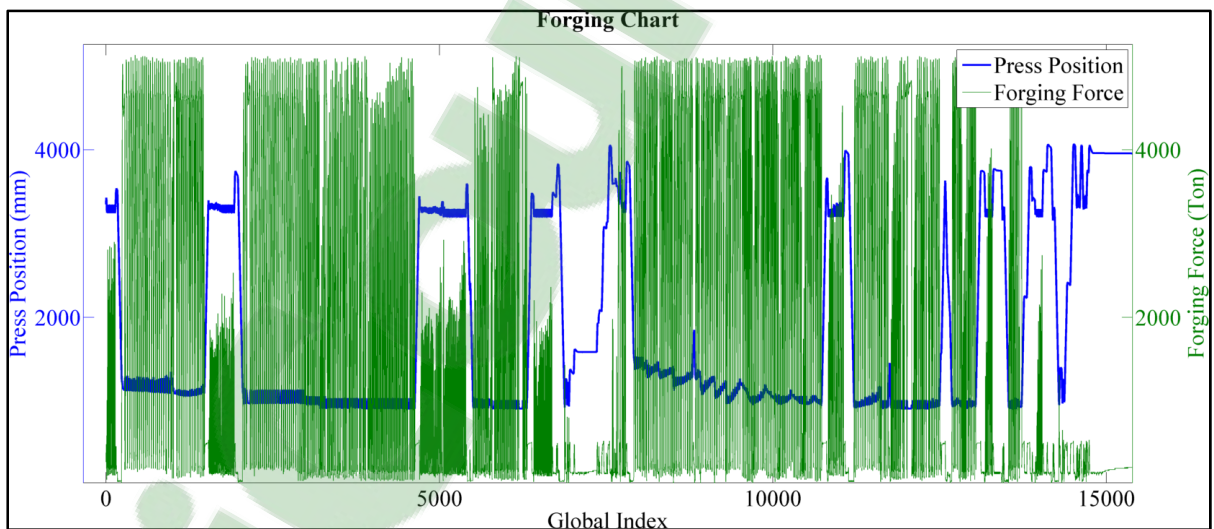
Figure 62 : Forging chart - Second forging, Finishing

Two conditions are necessary in order to successfully calculate stroke times, a crucial step in the forging data analysis algorithm. The first is the need for a sufficient forging force. The second, that material deformation only occurs when the upper anvil draws nearer to the lower anvil. These two conditions can be modelled through equations and algorithms. The force condition is predominant and as such is the first filter used in this analysis. The force filter results are then used as input for the position filter or second condition.

The force filter can be seen for The Upsetting and FM sequences respectively in Figure 63 and Figure 64. The forging force is represented alongside local minima (black circles) and local maxima (red circles) in each graph. The upper graph shows unfiltered results which contain several parasitic values due to sensor precision. The first stage of the force filter, seen in the middle graph, cleans and calculates alternating data minima and maxima. The second stage, the lower graph, delimits each force peak either side. The two delimiting values and the maximum of each force peak are inputs for the position filter.

Notice that even though the Upset and FM processes are theoretically one stroke sequences several anvil blows can be observed, five blows being used for this particular forging. This is because the maximal forging force of 5000T has been reached and the ingot to forge is too massive for brute force alone. A slight momentum is given to the upper anvil in order to compensate this lack.
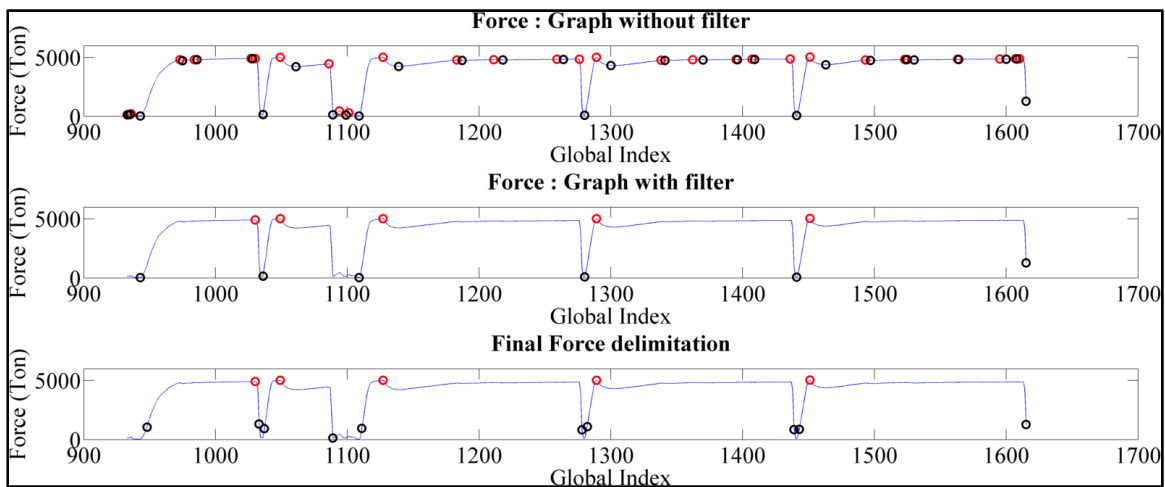
Figure 63 : Upset sequence, Force filter
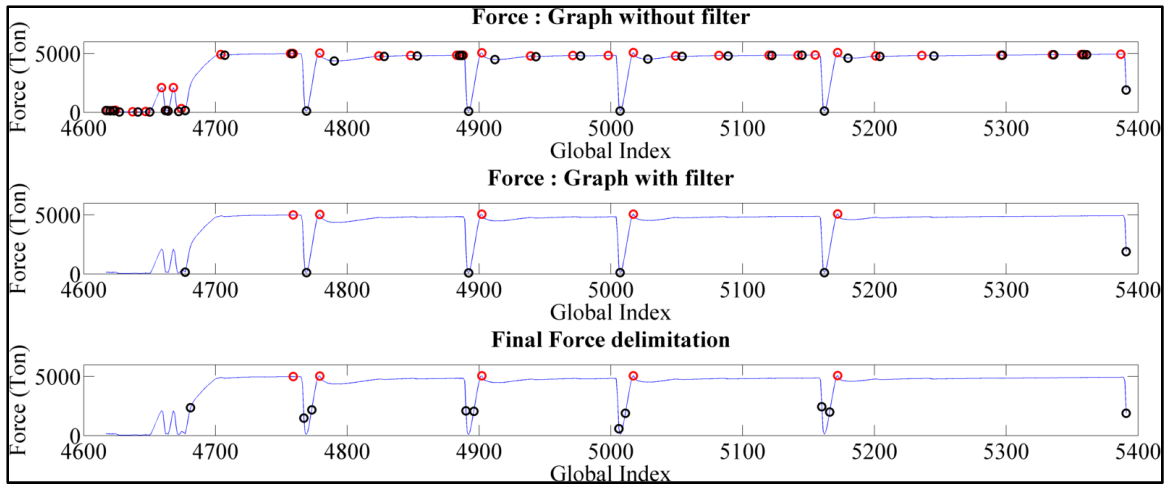
Figure 64 : FM sequence, Force filter

The position filter analyses a triplet of global indexes [force peak start, force peak maximum, force peak stop] for each force peak previously recognised. The values are transferred to the press position curve. A search for start hit press position is accomplished for values between force peak start index and force peak maximum index. A search for stop hit press position is then carried out for values from force peak maximum to force peak stop. Criteria for a successful search include a sufficient forging force (equivalent to forging values superior to a threshold which is a percentage of the current force peaks maximal value) and a decreasing position curve. Part reduction curves for the Upset and FM process of this forging can be seen respectively in Figure 65 and Figure 66. The start and stop hits for each force peak are represented by the red and black circles.
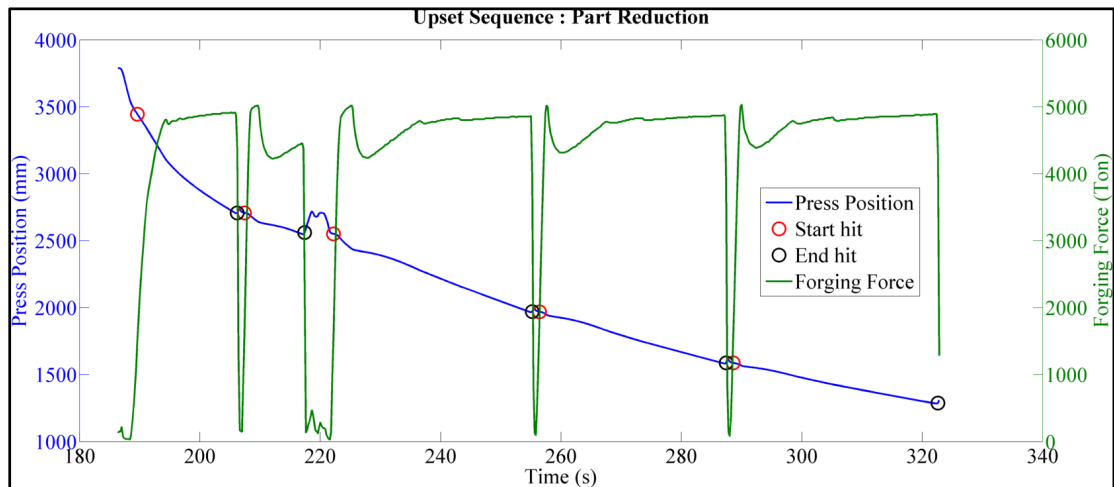
Figure 65 : Upset sequence, Part reduction
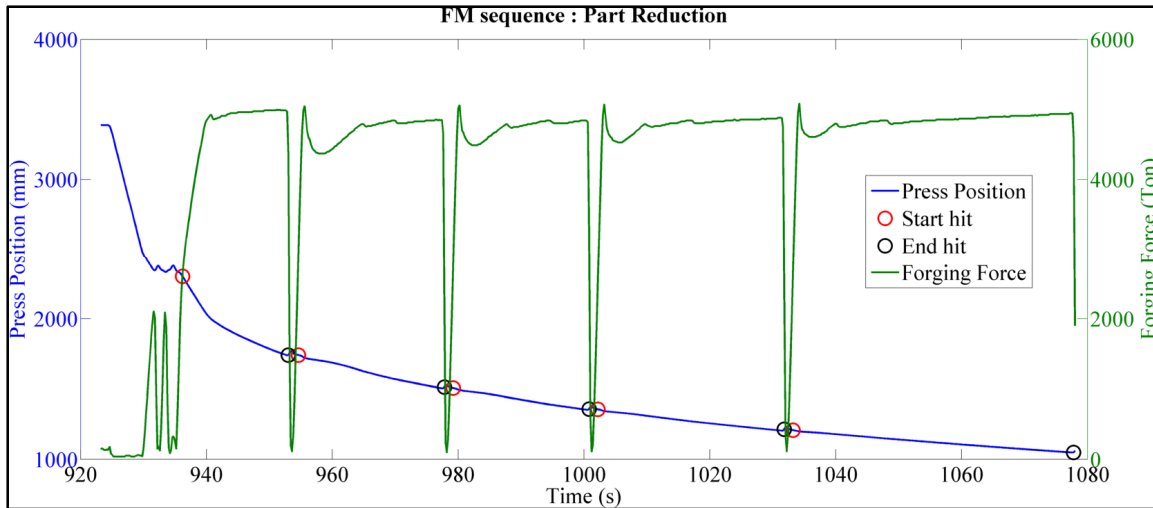
Figure 66 : FM sequence, Part reduction

The calculation of process indicators is then simply the application of the equations from 5.1.1.1. Table 17 and Table 18 show results for both sequences per hit of the anvil. Press speed is initially high (30-40 mm.s^{-1}) before rapidly decreasing as the anvil loses momentum and the forged material becomes more compressed. The Upset sequence shows higher press velocity values than that of the FM sequence. This shows that the material effects created during Upsetting must be overcome during FM. Table 19 shows average results for both sequences. These results are less representative of the process because the sampling period is larger, but the results are useful for simple process characterisation and can be applied in FE process simulations.

Results per hit

Table 17 : Upset results per hit of anvil

UPSET	Start time (s)	Stop time (s)	Amount Upset (mm)	Press velocity (mm.s^{-1})
hit 1	189.6	206.2	738.12	44.65
hit 2	207.4	217.4	148.08	14.80
hit 3	222.2	255.2	580.89	17.60
hit 4	256.4	287.4	381	12.29
hit 5	288.6	322.6	300.22	8.8

Table 18 : FM results per hit of anvil

FM	Start time (s)	Stop time (s)	Amount Upset (mm)	Press velocity (mm.s⁻¹)
hit 1	936.2	953	560.83	33.38
hit 2	654.6	977.8	227.58	9.81
hit 3	979.2	1008	150.11	4.8
hit 4	1022	1031	142.24	4.81
hit 5	1033	1077	158.49	3.55

Average results

Table 19 : Average Upset and FM indicators

	Process time (s)	Amount Upset (mm)	Average velocity (mm.s⁻¹)	Reduction	Percentage of Upset
Upset	125	2148	17.2	2	49.7
FM	135	1239	9.1	1.12	57.3

The real difficulty of this analysis is the flexibility of the code, especially concerning the filters. The same or very similar filters are used for the cogging and finishing sequences even though the data and consequential curves are a very different form. The code must also be able to cope with unexpected operator movements during forging. Each forging is completed with over 95% being manual, each operator reacting differently to the state of the ingot based on his past experience and what he sees in front of him. Patterns are therefore a lot more subtle to recognise when coding.

The approach to analysing the Cogging and Finishing sequences follows a logic that aims to apply the same methods and algorithms used in the Upset and FM analysis. The data range is split into shorter working sequences in order to increase the precision of results. Definition of work sequences are shown in Figure 67 and Figure 68. The algorithm determines an indicator based on press position which shows each time the manipulator rotates 90 degrees with part in hand. Therefore separating forging mainly part width (above indicator) and mainly part height (below indicator). As previously specified in 2.4.2, the press position curves for

Cogging and Finishing display significantly different aspects due to part shape at time of forging.
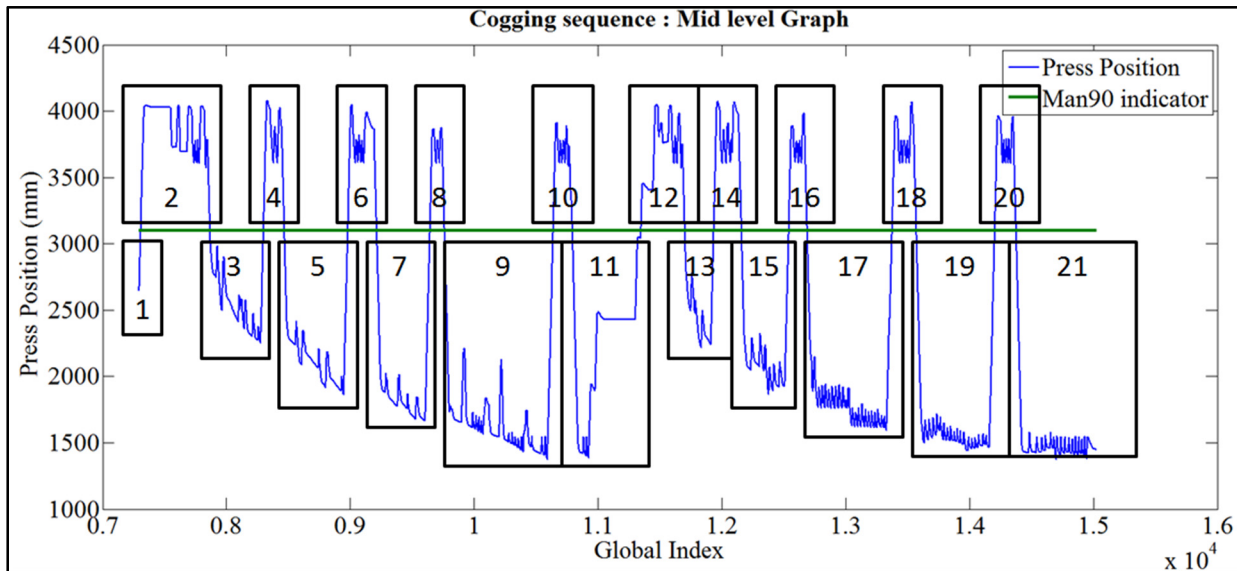
Figure 67 : Cogging - Work sequence definition
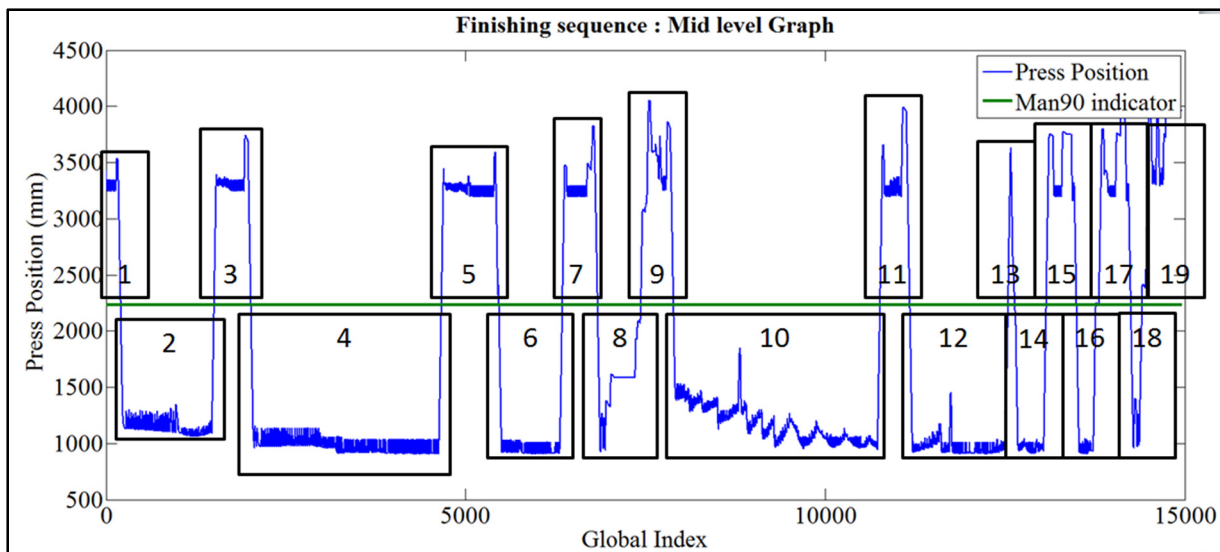
Figure 68 : Finishing - Work sequence definition

As well as rotating 90 degrees around its principal axis in between working on part height and width, the part also travels to and from the anvils in order to complete successive blows during the Cogging and Finishing sequences. A pass is defined as a significant change in part

travel direction. Passes can include a variable amount of work or blows from the press depending on forging progression. The number of hits increases with forging progression and part length. Each work sequence can contain a variable amount of passes as shown by Figure 69 and Figure 70. A decrease and increase respectively in travelling value means that the manipulator grabbing hand and the part are advancing respectively towards and away from the press anvil. A Work sequences are observed to incorporate more passes during Finishing in relation to Cogging. A greater number of force peaks per pass are counted during Finishing. However the deformation per hit is reduced. A pass is considered insignificant if it is defined without corresponding force peaks.
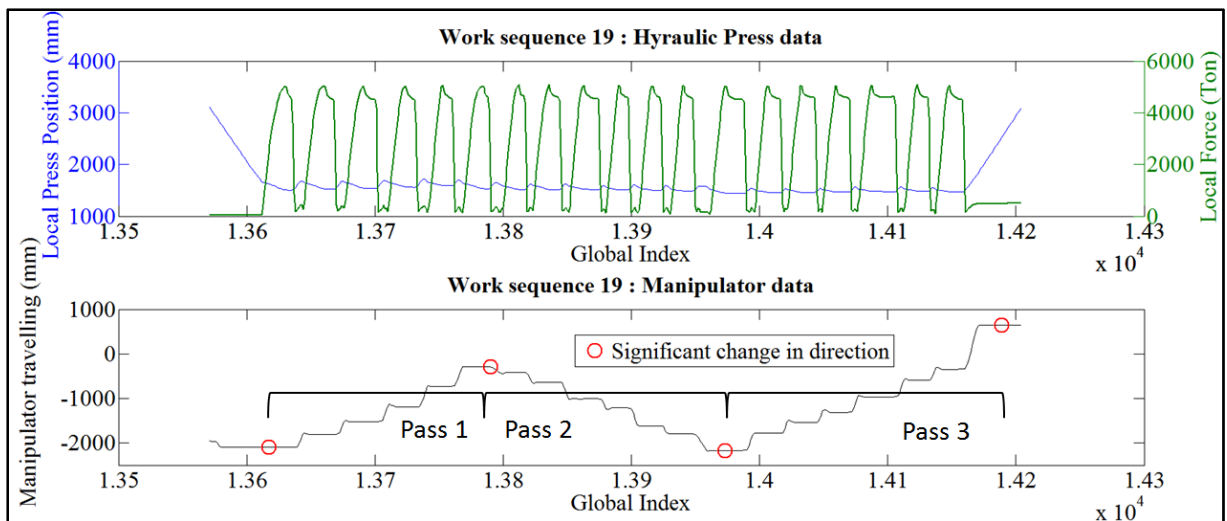
Figure 69 : Cogging - Work sequence 19 - Travel analysis
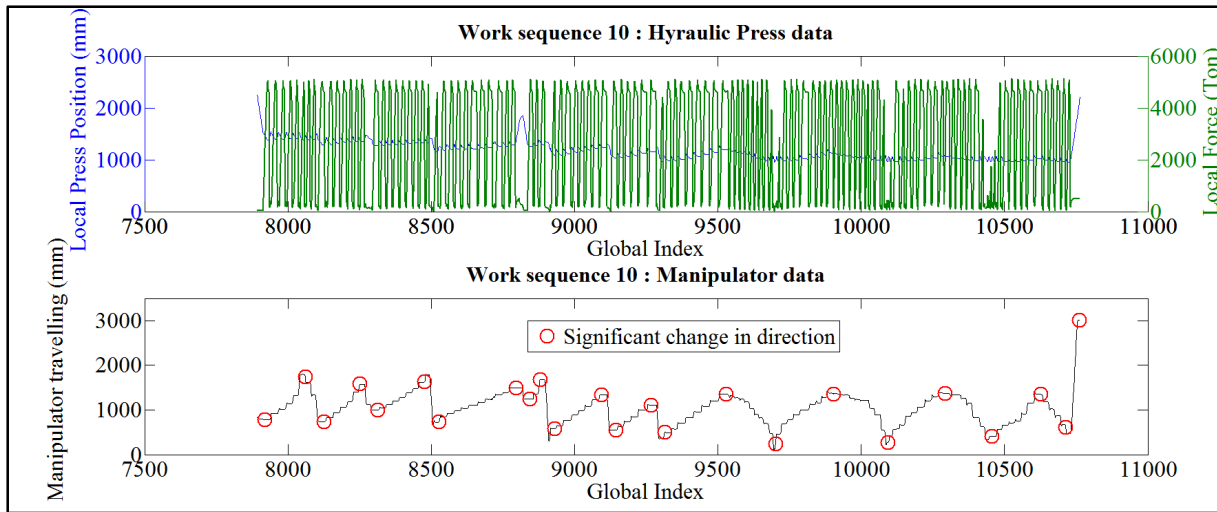
Figure 70 : Finishing - Work sequence 10 - Travel analysis

On top of back and forward movement, rotation around the parts principal axis and working on part height and width, the part undergoes one 180 degree rotation around a vertical axis with the help of the bridge crane. This rotation is equivalent to a half forging completion and marks the start of forging on the second half of the ingot. Figure 71 shows half forging completion detection for Cogging. The data point is also a point of theoretical symmetry which is particularly visible in the press position curve, see Figure 67 , with the same global index position. The symmetry is present in the numerical values of several calculated indicators.
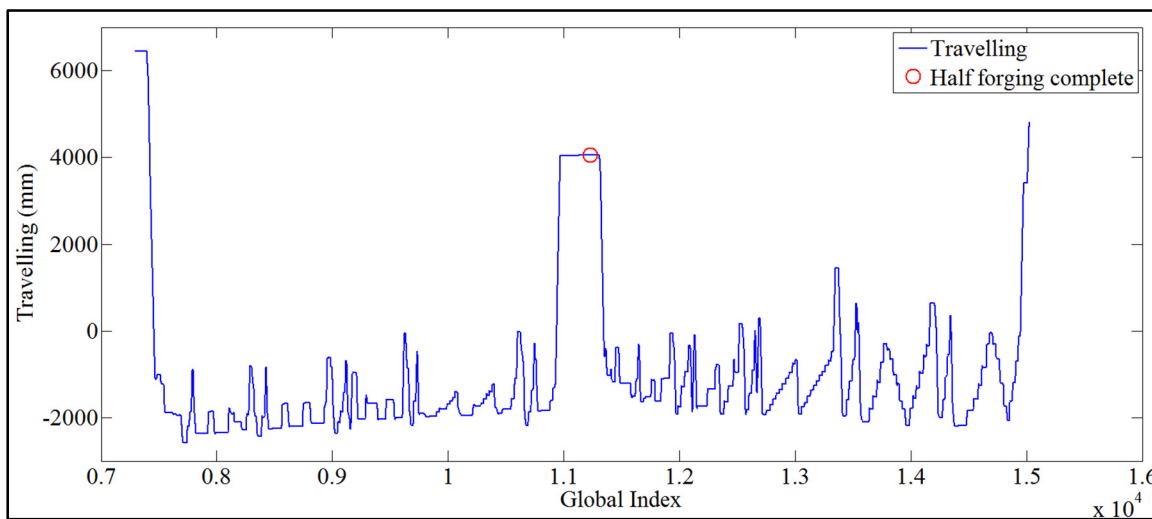
Figure 71 : Cogging - Half forging completion

After analysing travelling data, the force peaks for each work sequence are identified identically to the method used during Upsetting and the FM sequence. The position filter is also used to calculate all relative sequence indicators as proposed in 5.1.1.1. Figure 72 shows part reduction calculation for Finishing, work sequence 10. Staircase forging, as explained in 2.4.2, is observed. In this example, 6 one way passes are performed before completing a series of two way passes, starting in the zoom of Figure 72. The movement of the manipulator for the one way passes is a withdrawal from the press or backward. This means that the flow of material during deformation is from the end held by the manipulator towards the ingots free end. The part is essentially being stretched out, with material feeding the free end. This material flow pattern is characteristic of a successful forging technique. The deformation and deformation rate is shown to be greater for one way passes. The second pass of the two way passes, forward, is therefore a lot less significant for successful forging and is used just for part geometry homogeneity.
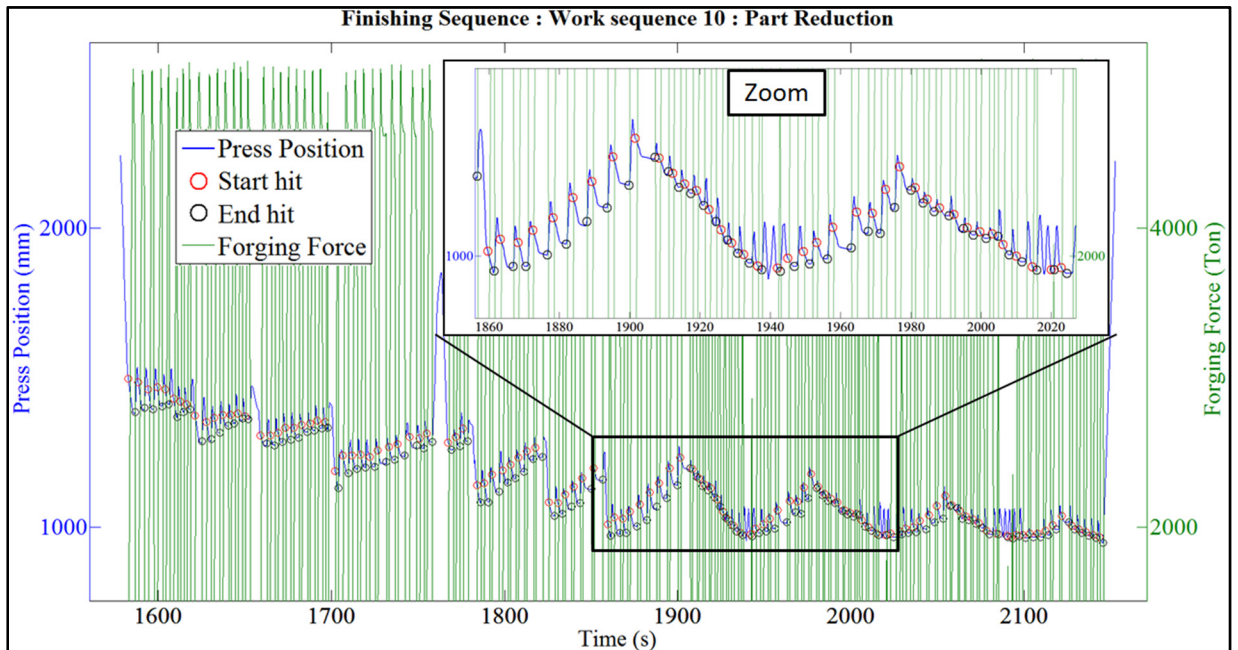
Figure 72 : Finishing - Work sequence 10 - Part reduction with zoom

Average results

The results from Table 20 show that the ingot is worked to a higher standard during Finishing in comparison to Cogging for a quasi-identical process time. The number of hits is greatly superior during Finishing for a similar amount of passes. The number of hits per pass is around 4 times that of Cogging. Approximately half the total forging time was spent on forging the first half of the ingot, which shows consistence and not over working one side to another. Table 21 proves the observation from Figure 72, significant forging occurs when material flows towards the ingots free end.

Table 20 : Cogging and Finishing average indicators

	Process Time (mins)	Switch around ratio	Number of passes	Number of hits
Cogging	50.1	0.51	47	139
Finishing	49.9	0.47	55	539

Table 21 : Cogging and Finishing anvil blow distribution

	Total number	Forward	Backward
Cogging	139	34	105
Finishing	539	194	345

5.1.2   Individual results module

Individual results allows the user to view results for an individual forging. The user interface is shown in Figure 73. Necessary input includes part casting number, selecting a forging session, and the particular sequence to visualise (top right). One or two curves, from force, speed and position, can then be observed if required. General information (top right) is given including material name and grade along with metal density. The operator for that particular forging session is displayed as well as the forging date, stop and start times. Sequence indicators from 2.3 are visible (middle left) together with process efficiency indicators (bottom left).

Potential use for this function would be for part inspection if the part was found not to conform to client specifications. A retroactive control could then take place for fault finding, taking a closer look at each forging sequence.
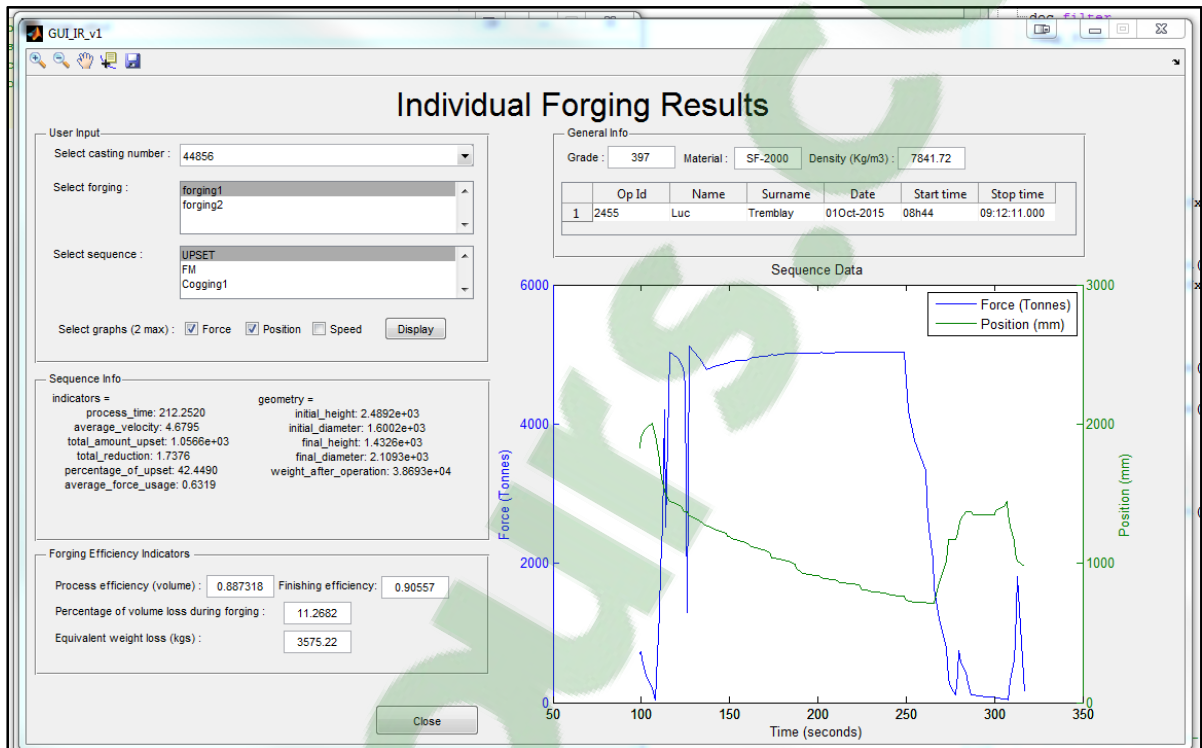

Figure 73 : Individual results user interface

5.1.3 Statistical analysis module

Global results combines information from each individual part forging and sorts the result by sequence. The user interface can be seen in Figure 74, with input being sequence and indicator selection (top left). A simplified histogram (left hand graph) and a more detailed distribution (right hand graph) of the empirical data is displayed. Probability density function matches are superimposed on the latter to show correlation. Parameters for the most suitable function are given. Sample size and standard indicator values (bottom left) are displayed to characterize the forging process. A probability calculation is available if the user wishes to calculate the occurrence of a particular event.

This function gives base line values for future forgings. The indicator standards characterize successful forgings and can therefore be useful for future successful forging predictions.
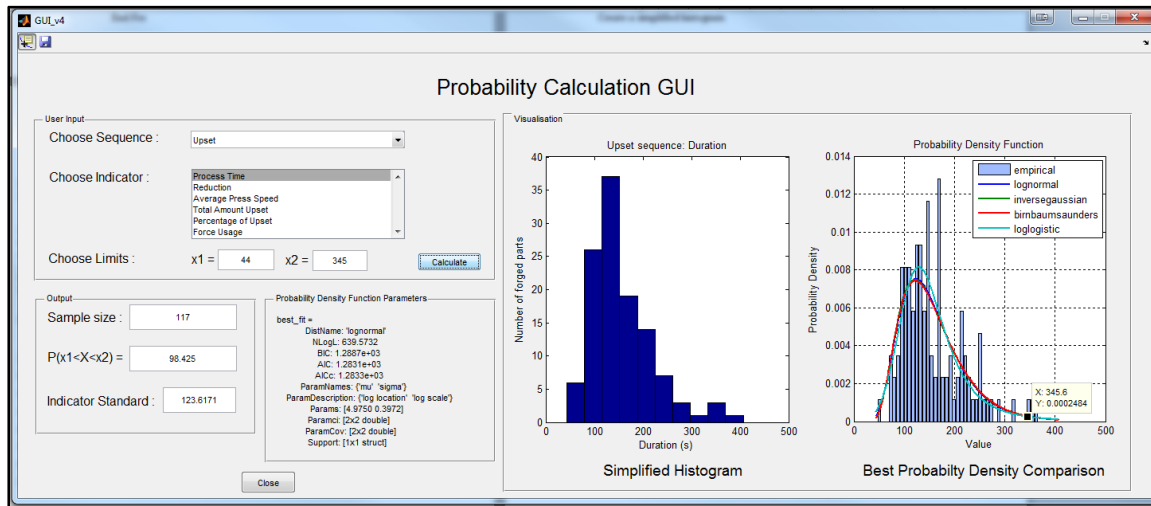
Figure 74 : Global results user interface

## 5.2	Future development

A tool able to analyse and characterize forged part sequences is only the beginning. This tool should be used as a platform for future development. A study validating the relevance of the chosen indicators and their standard values in relation to successful forgings should be completed.

A second study, looking at the interdependence between the relative sequence indicators, would then begin the development of a function capable of predicting the probability of a successful forging. Validation of this function could be simulated, emulating forgings conditions for each indicator.

The final action would be the implication of the developed prediction function into the company itself. The emulation of forging conditions would be replaced with a live data feed directly from the sensors in the forge. The information would be treated live and the probability function would show the operator if he was statistically following the guidelines set by a database of successful forgings.

CONCLUSIONS

A fast converging material specific void closure model was developed in order to assess void closure for explicit high strength steels from the industrial partner. The coupled effect of increased triaxiality states and Norton exponents was shown to have a positive effect on void closure potential. The model was then used in a full field FEM simulation, Forge Nxt 1.0 ®, for an open die forging sequence of a 40T ingot. The upsetting sequence was selected because it represents the first significant sequence of hot deformation and therefore greatly impacts upon void closure. Core areas in the ingot displayed the highest void closure potential followed by the outer core and a central zone close to the upper die. Peripheral regions showed the least potential, proving the necessity and effectiveness of the FM process.

Large amounts of experimental data from the industrial partner regarding slab forging were generated and analysed with an in-house code using Matlab 2012. The forging of over 70 parts was characterised individually and then globally using a statistical analysis. The results include standardised indicators for successful forgings and a possible future quality control.

Forge Calculus, new software for predicting successful open die high strength steel slab forgings from large ingots was developed in order to optimise forging conditions for void elimination.

The framework was defined according to an in depth study of industrial steel grades, forging processes and existing void closure models. Application of the latter to industrial case forgings was found to be missing in current literature. The open die forging process was found to incorporate five forging sequences including initial forming of a square base, upsetting, FM process, cogging and finishing. Initial forming was proven to be insignificant in terms of applied deformation and residual stress in ingot. Similarity in deformation effects on workpiece topology was observed for both the upsetting and FM respectively cogging and finishing sequences. The similarities detected are also noticeable in Forge Calculus data analysis code.

An intuitive user interface was designed in order to facilitate the visualisation and accelerate certain calculations. Real time forging quality predictions are discussed as an interesting future development for Forge Calculus.
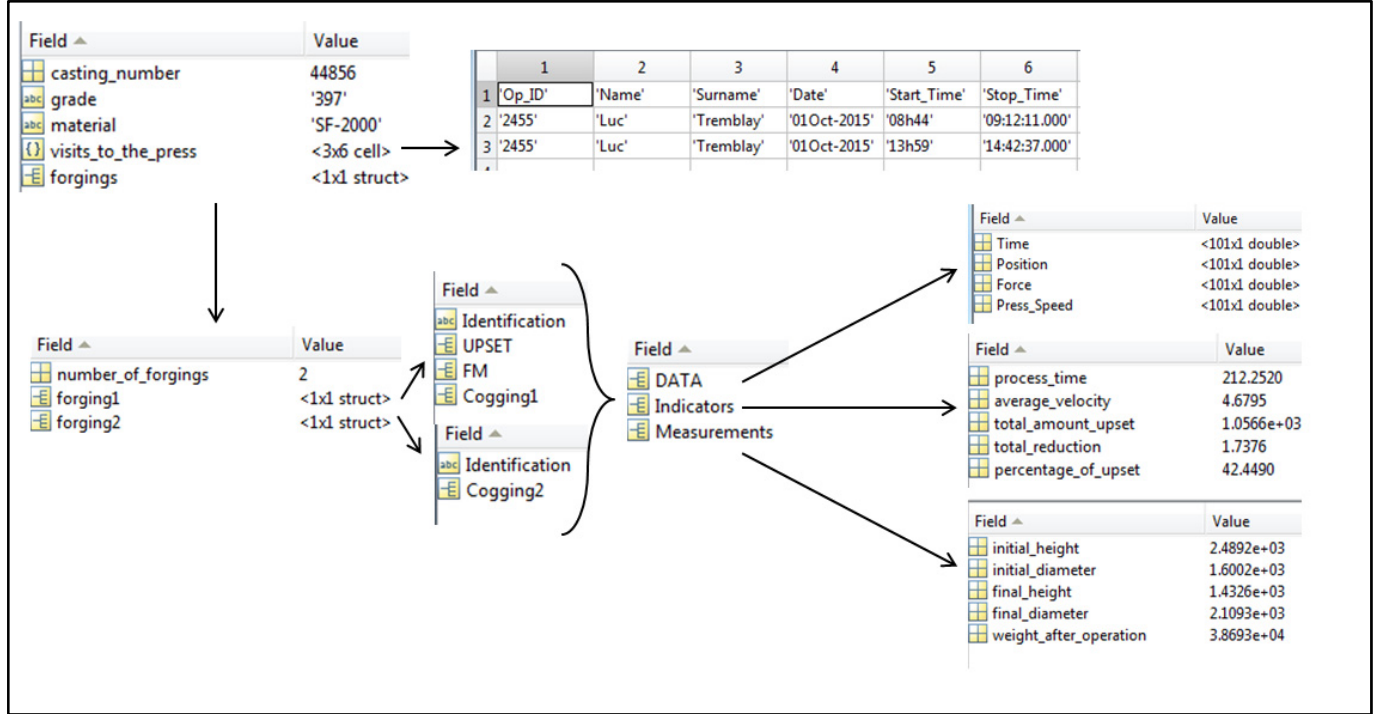
Forging plan example

Main Database Structure

Field ▲	Value
casting_number	44856
grade	'397'
material	'SF-2000'
visits_to_the_press	<3x6 cell>
forgings	<1x1 struct>

	1	2	3	4	5	6
1	'Op_ID'	'Name'	'Surname'	'Date'	'Start_Time'	'Stop_Time'
2	'2455'	'Luc'	'Tremblay'	'01Oct-2015'	'08h44'	'09:12:11.000'
3	'2455'	'Luc'	'Tremblay'	'01Oct-2015'	'13h59'	'14:42:37.000'

Field ▲	Value
number_of_forgings	2
forging1	<1x1 struct>
forging2	<1x1 struct>

Field ▲
Identification
UPSET
FM
Cogging1

Field ▲
Identification
Cogging2

Field ▲
DATA
Indicators
Measurements

Field ▲	Value
Time	<101x1 double>
Position	<101x1 double>
Force	<101x1 double>
Press_Speed	<101x1 double>

Field ▲	Value
process_time	212.2520
average_velocity	4.6795
total_amount_upset	1.0566e+03
total_reduction	1.7376
percentage_of_upset	42.4490

Field ▲	Value
initial_height	2.4892e+03
initial_diameter	1.6002e+03
final_height	1.4326e+03
final_diameter	2.1093e+03
weight_after_operation	3.8693e+04

Probability function list

Distribution Type	Formula : y= Probability density function	Information
Beta	$y = f(x \mid a,b) = \dfrac{1}{B(a,b)} x^{a-1}(1-x)^{b-1} I_{(0,1)}(x)$	$B(\cdot)$ is the Beta function
Binomial	$y = f(k \mid n,p) = \dbinom{n}{k} p^{k}(1-p)^{n-k}$	
Birnbaum-Saunders	$y = \dfrac{1}{\sqrt{2\pi}} \exp\left\{ -\dfrac{\left(\sqrt{\dfrac{x}{\beta}} - \sqrt{\dfrac{\beta}{x}}\right)^{2}}{2\gamma^{2}} \right\} \left(\dfrac{\left(\sqrt{\dfrac{x}{\beta}} + \sqrt{\dfrac{\beta}{x}}\right)}{2\gamma x} \right)$	$\beta > 0$, $\gamma > 0$, $x > 0$
Burr Type XII	$y = F(x \mid \alpha,c,k) = 1 - \dfrac{1}{\left(1 + \left(\dfrac{x}{\alpha}\right)^{c}\right)^{k}}$	$x > 0, \alpha > 0, c > 0, k >$
Exponential	$y = f(x \mid \mu) = \dfrac{1}{\mu} e^{\frac{-x}{\mu}}$	
Extreme value	$y = f(x \mid \mu,\sigma) = \dfrac{1}{\sigma} \exp\left(\dfrac{x-\mu}{\sigma}\right) \exp\left(-\exp\left(\dfrac{x-\mu}{\sigma}\right)\right)$	
Gamma	$y = f(x \mid a,b) = \dfrac{1}{b^{a}\Gamma(a)} x^{a-1} e^{\frac{-x}{b}}$	$\Gamma(\cdot)$ is the Gamma function
Generalised extreme value	$y = f(x \mid k,\mu,\sigma) = \dfrac{1}{\sigma} \exp\left(-\left(1 + k\dfrac{x-\mu}{\sigma}\right)^{-\frac{1}{k}}\right)\left(1 + k\dfrac{x-\mu}{\sigma}\right)^{-(1+\frac{1}{k})}$	
Generalised Pareto	$y = f(x \mid k,\sigma,\theta) = \dfrac{1}{\sigma}\left(1 + k\dfrac{x-\theta}{\sigma}\right)^{-(1+\frac{1}{k})}$	$\vartheta < x,\ k > 0$, or $\vartheta < x$ $< -\sigma/k$ for $k < 0$

Inverse Gaussian	$y = \sqrt{\dfrac{\lambda}{2\pi x^3}} \exp\left\{-\dfrac{\lambda}{2\mu^2 x}(x-\mu)^2\right\}$	
Logistic	$y = \dfrac{e^{\frac{x-\mu}{\sigma}}}{\sigma\left(1+e^{\frac{x-\mu}{\sigma}}\right)^2}$	
Log-logistic	$y = \dfrac{e^{\frac{\ln(x)-\mu}{\sigma}}}{\sigma\left(1+e^{\frac{\ln(x)-\mu}{\sigma}}\right)^2}$	
Lognormal	$y = f(x\,|\,\mu,\sigma) = \dfrac{1}{x\sigma\sqrt{2\pi}} e^{\frac{-(\ln x-\mu)^2}{2\sigma^2}}$	
Nakagami	$y = 2\left(\dfrac{\mu}{\omega}\right)^{\mu}\dfrac{1}{\Gamma(\mu)}x^{(2\mu-1)}e^{\frac{-\mu}{\omega}x^2}$	$\omega > 0$ for $x > 0$
Normal	$y = f(x\,|\,\mu,\sigma) = \dfrac{1}{\sigma\sqrt{2\pi}} e^{\frac{-(x-\mu)^2}{2\sigma^2}}$	
Poisson	$y = f(x\,|\,\lambda) = \dfrac{\lambda^x}{x!}e^{-\lambda}I_{(0,1,..)}(x)$	
Rayleigh	$y = f(x\,|\,b) = \dfrac{x}{b^2}e^{\frac{-x^2}{2b^2}}$	
Rician	$y = I_0\left(\dfrac{xs}{\sigma^2}\right)\dfrac{x}{\sigma^2}e^{-\left(\frac{x^2+s^2}{2\sigma^2}\right)}$	$s \geq 0$, $\sigma > 0$, for $x > 0$. I_0 is the zero order Bessel function.
t Location - Scale	$y = \dfrac{\Gamma\left(\dfrac{\upsilon+1}{2}\right)}{\sigma\sqrt{\upsilon\pi}\Gamma\left(\dfrac{\upsilon}{2}\right)}\left[\dfrac{\upsilon+\left(\dfrac{x-\mu}{\sigma}\right)^2}{\upsilon}\right]^{-\left(\frac{\upsilon+1}{2}\right)}$	$\sigma > 0$, $\nu > 0$
Weibull	$y = f(x\,|\,a,b) = \dfrac{b}{a}\left(\dfrac{x}{a}\right)^{b-1}e^{-\left(\frac{x}{a}\right)^b}$	$x>0$, $a>0$, $b>0$,

BIBLIOGRAPHY

(FORGE NxT 1.0 ®). 694 av. Donat, 06255 Mougins Cedex, France, Transvalor S.A. .

Azushima, A., et al. (2012). "Coefficient of friction at interface of lubricated upsetting process." Wear **286–287**(0): 3-7.

Banaszek, G. and A. Stefanik (2006). "Theoretical and laboratory modelling of the closure of metallurgical defects during forming of a forging." Journal of Materials Processing Technology **177**(1–3): 238-242.

Budiansky, B., et al. (1982). "Void growth and collapse in viscous solids." Pergamon Press, Oxford: 32.

Carroll, J. D., et al. (2012). "The effect of grain size on local deformation near a void-like stress concentration." International Journal of Plasticity **39**(0): 46-60.

Chen, D.-C. (2006). "Rigid-plastic finite element analysis of plastic deformation of porous metal sheets containing internal void defects." Journal of Materials Processing Technology **180**(1–3): 193-200.

Chen, K., et al. (2012). "Strain function analysis method for void closure in the forging process of the large-sized steel ingot." Computational Materials Science **51**(1): 72-77.

Chen, M.-S. and Y. C. Lin (2013). "Numerical simulation and experimental verification of void evolution inside large forgings during hot working." International Journal of Plasticity **49**(0): 53-70.

Chen, M.-S., et al. (2014). "Evolution of elliptic-cylindrical and circular-cylindrical voids inside power-law viscous solids." International Journal of Plasticity **53**(0): 206-227.

Cho, J. R., et al. (1998). "Analysis of the cogging process for heavy ingots by finite element method and physical modelling method." Journal of Materials Processing Technology **80–81**(0): 161-165.

Dudra, S. P. and Y.-T. Im (1990). "Analysis of void closure in open-die forging." International Journal of Machine Tools and Manufacture **30**(1): 65-75.

Duva, J. M. and J. W. Hutchinson (1984). "Constitutive potentials for dilutely voided nonlinear materials." Mechanics of Materials **3**(1): 41-54.

Everett, R. K., et al. (2001). "Spatial distribution of voids in HY-100 steel by X-ray tomography." Scripta Materialia **44**(1): 165-169.

138

Fleck, N. A. and J. W. Hutchinson (2001). "A reformulation of strain gradient plasticity." Journal of the Mechanics and Physics of Solids **49**(10): 2245-2271.

Gurson, A. L. (1977). "Continuum Theory of Ductile Rupture by Void Nucleation and Growth: Part I—Yield Criteria and Flow Rules for Porous Ductile Media." Journal of Engineering Materials and Technology **99**(1): 2-15.

He, M. Y. and J. W. Hutchinson (1981). "The Penny-Shaped Crack and the Plane Strain Crack in an Infinite Body of Power-Law Material." Journal of Applied Mechanics **48**(4): 830-840.

Huang., Z. P. and J. Wang. (2006). "Nonlinear Mechanics of Solids containing Isolated Voids " Applied Mechanics Review **59**: 20.

K.Chadha, et al. (2015). "An Approach to Develop Hansel-Spittel Constitutive Equation during Ingot Breakdown Operation of Low Alloy Steels." FiMPART: 6.

Kakimoto, H., et al. (2010). "Development of forging process design to close internal voids." Journal of Materials Processing Technology **210**(3): 415-422.

Keife, H. and U. Ståhlberg (1980). "Influence of pressure on the closure of voids during plastic deformation." Journal of Mechanical Working Technology **4**(2): 133-143.

Kim, Y., et al. (2011). "Efficient forging process to improve the closing effect of the inner void on an ultra-large ingot." Journal of Materials Processing Technology **211**(6): 1005-1013.

Kut, S. (2009). "State of Stress Identification in numerical modeling of 3D issues." Archives of Metallurgy and Materials **54**(3).

Lecarme, L., et al. (2014). "Heterogenous void growth revealed by in situ 3-D X-ray microtomography using automatic cavity tracking." Acta Materialia **63**: 130-139.

Lee, B. J. and M. E. Mear (1994). "Studies of the Growth and Collapse of Voids in Viscous Solids." Journal of Engineering Materials and Technology **116**(3): 348-358.

Lee, B. J. and M. E. Mear (1999). "Evolution of elliptical voids in power-law viscous solids." Mechanics of Materials **31**(1): 9-28.

Lee, Y. S., et al. (2011). "Internal void closure during the forging of large cast ingots using a simulation approach." Journal of Materials Processing Technology **211**(6): 1136-1145.

Li, J., et al. (2014). "Simulation of macrosegregation in a 2.45-ton steel ingot using a three-phase mixed columnar-equiaxed model." International Journal of Heat and Mass Transfer **72**: 668-679.

Lin, Y. C., et al. (2008). "Numerical simulation for stress/strain distribution and microstructural evolution in 42CrMo steel during hot upsetting process." Computational Materials Science **43**(4): 1117-1122.

Maire, E., et al. (2001). "On the Application of X-ray Microtomography in the Field of Materials Science." Advanced Engineering Materials **3**(8): 539-546.

Montheillet, F. and J. J. Jonas (1996). "Temperature dependence of the rate sensitivity and its effect on the activation energy." Metallurgical and Materials Transactions **27**(10): 3.

Niordson, C. F. (2008). "Void growth to coalescence in a non-local material." European Journal of Mechanics - A/Solids **27**(2): 222-233.

P. M.Dixit, U. S. D. (2008). Modelling of Metal Forming and Machining Processes: by Finite Element and Soft Computing Methods, Engineering Materials and Processes.

Park, C. Y. and D. Y. Yang (1996). "A study of void crushing in large forgings I: Bonding mechanism and estimation model for bonding efficiency." Journal of Materials Processing Technology **57**(1–2): 129-140.

Ragab, A. R. (2004). "Application of an extended void growth model with strain hardening and void shape evolution to ductile fracture under axisymmetric tension." Engineering Fracture Mechanics **71**(11): 1515-1534.

Rice, J. R. and D. M. Tracey (1969). "On the ductile enlargement of voids in triaxial stress fields∗." Journal of the Mechanics and Physics of Solids **17**(3): 201-217.

Roux, E., et al. (2013). "A level-set and anisotropic adaptive remeshing strategy for the modeling of void growth under large plastic strain." Computational Materials Science **68**(0): 32-46.

Saby, M. (2013). "Compréhension et modélisation des mécanismes de refermeture de porosité dans les procédés de mise en forme des métaux à chaud." 234.

Saby, M., et al. (2014). "Understanding and Modeling of Void Closure Mechanisms in Hot Metal Forming Processes: A Multiscale Approach." Procedia Engineering **81**(0): 137-142.

Saby, M., et al. (2013). "Analyse multi-échelle de la refermeture de porosités, appliquée à la mise en forme des métaux à chaud." 11e Colloque National en Calcul des Structures.

Saby, M., et al. (2013). "Three-dimensional analysis of real void closure at the meso-scale during hot metal forming processes." Computational Materials Science **77**(0): 194-201.

Saby, M., et al. (2015). "Void closure criteria for hot metal forming: A review." Journal of Manufacturing Processes **19**(0): 239-250.

Samei, J., et al. (2016). "Influence of strain path on nucleation and growth of voids in dual phase steel sheets." Materials & Design **92**: 1028-1037.

Song, M., et al. (2014). "In situ electron microscopy investigation of void healing in an Al–Mg–Er alloy at a low temperature." Acta Materialia **69**(0): 236-245.

Sternberg, S. R. (1983). "Biomedical Image Processing." Computer **16**(1): 22-34.

Szelążek, J., et al. (2009). "New samples with artificial voids for ultrasonic investigation of material damage due to creep." NDT & E International **42**(2): 150-156.

Tkadlečková, M., et al. (2013). "The effect of boundary conditions of casting on the size of porosity of heavy steel ingot." Journal of Achievements in Materials and Manufacturing Engineering **56**(1): 9.

Toda, H., et al. (2009). "Healing behavior of preexisting hydrogen micropores in aluminum alloys during plastic deformation." Acta Materialia **57**(15): 4391-4403.

Tvergaard, V. (1982). "On localization in ductile materials containing spherical voids." International Journal of Fracture **18**(4): 237-252.

Tvergaard, V. (1984). "On the creep constrained diffusive cavitation of grain boundary facets." Journal of the Mechanics and Physics of Solids **32**(5): 373-393.

Xu, B., et al. "Modeling of The Void Close Behavior in a 100t Ingot during Hot Forging." Metal Forming: 4.

Zhang, J. (2016). 11 - Defect detection, classification, and characterization using ultrasound A2 - Yuan, Fuh-Gwo. Structural Health Monitoring (SHM) in Aerospace Structures, Woodhead Publishing**:** 307-323.

Zhang, X.-X. and Z.-S. Cui (2009). "Theoretical study of void closure in nonlinear plastic materials." Applied Mathematics and Mechanics **30**(5): 631-642.

Zhang, X.-X., et al. (2009). "A criterion for void closure in large ingots during hot forging." Journal of Materials Processing Technology **209**(4): 1950-1959.

Zhang, X., et al. (2012). "Multi-scale Analysis of Void Closure for Heavy Ingot Hot Forging." <u>Modern Applied Science</u> **6**(10): 11.

Zhongxiao, J. and G. W. Stewart. (2000). "An analysis of the rayleigh-ritz method for approximating eigenspaces." <u>Mathematics of computation</u> **70**(234): 10.